SIEMENS

MAGNETOM Flash

The Magazine of MRI

Issue Number 3/2014 | ISMRM Edition

Not for distribution in the US

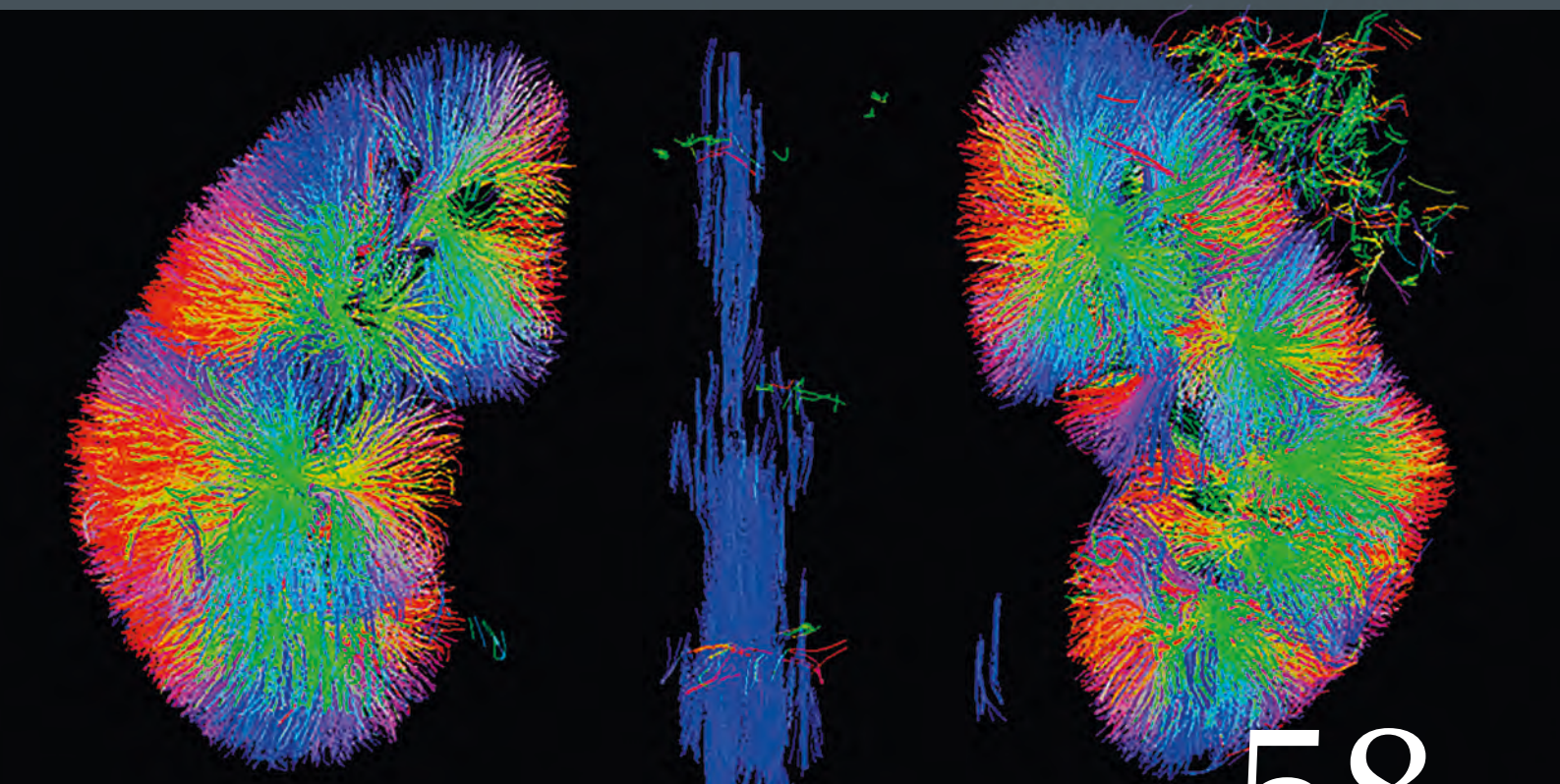

58

Assessment of Renal Allograft Function with DTI and Tractography, Page 28

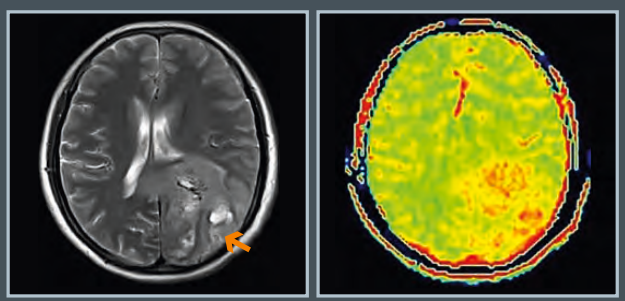

Amide Proton Transfer MRI in Patients with High- and Low-Grade Gliomas, Page 39

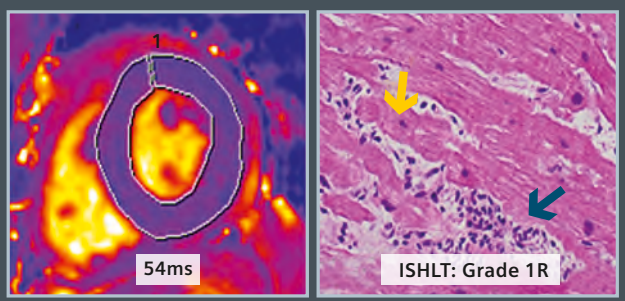

CMR Elastography to Estimate Myocardial Stiffness, Page 76

Professor Elmar Merkle, M.D., is a Senior Vice President of the Cross-Functional Medical Services Unit at University Hospital Basel (USB) in Switzerland. He joined the Faculty at USB in 2012, where he also serves as the Chairman of the Department of Radiology.

His current research interests include Abdominopelvic MRI and MR Angiography. Professor Merkle has dedicated his career to efficient workflows in imaging and reporting, and he is widely recognized for his contributions in this field.

Dear MAGNETOM Flash reader,

When I was searching the World Wide Web to prepare for this editorial I included the term "efficiency" in my search. Why? Because this is a word frequently mentioned as a reason why Computed Tomography or Ultrasound is often preferred to MR in daily clinical practice – especially in abdominal imaging. Two dictionary definitions of the word caught my attention and helped me relate it to our profession:
"competence: the ability to do something well or achieve a desired result without wasted energy or effort"
and
"competency in performance".
Whilst efficiency is often associated with time and cost issues, for us radiologists the goals to do something well and to achieve the desired result are of equal importance. This is especially true in some of the more challenging applications, such as liver imaging: The detailed assessment of the various vascular hepatic systems, the biliary anatomy and its variations, and the hepatic volume for surgical planning; the selection of the most promising hepatic area during liver biopsies in cirrhotic patients; or the detection of even the smallest metastases for planning of advanced liver resection. In such situations we are met not only by the technical challenges required to be able to provide this information, but also by our responsibilities for the well-being of our patients. These challenges demand "competency in performance".

MRI has been proven to give much added value compared to CT and US in many clinical scenarios, especially in the context of appropriate treatment selection and outcome monitoring. It can evaluate the biliary system non-invasively by MRCP; detect the smallest lesions by diffusion weighted imaging; and quantify and monitor fatty liver diseases by imaging or spectroscopy. But how do all these techniques help when our patients are simply too short of breath to go through a simple post-contrast dynamic scan? What happens if our dynamic Gadolinium enhanced scans simply take too much time or the timing is insufficient for achieving the perfect dynamic phase?

Clinical competency is another ingredient for an efficient use of imaging techniques. Imaging efficiency can be improved only by understanding the clinical question, the underlying pathophysiology, and by complementing this with the radiologic expertise of what is technically feasible. Let me illustrate this by using the following example: Young female patients oftentimes present clinically with 'pelvic fullness'. Usually, percutaneous ultrasound is being performed as a first imaging step, and sometimes uterine leiomyomata are detected. As minimally invasive treatment options such as thermal ablation or transarterial fibroid embolization have matured over the past decade, oftentimes a contrast enhanced MRI is being ordered for subsequent treatment planning. By simply adding a Gadolinium enhanced time-resolved MR angiography, flow dynamics and direction in the ovarian veins can be evaluated with reversed flow supporting an alternative diagnosis of pelvic fullness such as pelvic congestion syndrome. The amount of time this will add to the total exam time is negligible. And why choose MRI overall? Because gentle imaging is advised for all patients, not only for children and adolescents; because we want to avoid any potential risk of radiation.

"MRI has been proven to give much added value compared to CT and US in many clinical scenarios, especially in the context of appropriate treatment selection and outcome monitoring."

Professor Elmar Merkle, M.D.

In this issue of the MAGNETOM Flash you will read about many other developments in the field of abdominal imaging which will resonate with us radiologists. I think these articles will encourage you to consider how this changes the competency of MRI. But aside from your own opinion about the efficiency of MR in the clinical scenarios presented in the following pages, I hope you enjoy reading them for the added clinical value they may provide to your daily work.

Editorial Board

We appreciate your comments.
Please contact us at magnetomworld.med@siemens.com

Antje Hellwich
Editor-in-chief

Wellesley Were
MR Business Development Manager Australia and New Zealand

Ralph Strecker
MR Collaborations Manager, São Paulo, Brazil

Sven Zühlsdorff, Ph.D.
Clinical Collaboration Manager, Chicago, IL, USA

Gary R. McNeal, MS (BME)
Advanced Application Specialist, Cardiovascular MR Imaging Hoffman Estates, IL, USA

Peter Kreisler, Ph.D.
Collaborations & Applications, Erlangen, Germany

Review Board

Lisa **Chuah**, Ph.D.
Global Segment Manager Neurology
Lars **Drüppel**, Ph.D.
Global Segment Manager Cardiovascular MR
Wilhelm **Horger**
Application Development Oncology
Michelle **Kessler**
US Installed Base Manager
Berthold **Kiefer**, Ph.D.
Head of Oncological and Interventional Applications
Sunil **Kumar** S.L., Ph.D.
Senior Manager Applications
Reto **Merges**
Head of Outbound Marketing MR Applications
Edgar **Müller**
Head of Cardiovascular Applications
Heiko **Meyer**, Ph.D.
Head of Neuro Applications
Heike **Weh**
Clinical Data Manager

Content

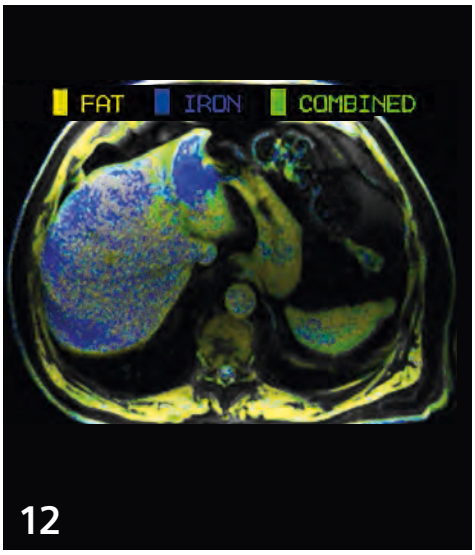

Learn from the experience of other MAGNETOM users

The MAGNETOM World is the community of Siemens MR users worldwide, providing you with relevant clinical information. Here you will find application tips and protocols to optimize your daily work. Lectures and presentations from experts in the field will allow you to be exposed to new ideas and alternative clinical approaches.

Put the advantages of the MAGNETOM World to work for you!

www.siemens.com/magnetom-world

Abdominal Imaging

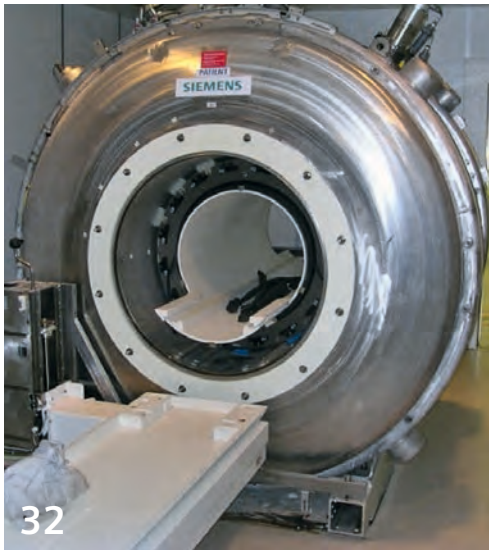

MAGNETOM Trio Upgrade to Prisma^{fit}

Highest Quality Spine Imaging in an Optimized Clinical Workflow

Kawasaki Disease on CMR

Business

Neurology

Orthopedic Imaging

Pediatric Imaging

Cardiovascular Imaging

MAGNETOM Prisma – Abdominal Applications

Caroline Zähringer, M.D.; Tobias Heye M.D.; Gregor Sommer, M.D.; Georg Bongartz; M.D.

Department of Radiology and Nuclear Medicine, University Hospital Basel, Basel, Switzerland

Introduction

In 2002, the first 3 Tesla (T) magnetic resonance imaging (MRI) scanner was approved for clinical use by the Food and Drug Administration. The increase in magnetic field strength technology promised new opportunities in MRI diagnosis and improvement of already established MRI procedures [1–3]. 3T MRI offers a higher signal-to-noise ratio (SNR) compared with lower field strength MRI, which leads to a higher spatial resolution or improved signal exploitation allowing for shorter acquisition times while keeping spatial resolution constant [4, 5]. With the implementation of parallel imaging techniques, imaging acceleration can be performed with a higher acceleration factor compared to lower field strength MRI [6]. Due to slight differences in magnetization characteristics at 3T compared to 1.5T, contrast-to-noise ratio (CNR) is also increased, resulting in improved lesion conspicuity in contrast-enhanced imaging, more sufficient background signal suppression and better fat/water separation [7, 8].

The experience from the clinical routine shows that imaging of the brain and the musculoskeletal system achieved better results with 3T MRI compared with lower field strength. In brain imaging for example, 3T MRI scanners were sufficiently able to detect very small contrast enhancing lesions in the diagnosis of multiple sclerosis [1]. In musculoskeletal imaging the advantages can either lead to depicting fine details of small joints or to a significant reduction in scan time. Theoretically, these advantages could also be used for abdominal imaging, but particular challenges of this body region may increase the risk for artifacts.

In abdominal imaging, especially, increasing the field strength not only provides opportunities for improving image quality and acquisition speed, but also results in more demanding technical challenges. Higher field strength causes an increase in main magnetic field (B_0) inhomogeneity, radiofrequency field (B_1) inhomogeneity, increase the amount of radiofrequency (RF) energy deposition in tissue, and cause an increase in chemical shift and susceptibility artifacts [7, 8]. Suboptimal fat suppression may pose an additional diagnostic issue. The use of parallel imaging techniques can be negatively affected by noise bands through the image plane which occur more often in examinations with a large field-of-view (FOV). Therefore, a simple transfer of imaging protocols from 1.5T to 3T is not applicable.

However, the technical development in the new generation of MR scanners enables the issues in abdominal imaging listed above to be addressed. In this article we will briefly discuss the advan-

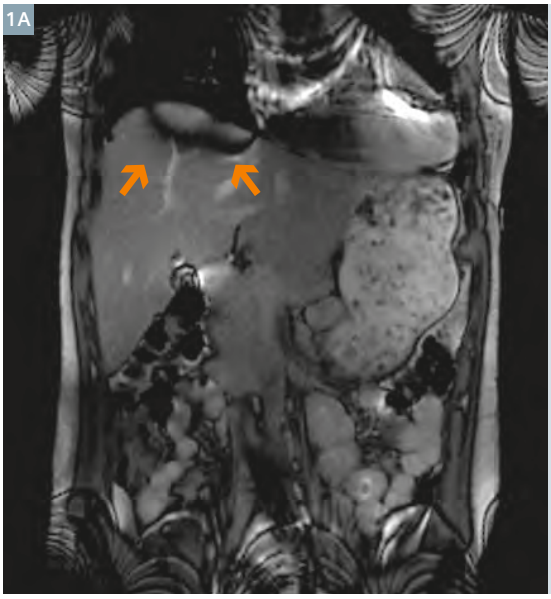

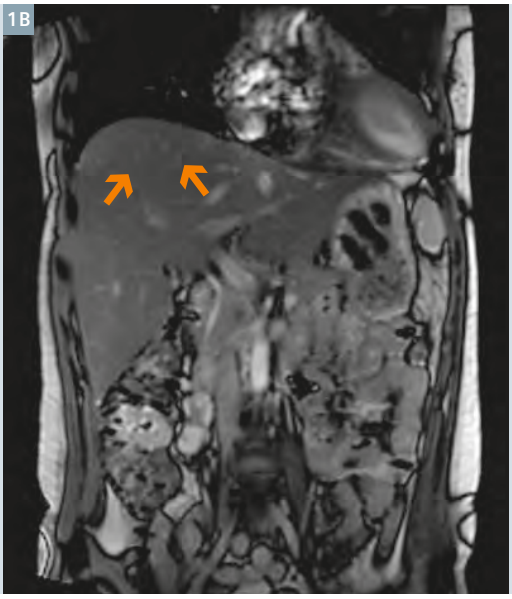

1

Comparison of TrueFISP in the same volunteer performed on a standard 3T MR scanner **(1A)** and on MAGNETOM Prisma **(1B)**. Distortion artifacts are markedly reduced. (Sequence details 1A, 1B: Slice thickness (ST) 10 mm; TR 289 s; TE 1.14 ms; Matrix 156 × 116; Field-of-view (FOV) 40 × 40 cm).

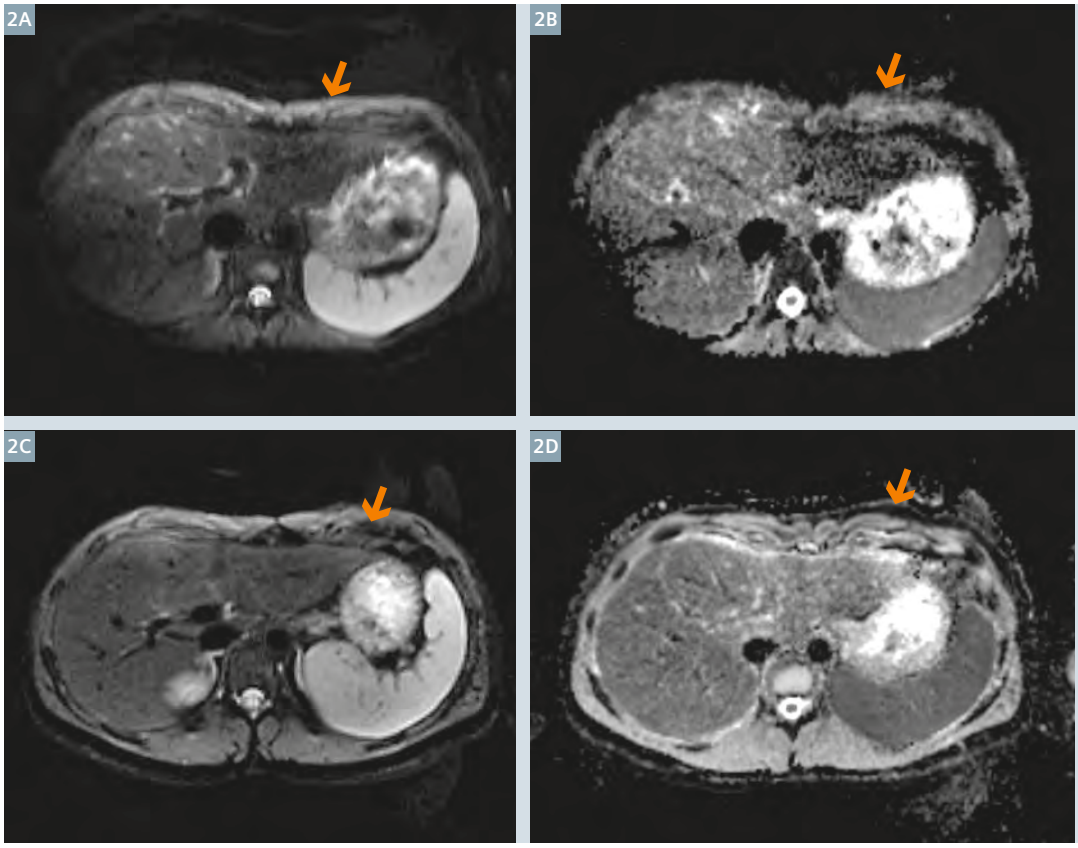

2

DWI and ADC maps of the liver in the same volunteer performed on a standard 3T MR scanner **(2A, B)** and on the MAGNETOM Prisma **(2C, D)**. The homogeneous B_0 and B_1 fields provide improved image quality at MAGNETOM Prisma, especially of the left liver lobe. (Sequence details 2A–D: ST 5 mm; TR 6.6 s; TE 63 ms; Matrix 192 × 156; FOV 41 × 33 cm; b = 800 s/mm²).

tages and challenges of 3T abdominal imaging and demonstrate how the next generation MR scanner, the MAGNETOM Prisma, performs in this context.

Advantages of 3T MRI in abdominal imaging

Many clinical studies over recent years have shown that abdominal MRI examinations can benefit from 3T MRI due to the available increase in SNR and CNR [7, 8]. With higher SNR, higher spatial resolution can be achieved, resulting in an improved image quality offering the possibility to detect smaller lesions and to delineate finer anatomic structures. Increased CNR is a consequence of longer T1 times, as well as improved background suppression and precise fat/water separation [11, 12].

The high signal in 3T MRI allows for improvement and acceleration of parallel imaging techniques, (e.g. generalized autocalibrating partially parallel acquisition, GRAPPA) [6]. The scan time is thereby significantly reduced with the help of multiple coils, subsequent reconstruction methods and by subsampling the *k*-space. With the use of GRAPPA technique, diagnostic examinations of the abdomen can be performed in patients with impaired or poor breath-holding capabilities. The CAIPIRINHA (controlled aliasing in parallel imaging results in higher acceleration) technique benefits markedly from the improved signal in 3T MRI [9]. This technique can be used in liver imaging to acquire multiarterial phase acquisitions, which are especially helpful in the diagnosis of hepatocellular carcinoma by obtaining adequately-timed arterial phase images [10].

Challenges of 3T MRI in abdominal imaging and how MAGNETOM Prisma performs in these conditions

Whilst there are clear advantages to 3T MRI, there are still some challenges that need to be met, particularly in abdominal imaging.

The recently-introduced next generation 3T MR scanner, MAGNETOM Prisma, is longer and slimmer in size compared to standard 3T MR scanners. With a combination of high gradient strength (80 m/T) and fast gradient slew rates (200 m/T/s), the homogeneity of the magnetic field is improved. The new system provides up to 204 coils elements with up to 128 integrated receive channels and uses the 4th generation coil architecture, total imaging matrix (Tim 4G).

In order to establish a correct spatial resolution for avoiding artifacts in MRI (e.g. distortion), the spatial linearity of the gradient has to be matched with the volume of consideration. The gradient coils are surrounded by conductive structures where eddy currents are generated by the time-varying magnetic field. At higher field strength these eddy currents effects are higher, resulting in the disruption of B_0 homogeneity, and are reflected by distortion artifacts. MAGNETOM Prisma counteracts this effect with a higher gradient strength coupled with advanced shimming solutions that allow for finer and more effective compensation of patient-induced disturbances. Figure 1 illustrates how the MAGNETOM Prisma performs in true fast abdominal

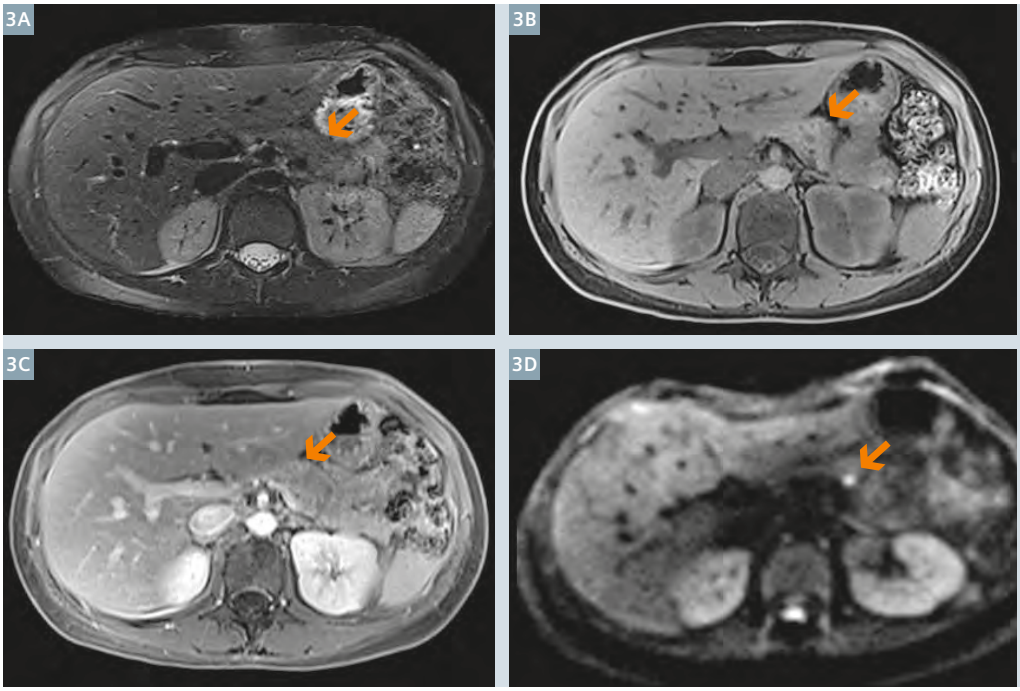

3

Insulinoma (**3A**: T2-weighted, **3B**: T1-weighted without contrast, **3C**: T1-weighted with contrast, **3D**: DWI). Excellent image quality resulting in good lesion conspicuity allows for detecting a small lesion in the pancreas tail. (Sequence details 3A: ST 4.8 mm; TR 1.6 s; TE 117 ms; Matrix 320 × 170; 3B: ST 2.5 mm; TR 3.92 s; TE 1.24 ms; Matrix 288 × 187; 3C: ST 2.5 mm; TR 4.16 s; TE 2.01 ms; Matrix 320 × 147; 3D: ST 4 mm; TR 6.6 s; TE 63 ms; Matrix 192 × 156; b = 800 s/mm²).

imaging with steady state free precession (TrueFISP) imaging compared to a standard 3T MRI scanner. Image quality is significantly improved and distortions are reduced especially in the periphery.

As mentioned above, higher field strengths result in pronounced image artifacts from B_1 inhomogeneities in comparison to lower field strengths [13]. The frequency required to excite the magnetization increases linearly with the field strength. Human body tissues have a high dielectric constant reducing the wavelength of the RF field significantly which results in standing wave artifacts. These images have regions of increased and decreased magnitudes which produce bright areas away from the receiver coils or dark areas near the receiver coils [4, 14, 15]. Thus, the result of B_1 inhomogeneities can be loss of image contrast. This problem plays an important role in abdominal imaging due to the large FOV further amplifying B_1 inhomogeneities.

Liver MRI is a well-established clinical application for the characterization of focal hepatic lesions, but it remains a complex technique requiring optimal patient compliance and technical conditions to obtain diagnostic images [16]. Due to B_0 and B_1 imperfections, a homogeneous large field-of-view image is more difficult to acquire at 3T. Diffusion-weighted imaging (DWI) of the liver can assess microstructural cell characteristics such as cellularity. In figure 2 an example of DWI of the liver is depicted as a comparison between a standard 3T MR scanner and the MAGNETOM Prisma. With improved homogeneity of the technical setup, the entire liver parenchyma is homogeneously imaged and previously problematic areas, such as the left liver lobe, have an evenly distributed signal similar to the right liver lobe.

The detection of very small lesions in abdominal organs remains challenging in MR imaging. In particular, the examination of the pancreas requires adequate diagnostic images to detect and characterize small lesions. Figure 3 shows an example of an insulinoma measuring 6 × 4 mm clearly detectable in the pancreatic tail.

Imaging at 3T has the advantage of increased signal, but has to cope with disadvantages including increased chemical shift, increased susceptibility and motion artifacts [17]. Chemical shift artifacts are caused by different resonant frequencies of water and fat resulting in a chemical shift misregistration of water/fat spins which precess at the same frequency along the frequency encoding axis. At 3T MRI the chemical shift between fat and water spins increases by a factor of two occurring for instance around the kidneys potentially mimicking a subcapsular hematoma [18]. As a result of static microscopic gradients or variations in the magnetic field, susceptibility artifacts occur near tissue interfaces with different magnetic susceptibilities [14]. In abdominal imaging a multitude of boundaries between air and soft tissue are present, (e.g. adjacent to the stomach, bowel or near the diaphragm) which may increase the risk for susceptibility artifacts. At high field strength, susceptibility artifacts are more pronounced and can obscure anatomical details or important findings [14, 15, 18, 19]. Figure 4 shows T2 and DWI of the prostate of the same healthy volunteer with a standard 3T MRI scanner and with the MAGNETOM Prisma. Artifacts are significantly reduced on images acquired with the MAGNETOM Prisma. The high gradient slew rates

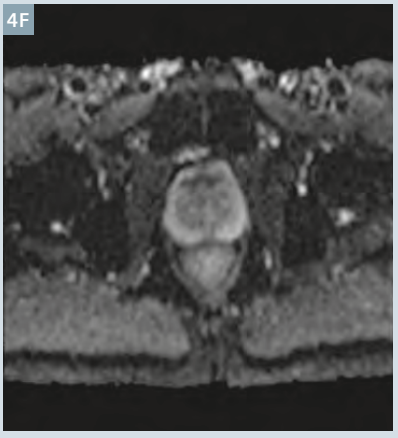

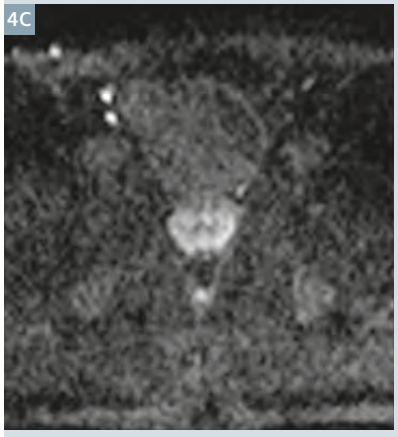

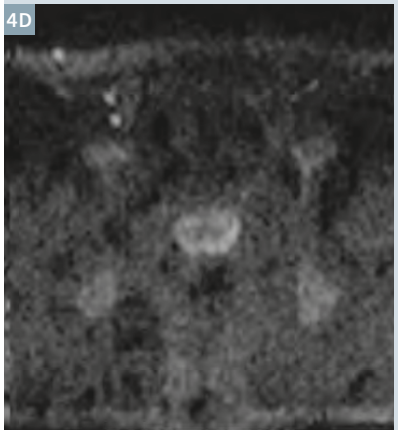

4

Comparison of prostate imaging performed with a standard 3T MRI scanner **(4A–D)** and with the MAGNETOM Prisma **(4E–F)**, T2-weighted and DWI with b-values of 0, 1000 and 2000 s/mm². In DWI acquired on the MAGNETOM Prisma platform the signal is higher and less noisy also at high b-values.
(Sequence details 4A: ST 3 mm; TR 5.15 s, TE 143 ms; Matrix 448 × 254; FOV 23 cm²; 4B–D: ST 2.5 mm, TR: 3.9 s; TE 72 ms; Matrix 100; FOV 25 cm²; 4E: ST 3.5 mm; TR 7.5 s, TE 101 ms; Matrix 320; FOV 23 cm²; 4F–H: ST 2.5 mm, TR: 3.7 s; TE 50 ms; Matrix 100 × 10; FOV; 25 cm²).

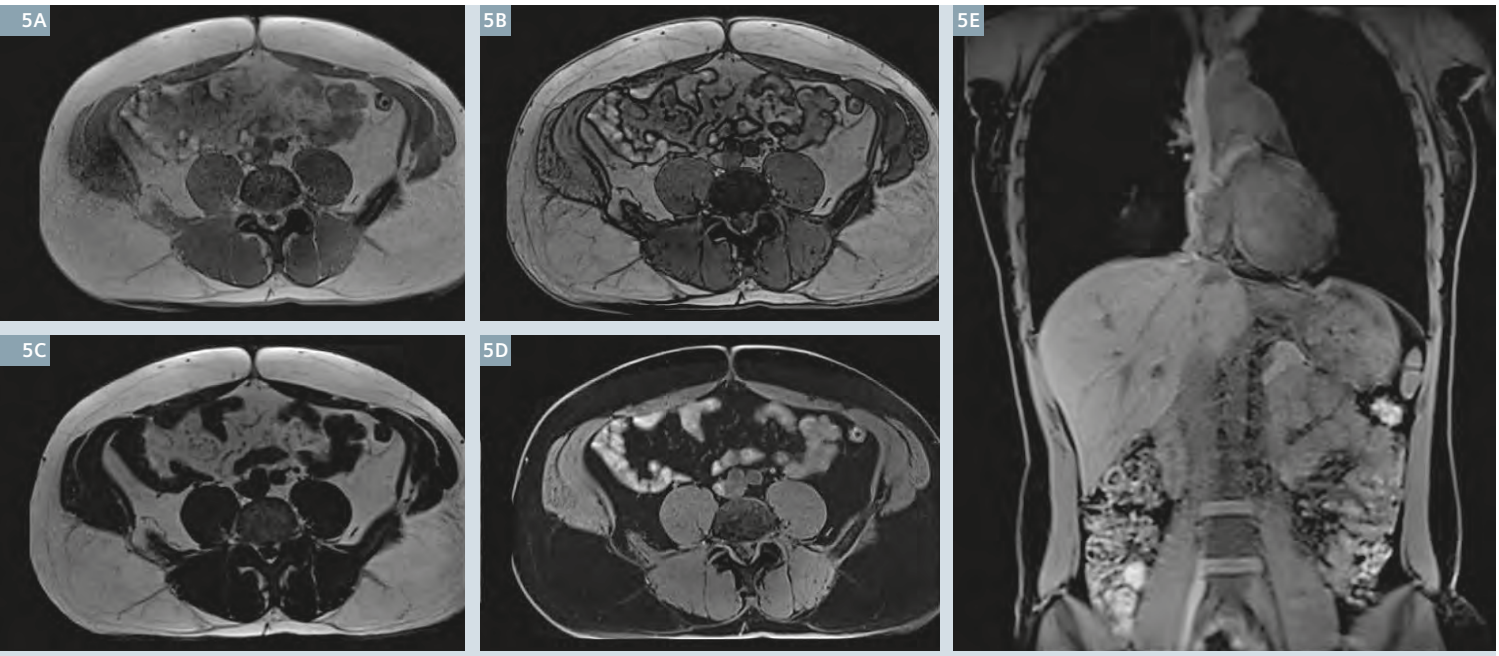

5 Dixon with in-phase, out-of-phase, water and fat only **(5A–D)** images performed at MAGNETOM Prisma. Additionally, demonstration of optimal image homogeneity on coronal orientation **(5E)**. (Sequence details 5A–D: ST 3 mm; TR 3.9 s; TE 1.23 ms / 2.46 ms; Matrix 288 × 187; FOV 40 × 29 cm; 5E: ST 1.6 mm; TR 4.12 s; TE 1.3 ms / 2.6 ms; Matrix 288 × 209; FOV 45 × 36 cm).

of 80 mT/m of MAGNETOM Prisma allow for shorter echo times (TE) and can be reduced to 50 ms in DWI. Thus, more signal can be detected allowing for improved, less noisy images even at high b-values.

In abdominal imaging motion artifacts may be present due to the intrinsic properties and function of abdominal organs (e.g. bowel peristalsis or cardiac motion). Particularly sequences with long acquisition times are prone to motion artifacts. Utilizing parallel imaging techniques, scan times can be reduced if sufficient image quality is maintained. MAGNETOM Prisma uses a new technology, TimTX True Shape, which offers an intelligent interaction of multiple, independent transmit channels. Thus, several high-frequency pulses can be sent in parallel resulting in better image quality and shorter scan times.

Figure 5 gives an example for excellent high-resolution imaging and image quality acquired in a single breath-hold scan with advanced parallel imaging techniques (CAIPRINHA), which benefit from the technical advantages of the MAGNETOM Prisma. Fast parallel imaging in breath-hold technique results in a reduction of motion artifacts and simultaneously in a reduction in the specific absorption rate (SAR). The SAR is a measure for RF energy deposition to the human body. Doubling the field strength to 3T results in quadrupling the RF energy deposition potentially limiting imaging thus any reduction of SAR at 3T is beneficial [14, 18].

In almost all abdominal MR imaging applications a sufficient fat saturation is paramount, especially in contrast-enhanced examinations. Nevertheless, spectral fat saturation techniques may not work well in inhomogeneous tissue volumes due to changes in the precessional frequencies. In abdominal imaging inhomogeneous or insufficient fat saturation often occurs at tissue boundaries or adjacent moving structures. The faster, stronger gradients of the MAGNETOM Prisma in combination with its more homogeneous B_0 field translate into a more homogenous and adequate fat saturation.

Summary

Due to their high SNR and CNR, 3T MRI systems have been established for clinical brain and musculoskeletal imaging over the last years. With respect to abdominal applications, 3T imaging remains challenging given the more difficult conditions associated with the large FOV and amplified image artifacts. Under these circumstances, the disadvantages of standard 3T MRI may outweigh potential advantages.

The new generation MAGNETOM Prisma copes with the said challenges by offering a new system design, and several technical methods to reduce sources of image noise and to optimize image acquisition. With high gradient field strengths and fast slew rates, existing techniques like parallel imaging can be optimally utilized and acquisition time further reduced without a significant loss in signal strength. This further leads to a reduction in motion artifacts and SAR. The increased homogeneities of the B_0 and B_1 fields contribute to a significantly improved image quality and more effective reduction of image noise.

References

1 Sicotte NL, Voskuhl RR, Bouvier S, Klutch R, Cohen MS, Mazziotta JC. Comparison of multiple sclerosis lesions at 1.5 and 3.0 Tesla. Investigative radiology. 2003;38(7):423-7. Epub 2003/06/25.

2 Krautmacher C, Willinek WA, Tschampa HJ, Born M, Traber F, Gieseke J, et al. Brain tumors: full- and half-dose contrast-enhanced MR imaging at 3.0 T compared with 1.5 T-Initial Experience. Radiology. 2005;237(3):1014-9. Epub 2005/10/21.

3 Isoda H, Kataoka M, Maetani Y, Kido A, Umeoka S, Tamai K, et al. MRCP imaging at 3.0 T vs. 1.5 T: preliminary experience in healthy volunteers. Journal of magnetic resonance imaging: JMRI. 2007;25(5):1000-6. Epub 2007/04/06.

4 Michaely HJ, Kramer H, Dietrich O, Nael K, Lodemann KP, Reiser MF, et al. Intraindividual comparison of high-spatial-resolution abdominal MR angiography at 1.5 T and 3.0 T: initial experience. Radiology. 2007;244(3):907-13. Epub 2007/08/22.

5 Koh DM, Collins DJ. Diffusion-weighted MRI in the body: applications and challenges in oncology. AJR American journal of roentgenology. 2007;188(6):1622-35. Epub 2007/05/23.

6 Aja-Fernandez S, Vegas-Sanchez-Ferrero G, Tristan-Vega A. Noise Estimation in Parallel MRI: GRAPPA and SENSE. Magnetic resonance imaging. 2013. Epub 2014/01/15.

7 Chang KJ, Kamel IR, Macura KJ, Bluemke DA. 3.0-T MR imaging of the abdomen: comparison with 1.5 T. Radiographics: a review publication of the Radiological Society of North America, Inc. 2008;28(7):1983-98. Epub 2008/11/13.

8 Barth MM, Smith MP, Pedrosa I, Lenkinski RE, Rofsky NM. Body MR imaging at 3.0 T: understanding the opportunities and challenges. Radiographics : a review publication of the Radiological Society of North America, Inc. 2007;27(5):1445-62; discussion 62-4. Epub 2007/09/13.

9 Roth CJ, Boll DT, Wall LK, Merkle EM. Evaluation of MRI acquisition workflow with lean six sigma method: case study of liver and knee examinations. AJR American journal of roentgenology. 2010;195(2):W150-6. Epub 2010/07/24.

10 Takahashi N, Yoshioka H, Yamaguchi M, Saida Y, Itai Y. Accelerated dynamic MR imaging with a parallel imaging technique for hypervascular hepatocellular carcinomas: usefulness of a test bolus in examination and subtraction imaging. Journal of magnetic resonance imaging: JMRI. 2003;18(1):80-9. Epub 2003/06/20.

11 Koenig SH BR. Relaxation of solvent protons by paramagnetic ions and its dependence on magnetic field and chemical environment: implications for NMR imaging. Magnetic resonance in medicine : official journal of the Society of Magnetic Resonance in Medicine / Society of Magnetic Resonance in Medicine. 1984;1(4):478-95.

12 AD E. How much contrast is enough? dependence of enhancement on field strength and MRpulse sequence. European radiology. 1997;7(5):276-80.

13 Bottomley PA, Andrew ER. RF magnetic field penetration, phase shift and power dissipation in biological tissue: implications for NMR imaging. Physics in medicine and biology. 1978;23(4):630-43. Epub 1978/07/01.

14 Merkle EM, Dale BM, Paulson EK. Abdominal MR imaging at 3T. Magnetic resonance imaging clinics of North America. 2006;14(1):17-26. Epub 2006/03/15.

15 Soher BJ, Dale BM, Merkle EM. A review of MR physics: 3T versus 1.5T. Magnetic resonance imaging clinics of North America. 2007;15(3):277-90, v. Epub 2007/09/26.

16 Cruite I, Schroeder M, Merkle EM, Sirlin CB. Gadoxetate disodium-enhanced MRI of the liver: part 2, protocol optimization and lesion appearance in the cirrhotic liver. AJR American journal of roentgenology. 2010;195(1):29-41. Epub 2010/06/23.

17 Delfaut EM, Beltran J, Johnson G, Rousseau J, Marchandise X, Cotten A. Fat suppression in MR imaging: techniques and pitfalls. Radiographics : a review publication of the Radiological Society of North America, Inc. 1999;19(2):373-82. Epub 1999/04/09.

18 Merkle EM, Dale BM. Abdominal MRI at 3.0 T: the basics revisited. AJR American journal of roentgenology. 2006;186(6):1524-32. Epub 2006/05/23.

19 Lewin JS, Duerk JL, Jain VR, Petersilge CA, Chao CP, Haaga JR. Needle localization in MR-guided biopsy and aspiration: effects of field strength, sequence design, and magnetic field orientation. AJR American journal of roentgenology. 1996;166(6):1337-45. Epub 1996/06/01.

Contact

Caroline Zähringer, M.D.
Department of Radiology and Nuclear Medicine
University Hospital Basel, University of Basel
Petersgraben 4
4031 Basel, Switzerland
Phone +41 62 32 86 913
Fax +41 61 265 53 51
Caroline.Zaehringer@usb.ch

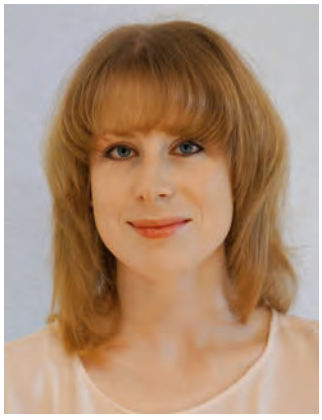

MAGNETOM Prisma is not commercially available in all countries. Due to regulatory reasons its future availability cannot be guaranteed.

An Efficient Workflow for Quantifying Hepatic Lipid and Iron Deposition using LiverLab

Puneet Sharma, Ph.D.; Diego Martin, M.D., Ph.D.

University of Arizona, Department of Medical Imaging, Tucson, AZ, USA

Introduction

Over the last decade, Magnetic Resonance Imaging has shown an excellent ability to detect and quantify diffuse liver disease [1–3]. The primary application has been the clinical evaluation of hepatic steatosis and iron deposition, which may be a pre-cursor of advanced liver disease, such as chronic fibrosis, and HCC. Early detection and therapeutic monitoring are key objectives for preventing and managing liver disease.

It is well-known that MRI is inherently sensitive to both lipid and iron deposition in the liver using conventional in- and opposed-phase T1-weighted 2D FLASH [4–5]. This is also evident with dual-echo 3D Dixon methods, which have gained more use and acceptance recently. However, accurate quantification of lipid and iron components requires compensating for several confounding factors, arising primarily from T1-, T2*-, and lipid resonance-effects. This has been the focus of much investigation recently, with modern methods, such as multi-point 3D Dixon with fat quantification (DIXON FQ), now utilizing a complex signal model for multiple lipid resonances, while simultaneously correcting for relaxation-effects [6–8]. An alternate direct interrogation of lipid-fraction and iron deposition is breath-hold, multi-echo MR spectroscopy (HISTO-MRS) [2]. Though limited to localized quantification, HISTO-MRS has shown to be highly accurate and

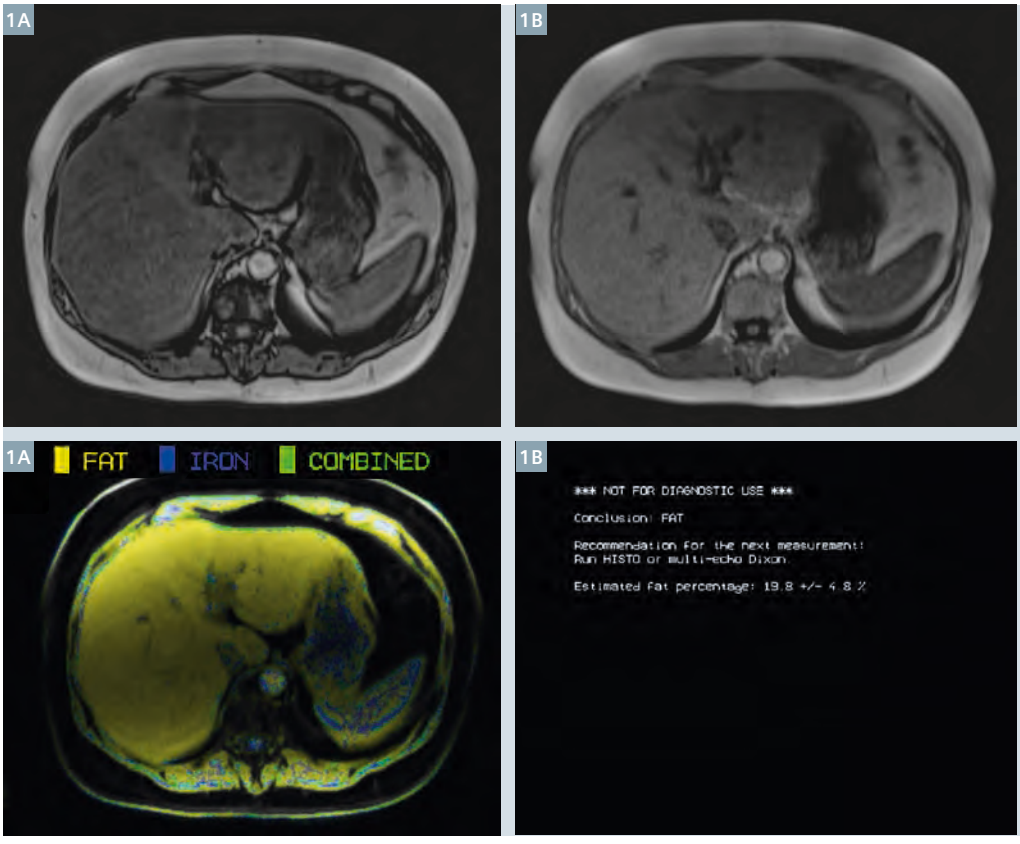

1

Resultant images from one subject using Screening Dixon, acquired in 18 sec (TR 7.17 ms, TE_1 2.4 ms, TE_2 4.8 ms; 288 × 162 matrix; 3 mm thickness; 80 slices).
(1A) Opposed-phase;
(1B) In-phase;
(1C) Result color map overlay on water image;
(1D) Clinical conclusion. Pure water and fat images are also produced (not shown).

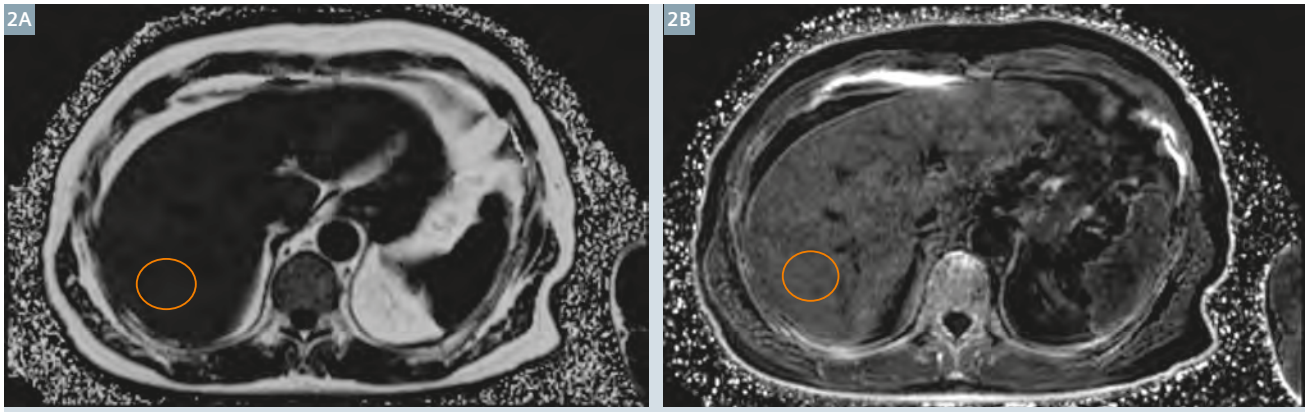

2 Fat percentage **(2A)** and effective R2* maps **(2B)** in one subject using multi-point Dixon FQ. Signal from a region-of-interest shows FP = 11.2%, and R2*eff = 43.7 s^{-1}. Acquisition was performed in an 18 sec breath-hold (TR 9.7 ms; TE = {1.2, 2.4, 4.8, 5.9, 7.1, 8.3} ms; 256 × 154 matrix; 3.5 mm thickness; 64 slices).

reproducible, enabling improved local water and lipid analysis, which may complement and confirm findings from other imaging methods.

Despite the relative ease to implement breath-hold DIXON FQ and HISTO, not all patients for routine abdominal imaging require lipid and/or iron quantification. An effective strategy, therefore, is to incorporate disease 'screening'. Since conventional two-point Dixon techniques are found in most clinical abdominal protocols, an automated signal analysis algorithm on these images can indicate the presence of lipid, iron, or combined disease. This conclusion can then prompt subsequent decisions for quantification. Recently, development of automated screening analysis with two-point Dixon has been described [9–11], and has been termed Screening Dixon in this report.

The liver quantification tools described above have now been introduced as an application package, called 'LiverLab'. All three methods remain in developmental stages**, with additional image outputs generated for quality control purposes. This report describes this initial sequence implementation, along with the workflow and acquisition strategy for integrating hepatic lipid and iron quantification methods in routine clinical abdominal imaging.

**WIP, the product is currently under development and is not for sale in the US and other countries. Its future availability cannot be ensured.

Outline of techniques

Screening Dixon

Many clinical abdominal MRI protocols incorporate a two-point, in- and opposed-phase imaging method into their standard imaging exams. In addition to anatomic images, the inherent sensitivity of chemical-shift images to lipid and iron allows the potential for further screening information, which is the basis for the Screening Dixon technique. Following acquisition, an automated liver sampling algorithm is designed to provide a preliminary analysis for the presence of hepatic lipid, iron, or combined disease. Since the Screening Dixon only uses two echoes, as with conventional chemical-shift imaging, accurate quantification of hepatic lipid and iron deposition is not possible due to known confounding effects. However, 3D coverage, coupled with a colorized map of analysis findings, shows the geographic distribution of the disease, if present. Figure 1 shows an example of the Screening Dixon in the abdomen, along with the resultant images.

Multi-echo Dixon FQ

The multi-point 3D Dixon with lipid and iron quantification (DIXON FQ) includes several features that compensate for confounding effects, namely low flip angle for reducing T1 effects; a multi-fat peak model for robust lipid estimation; and multiple echo acquisitions for R2*/T2* estimation and correction. Typical implementation of the DIXON FQ includes six-echoes, with echo times either set to minimum (flexible) values for a given bandwidth, or to respective in- and opposed-phase values. The former allows a shorter TR, which reduces breath-hold time. The technique is also compatible with CAIPIRINHA acceleration, which allows acceptable coverage and breath-hold times. The resultant volumetric images include a fat percentage (proton density fat fraction, PDFF) map, and a map of effective R2* (inverse of T2*), which is an estimation of iron deposition. This parameter map calculation is based on a pixel-wise non-linear fitting of the multi-echo signals to a signal model that includes water, fat, and effective R2* variables [8]. Additionally, separate water and lipid R2* maps are available, which may provide more information about the compartmental distribution of iron. Figure 2 depicts the DIXON FQ resultant maps from a subject with mildly elevated lipid and relatively normal iron deposition. The signal intensities in the images are proportional to lipid fraction and effective R2*.

HISTO-MRS

A more detailed inspection of lipid fraction and iron content can be achieved with MR spectroscopy. Historically, the utility of MRS techniques in the liver have been limited to triggered, free breathing techniques, lasting several minutes.

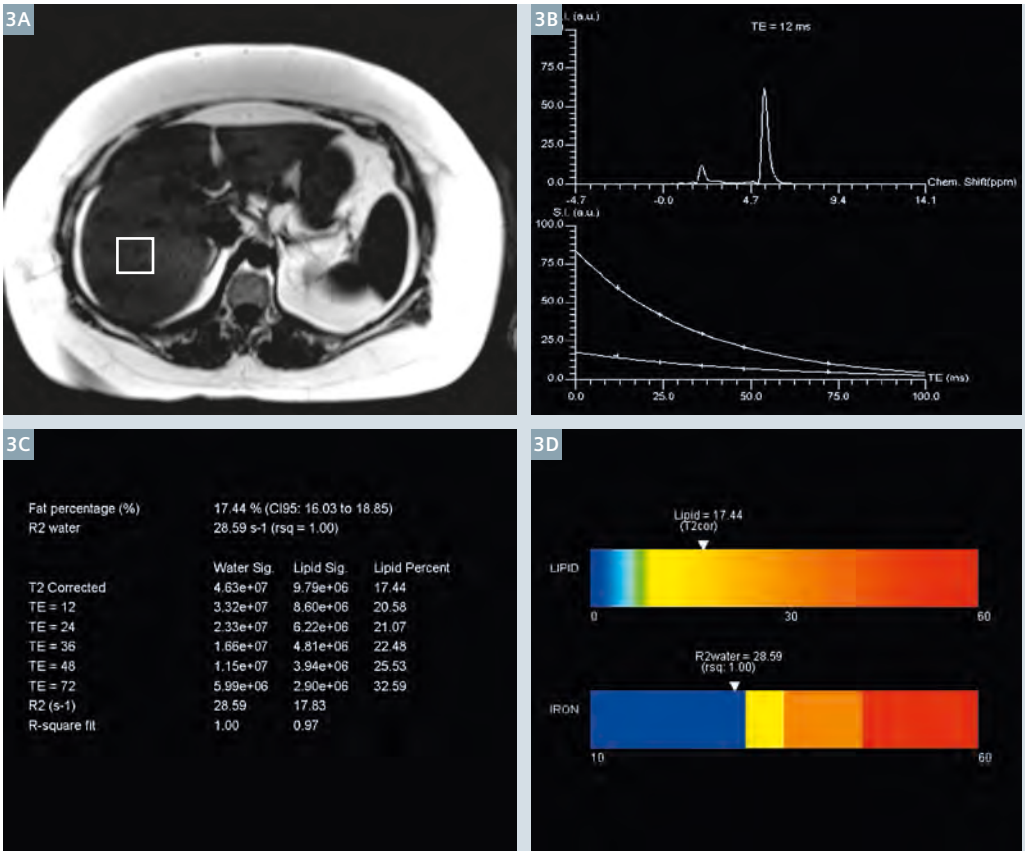

3

Breath-hold HISTO-MRS acquisition in one subject with elevated lipid. **(3A)** Placement of HISTO voxel (27 cc) is performed on a non-distortion-corrected image (multiple orientations prefered). Output images inlude: **(3B)** Spectral peaks at TE 12 ms and T2 curve-fit of lipid and water; **(3C)** a results table of calculated values; and **(3D)** a color bar depicting lipid fraction and $R2_{water}$ (iron) estimates.

4

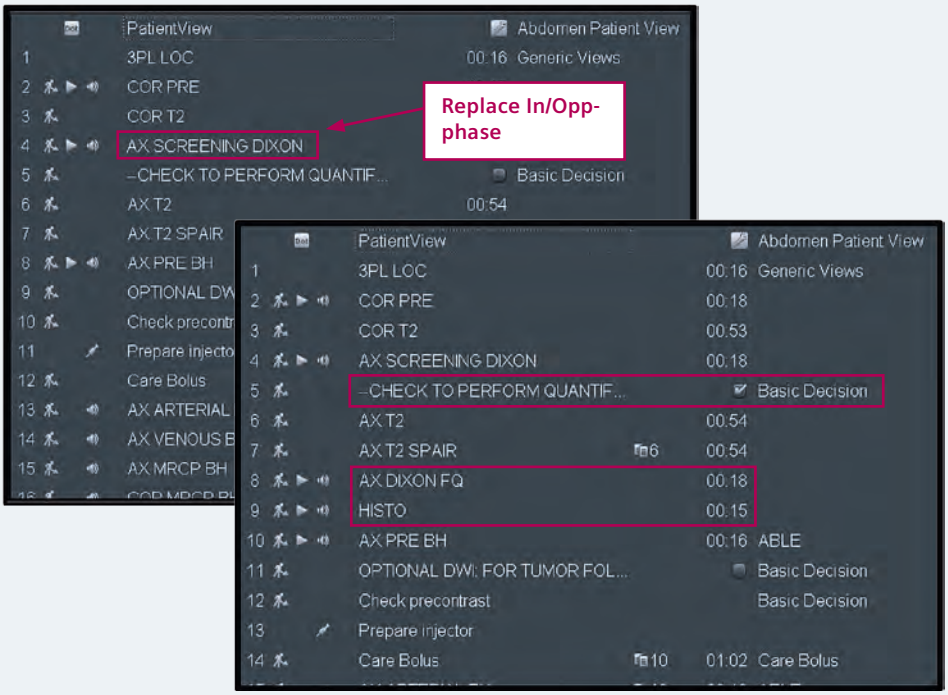

4 Dual echo 3D-VIBE with Screening Dixon evaluation can be inserted in an Abdomen Dot protocol to replace conventional in- and opposed-phase imaging. Following the acquisition step, the user can decide whether to execute quantification, or proceed with routine exam based upon the Screening Dixon results. Note the insertion of Dixon FQ and HISTO upon activating the decision step. The decisions and quantification sequences can be inserted anywhere in the queue to optimize exam workflow.

Due to the lack of water suppression, and the relatively high abundance of lipid (when present), particularly at 1.3 (methylene) and 2.1 ppm (carboxyl), the signal-to-noise ratio of single-voxel MRS is substantial over other metabolic applications. This idea allows the application of a voxel region-of-interest with only one signal-average, drastically reducing acquisition time. To alleviate T1 effects, a long TR is prescribed (TR = 3000 ms), while T2 effects are overcome by repeat (concatenated) acquisitions with a total of five echo times, such as TE = {12, 24, 36, 48, 72} ms. Reconstruction and post-processing of HISTO-MRS is inline and simplified to present data quickly and without complex user-interaction. Lipid-fraction is determined from the ratio of total lipid signal to total voxel (water + lipid) signal. For more accurate results, however, 'proton-density' lipid-fraction value using T2-correction can be determined from an exponential fit of the five-echo signal decay. In addition, the reciprocal T2-estimation of water ($R2_{water}$) provides a close correlation with iron content, as described in previous phantom and *in vivo* studies [2, 12]. $R2_{water}$ also does not show sensitivity to lipid content, which may obscure iron measurements in some imaging methods that do not discriminate R2* compartments. Figure 3 depicts the prescription and output from a 15-second breath-hold HISTO-MRS acquisition.

Integration with Dot / clinical protocol

Integrating the components of LiverLab into a clinical abdominal protocol lends well to the versatility of the Abdomen Dot Engine. This workflow allows the user to define exam strategies, patient context options, and clinical decision points. Though these workflow tools afford many variations for integrating specialized applications, such as LiverLab, an initial step involves substituting the conventional T1-weighted in- and opposed-phase acquisition with the two-point 3D Screening Dixon method (Fig. 4). Since this acquisition 'screens' the subject for lipid and iron deposition with an automated inline post-processing step, no prior knowledge of diffuse disease is necessary. The subsequent step requires a user decision based on the Screening Dixon conclusion: "perform quantification", or "proceed with routine exam". This can be accomplished with a clinical decision point step; a Dot add-in checkbox can be inserted in the exam queue that toggles the quantification step (Fig. 4). From a positive screening result, the multi-point Dixon FQ can be selected and performed in the same abdominal location to generate fat percentage and R2* maps for subsequent analysis. Alternatively, HISTO-MRS can be performed for additional information of a specified location, especially if non-geographic variation is revealed. This step may also be elicited from a clinical

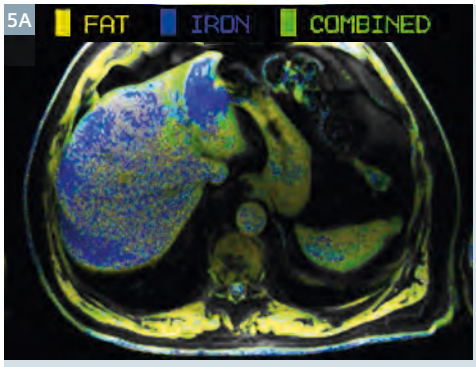

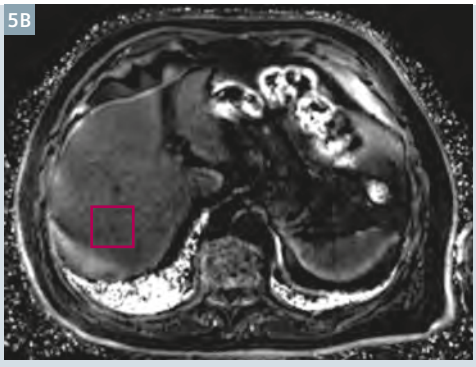

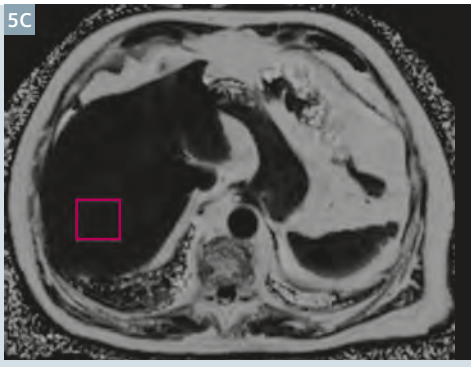

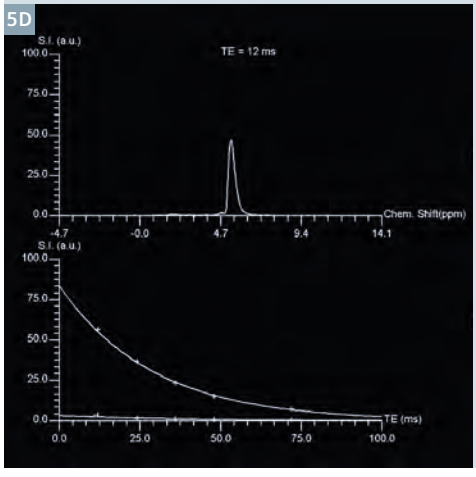

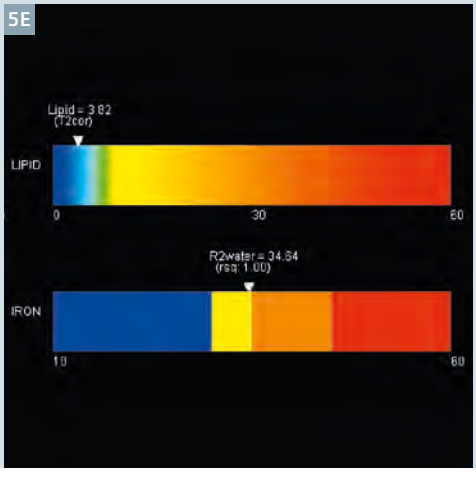

5

77-year-old male with intraductal papillary mucinous neoplasm. **(5A)** Screening Dixon reveals the conclusion of iron deposition; **(5B)** and **(5C)** Regional analysis of multi-point Dixon FQ shows R2*eff= 63.5 s^{-1} and lipid faction (FF) = 5.5%. **(5D)** and **(5E)** Subsequent HISTO reveals similar findings, LF = 3.8% and $R2_{water}$ = 34.6 s^{-1}, which is evidence of mildly elevated iron. (Measurements perfomed at 1.5T MAGNETOM Avanto.

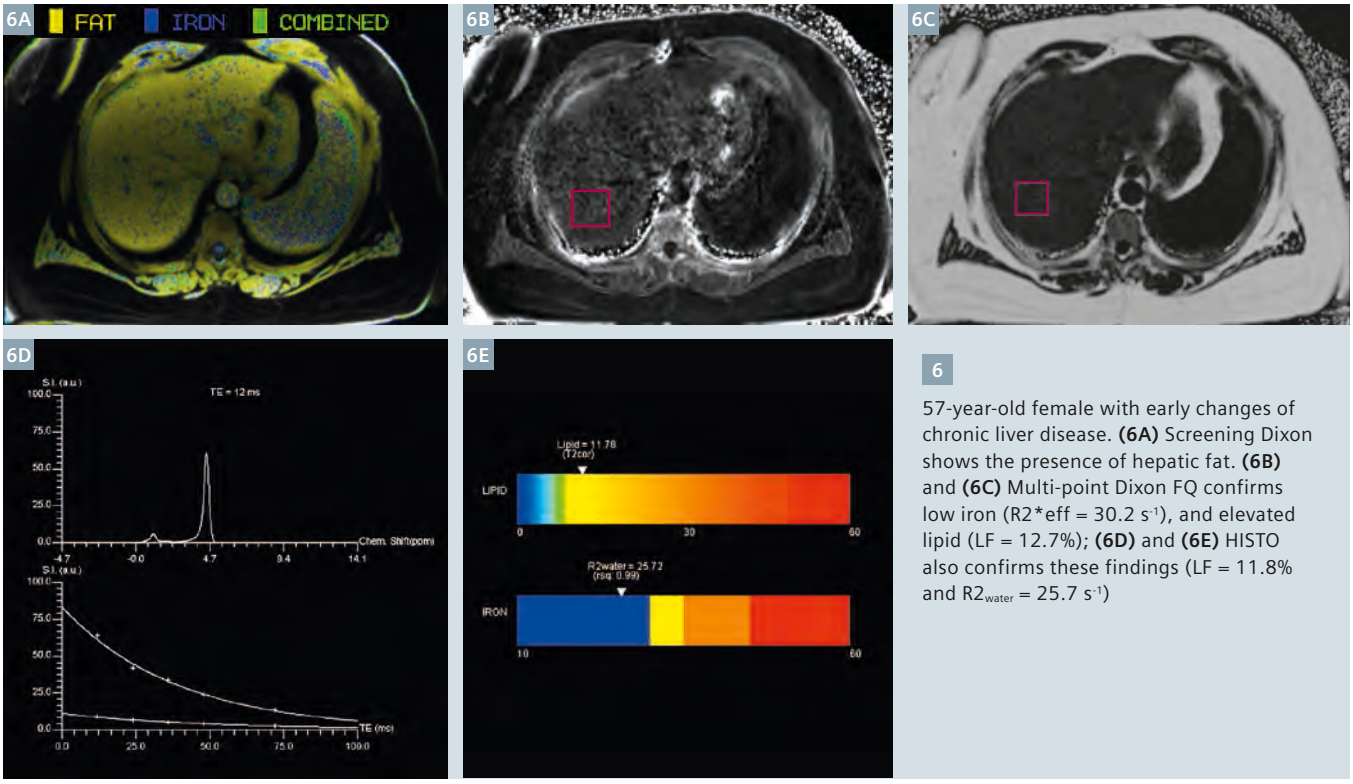

6

57-year-old female with early changes of chronic liver disease. **(6A)** Screening Dixon shows the presence of hepatic fat. **(6B)** and **(6C)** Multi-point Dixon FQ confirms low iron (R2*eff = 30.2 s^{-1}), and elevated lipid (LF = 12.7%); **(6D)** and **(6E)** HISTO also confirms these findings (LF = 11.8% and $R2_{water}$ = 25.7 s^{-1})

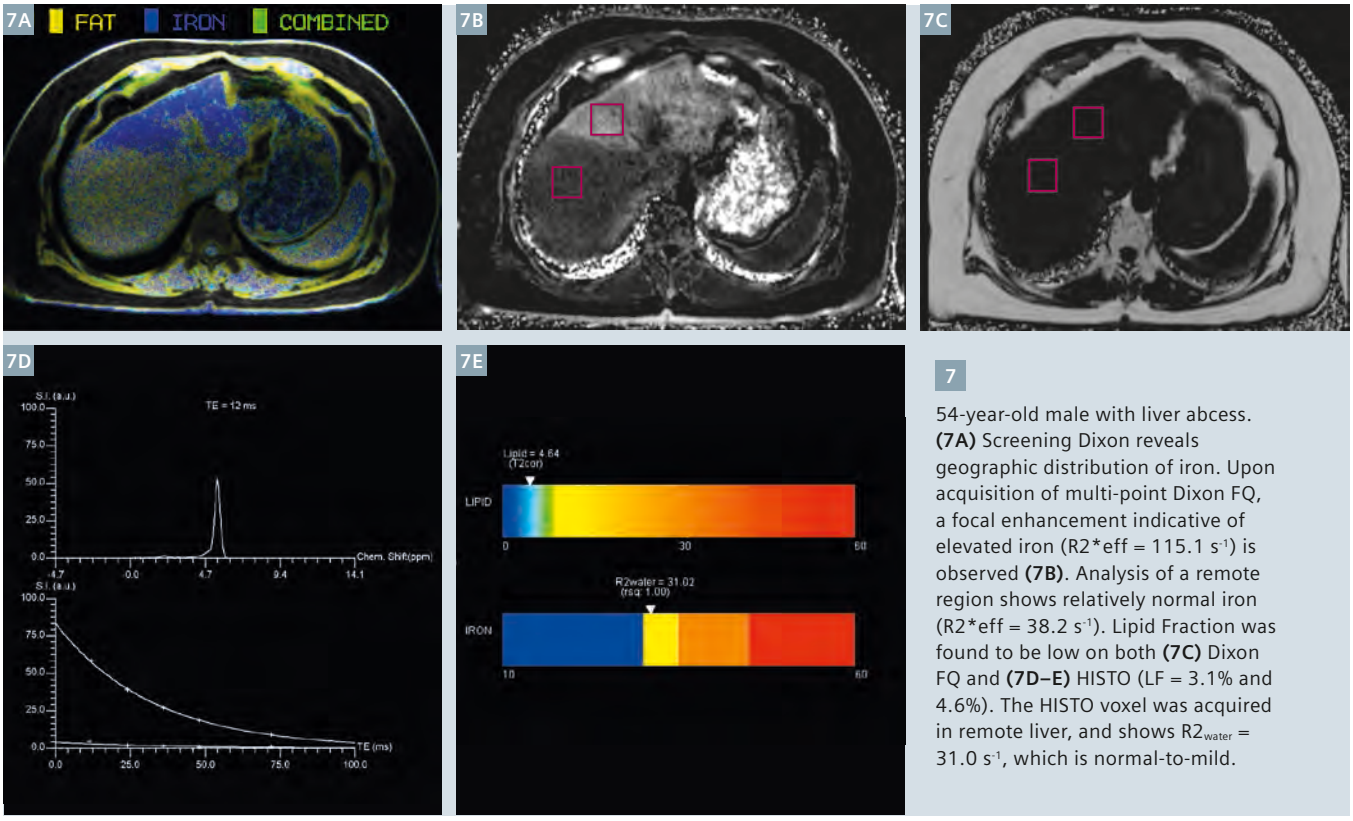

7

54-year-old male with liver abcess. **(7A)** Screening Dixon reveals geographic distribution of iron. Upon acquisition of multi-point Dixon FQ, a focal enhancement indicative of elevated iron (R2*eff = 115.1 s^{-1}) is observed **(7B)**. Analysis of a remote region shows relatively normal iron (R2*eff = 38.2 s^{-1}). Lipid Fraction was found to be low on both **(7C)** Dixon FQ and **(7D–E)** HISTO (LF = 3.1% and 4.6%). The HISTO voxel was acquired in remote liver, and shows $R2_{water}$ = 31.0 s^{-1}, which is normal-to-mild.

decision-point configuration. HISTO-MRS is akin to prescribing a ~27 cc ROI in the liver for simultaneous lipid-fraction and iron ($R2_{water}$) estimation, without additional post-processing.

Clinical experience, results, examples

Our institution has implemented and tested the LiverLab workflow with our routine clinical Abdomen Dot protocol. The use of two-point Screening Dixon improves exam efficiency and through-plane resolution, compared to conventional multi-breath-hold, 2D in- and opposed-phase FLASH, while also providing immediate insight into the presence of hepatic lipid and iron deposition. In our initial implementation, we acquired both the multi-point Dixon FQ and HISTO-MRS in two additional breath-holds, based on the screening result. Figures 5–7 show examples of three clinical cases utilizing LiverLab within the Abdomen Dot workflow. The initial assessment using Screening Dixon correlates well with the analysis of subsequent quantification methods. Moreover, there is strong agreement between Dixon FQ and HISTO-MRS results in the examples.

Conclusion

Rapid quantification of diffuse liver disease related to metabolic syndromes, such as lipid and iron accumulation, is now possible with LiverLab. By integrating the 2-point Screening Dixon acquisition into the routine Abdomen Dot protocol, immediate assessment of lipid and iron deposition can be achieved. Inline decision-points can be configured to prompt subsequent quantification steps, which include multi-point Dixon FQ and HISTO-MRS. These quantification methods provide diagnostic information on a global- or region-specific-basis, with strong correlation.

References

1 Reeder SB, Robson PM, Yu H, et al. Quantification of hepatic steatosis with MRI: the effects of accurate fat spectral modeling. J Magn Reson Imaging 2009; 29:1332–1339.

2 Pineda N, Sharma P, Xu Q, Hu X, Vos M, Martin DR. Measurement of hepatic lipid: high-speed T2-corrected multiecho acquisition at 1H MR spectroscopy–a rapid and accurate technique. Radiology 2009; 252:568–576.

3 Meisamy S, Hines CD, Hamilton G, et al. Quantification of hepatic steatosis with T1-independent, T2-corrected MR imaging with spectral modeling of fat: blinded comparison with MR spectroscopy. Radiology 2011; 258:767–775.

4 Dixon WT. Simple proton spectroscopic imaging. Radiology 1984; 153:189–194.

5 Stark DD, Moseley ME, Bacon BR, et al. Magnetic resonance imaging and spectroscopy of hepatic iron overload. Radiology 1985; 154:137–142.

6 Bydder M, et al. Relaxation effects in the quantification of fat using gradient echo imaging. Magn Reson Imaging 2008;26:347-359.

7 Hernando D, Liang ZP, Kellman P. Chemical shift-based water/fat separation: a comparison of signal models. Magn Reson Med 2010; 64:811–822.

8 Zhong X, Nickel MD, Kannengiesser SA, Dale BM, Kiefer B, Bashir MR. Liver fat quantification using a multi-step adaptive fitting approach with multi-echo GRE imaging. Magn Reson Med 2013; doi: 10.1002/mrm.25054. [Epub ahead of print].

9 Bashir MR, Dale BM, Merkle EM, Boll DT. Automated liver sampling using a gradient dual-echo dixon-based technique. Magn Reson Med. 2012 May;67(5):1469-77.

10 Bashir MR, Merkle EM, Smith AD, Boll DT. Hepatic MR imaging for *in vivo* differentiation of steatosis, iron deposition and combined storage disorder: Single-ratio in/opposed phase analysis vs. dual-ratio Dixon discrimination. Eur J Radiol 2012;81(2):e101-e109.

11 Bashir MR, Zhong X, Dale BM, Gupta RT, Boll DT, Merkle EM. Automated patient-tailored screening of the liver for diffuse steatosis and iron overload using MRI. AJR Am J Roentgenol. 2013 Sep;201(3):583-8.

12 Sharma P, Martin DR, Pineda N, et. al. Quantitative analysis of T2-correction in single-voxel magnetic resonance spectroscopy of hepatic lipid fraction. J Magn Reson Imaging 2009; 29:629-635.

Contact

Puneet Sharma, Ph.D.
Department of Medical Imaging
University of Arizona
Phone: +1 520-626-7965
puneets@radiology.arizona.edu

Case Study LiverLab

Stephan Kannengiesser, Ph.D.[1]; Radhouene Neji, Ph.D.[1]; Xiaodong Zhong, Ph.D.[2]

[1]Siemens Healthcare, MR Oncology Applications, Erlangen, Germany
[2]Siemens Healthcare, MR R&D Collaborations, Atlanta, GA, USA

Measurement data of a 22-year-old male volunteer with elevated liver fat signal, acquired on a 3T MAGNETOM Skyra system, were processed with the *syngo* MR E11A* implementation of LiverLab*.

The measurement program includes a regular opposed-phase / in-phase two-point Dixon protocol with water/fat separation. The First look Dixon processing first performs a liver segmentation on the water series, and then a voxel classification according to the dual-ratio Dixon signal discrimination [1]. This leads to the conclusion of fat deposition and the recommendation to run additional quantification (Fig. 1).

The *syngo* MR E11A Abdomen Dot framework uses this recommendation to implement a decision point, through which the user can add the quantification protocols to the measurement queue. In addition, the Dot engine allows specifying an inline region-of-interest (ROI) during protocol planning. The multi-echo VIBE Dixon [2] produces inline parameter maps of fat signal percentage (proton density fat fraction, PDFF) and effective R2*, with overlays of the liver segmentation region and pre-planned ROI. Statistics (mean, std) of PDFF and effective R2* over the ROI and segmentation region are calculated inline, and are output as a report sheet, showing values both in text form and as color bars. Likewise, histograms are produced for PDFF and effective R2* over the segmentation region (Fig. 2).

A HISTO (high-speed T2-corrected multi-echo single voxel spectroscopy, [3]) protocol was also run, with 5 TEs ranging from 12 to 72 ms, and a voxel of size $3 \times 3 \times 3 cm^3$. The HISTO inline processing integrates over the water and fat parts of the spectrum for the individual echoes, and performs a T2 relaxation correction. Results include a fat signal percentage and the R2 of water ($R2_{water}$), which are displayed in textual and color bar formats. A spectrum of the shortest TE and a list of quantification values for the individual echoes are added for quality control of the signal fitting. The inline analysis for this case reveals similar findings as the multi-echo VIBE Dixon (Fig. 3).

*WIP, the product is currently under development and is not for sale in the US and other countries. Its future availability cannot be ensured.

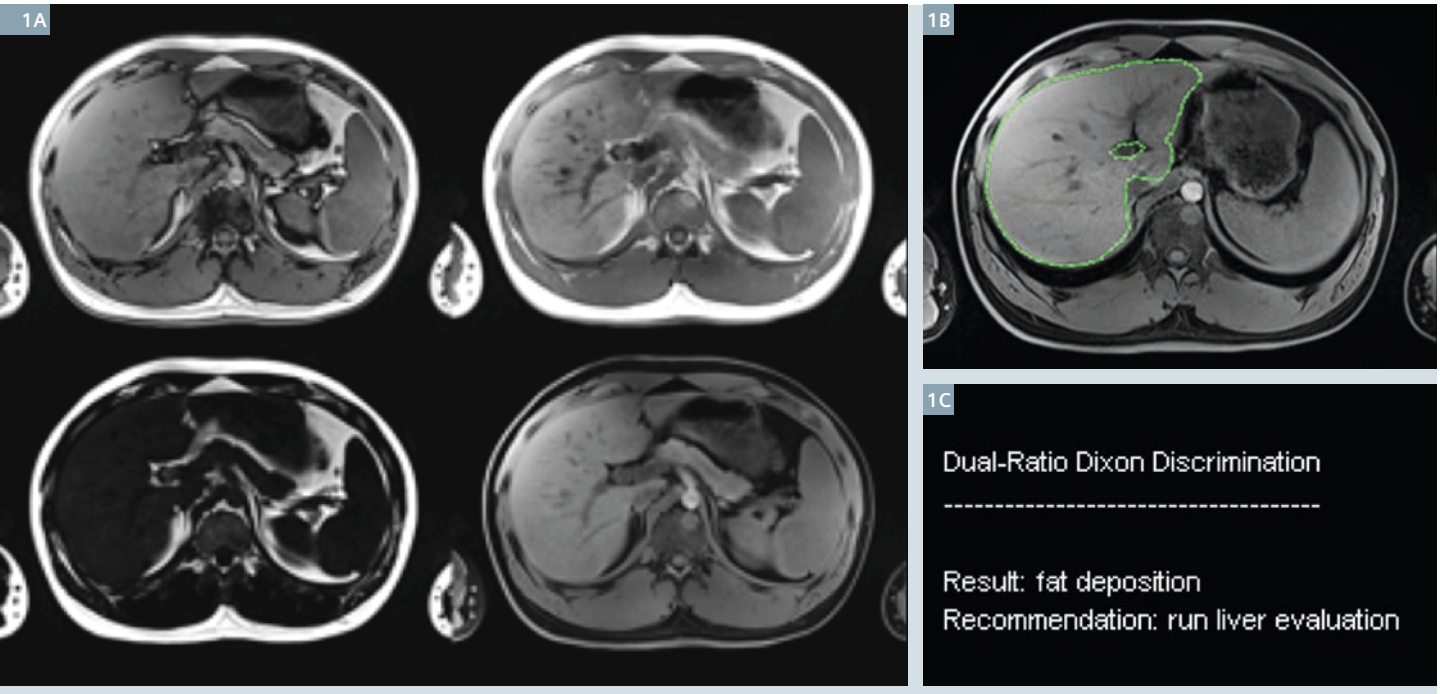

1 First look Dixon (Screening Dixon) results: **(1A)** opposed-phase, in-phase, fat, and water images, **(1B)** liver segmentation, **(1C)** report sheet.

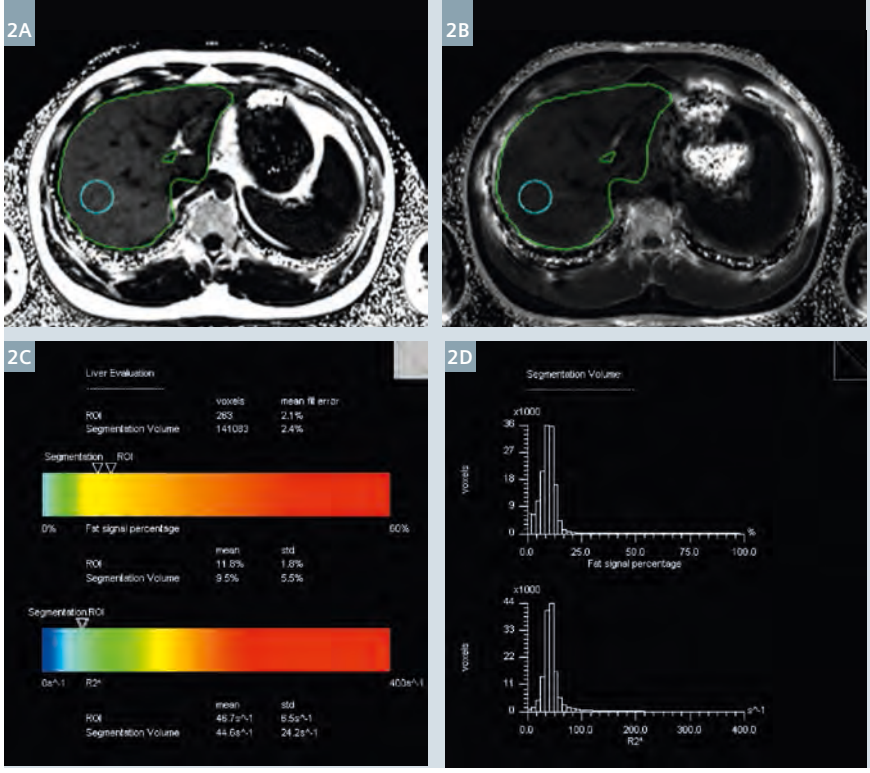

2

Multi-echo Dixon results: **(2A)** PDFF and **(2B)** effective R2* maps with overlays of the inline liver segmentation region (green) and inline ROI (cyan). **(2C)** Inline statistics (mean, std) of PDFF and effective R2* over ROI and segmentation region as text and color bar. The mean ROI values are fat signal percentage 11.8% and effective R2* 46.7 s^{-1}. **(2D)** Histograms of PDFF and effective R2* over the segmentation region.

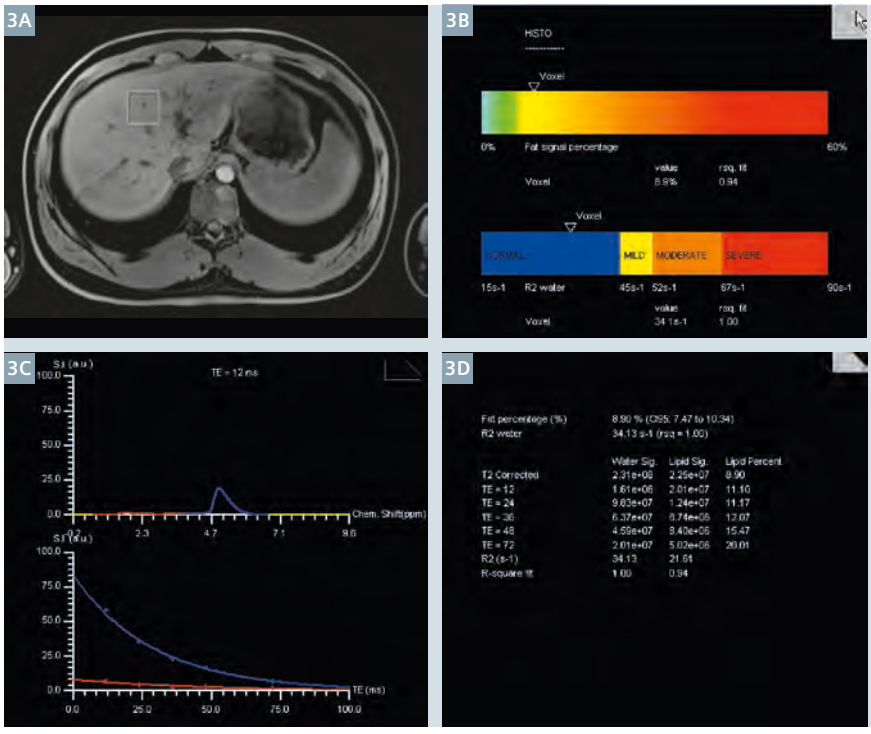

3

HISTO results: **(3A)** Voxel location (from the spectroscopy task card), **(3B)** report sheet. The values are fat signal percentage 8.9%, $R2_{water}$ 34.1 s^{-1}. **(3C)** Spectrum at shortest TE, **(3D)** list of individual echo values. For comparison, a manually drawn ROI on the multi-echo Dixon parameter maps, co-localized with the HISTO voxel position shown in A), reveals PDFF 8.9%, and effective R2* 44.3 s^{-1}.

References

1 Bashir MR, Merkle EM, Smith AD, Boll DT. Hepatic MR imaging for in vivo differentiation of steatosis, iron deposition and combined storage disorder: Single-ratio in/opposed phase analysis vs. dual-ratio Dixon discrimination. Eur J Radiol 2012;81(2):e101-e109.

2 Zhong X, Nickel MD, Kannengiesser SA, Dale BM, Kiefer B, Bashir MR. Liver fat quantification using a multi-step adaptive fitting approach with multi-echo GRE imaging. Magn Reson Med 2013; doi: 10.1002/mrm.25054. [Epub ahead of print]

3 Pineda N, Sharma P, Xu Q, Hu X, Vos M, Martin DR. Measurement of hepatic lipid: high-speed T2-corrected multiecho acquisition at 1H MR spectroscopy – a rapid and accurate technique. Radiology 2009; 252:568–576.

Contact

Stephan Kannengiesser
Siemens Healthcare
MR PI TIO ONCO
Postbox 32 60
91050 Erlangen , Germany
Phone: +49 (1525) 4689516
stephan.kannengiesser@siemens.com

CAIPIRINHA in Gadoxetic Acid-Enhanced Liver MRI: Can We Clarify the Hepatic Arterial Phase?

Chang Hee Lee, M.D.; Yang Shin Park, M.D.

Department of Radiology, Korea University Guro Hospital, Korea University College of Medicine, Seoul, Korea

Introduction

The arterial dominant phase has been accepted as an essential and most important phase for the characterization of focal liver lesions, especially in patients with chronic liver disease. This phase is currently achieved using 3-dimensional (3D) 'Gradient Recalled Echo' (GRE) imaging with fat suppression. Breath-hold T1-weighed volumetric GRE sequences ('Volumetric Interpolated Breath-hold Examination', VIBE) allow motion-free acquisition of diagnostic quality images within a single breath-hold period of up to 20 seconds in most patients [1, 2].

Image quality highly depends on the breath-holding capability of the patients. Therefore a short acquisition time is highly important for liver MRI. The partially parallel acquisition technique generated high-speed imaging. Among the recently developed parallel imaging techniques, 'Controlled Aliasing In Parallel Imaging Results In Higher Acceleration' (CAIPIRINHA) is a promising algorithm that allows a further reduction in image acquisition time while maintaining resolution [3, 4]. It is based on a modification of the undersampling method used in

Table 1:

	Group 1	Group 2	Group 3	Group 4
Temporal matching of data acquisition	Fixed scan (20 s delay)	Bolus triggering	Bolus triggering	Bolus triggering
Contrast injection rate	2 ml/s hand injection	1 ml/s automatic injector	1 ml/s automatic injector	1 ml/s automatic injector
MR system	3T (MAGNETOM Trio, a Tim system; Siemens Healthcare)	3T (MAGNETOM Trio, a Tim system; Siemens Healthcare)	3T (MAGNETOM Skyra; Siemens Healthcare)	3T (MAGNETOM Skyra; Siemens Healthcare)
MR parameters				
TR (ms)	3.37	3.38	3.19	4.12
TE (ms)	1.23	1.23	1.47	1.74
Flip angle (°)	10	10	11	9
Slice thickness (mm)	3, 2	3	3.3	3.5
Number of signal averages	1	1	1	1
Matrix	256 × 157	256 × 157	320 × 240	320 × 182
Field-of-view	285 × 285	278 × 278	285 × 285	348 × 350
Acceleration factor	2	2	2	4
Delta shift	NA	NA	NA	1
Acquisition time (s)	20	18	18	13
k-space	Linear	Centric-ordered	Linear	Segmented linear

Scanning method for gadoxetic acid-enhanced dynamic liver MRI of each group.

the 'GeneRalized Auto calibrating Partially Parallel Acquisition' (GRAPPA) technique.

Generally, 2-dimensional (2D) parallel imaging accelerates data acquisition in the phase- and partition-encoding directions simultaneously, whereas the commonly used 1-dimensional (1D) parallel imaging accelerates data acquisition in the phase-encoding direction. In 2D CAIPIRINHA, in addition to the standard 2D parallel imaging, the acquisition pattern is modified by shifting the sampling positions from their original locations with respect to each other in the partition-encoding direction, which is called a delta shift [3]. Shifting the sampling positions so that sensitivity variations in the receiver coil array are exploited more efficiently results in an improvement in parallel imaging reconstruction.

Therefore, the use of CAIPIRINHA provides better image quality and allows the use of higher acceleration factors. It reduces the acquisition time more effectively than the standard 1D and 2D parallel imaging techniques do and can be applied to 3D volume imaging [3, 4].

Gadoxetic acid (EOB) is now widely used for its added value during the hepatobiliary phase [5-7]. However, poor image quality has been reported on the arterial dominant phase of the dynamic liver MRI more frequently using gadoxetic acid than using other extracellular gadolinium contrast agents [8]. The lower dose of gadoxetic acid results in a short duration of injection, which leads to an abrupt change of gadolinium concentration during *k*-space filling in the hepatic arterial phase, narrowing the time window for optimal imaging. In addition, acute transient dyspnea has been reported significantly more often than with gadobenate dimeglumine [8-10]. However, in our experience, the incidence of spoiled arterial phase was different. In the period of initial use, overall 10% was developed. We have not observed any case of severely degraded arterial dominant phase of GD-EOB-DTPA-enhanced liver MRI [11].

Therefore, the purpose of this paper was to evaluate the feasibility and technical quality of an abdominal 3D VIBE MR examination using the new parallel acquisition technique, CAIPIRINHA, and to determine whether CAIPIRINHA technique could improve the image quality of the hepatic arterial phase of gadoxetic acid-enhanced liver MR imaging.

1

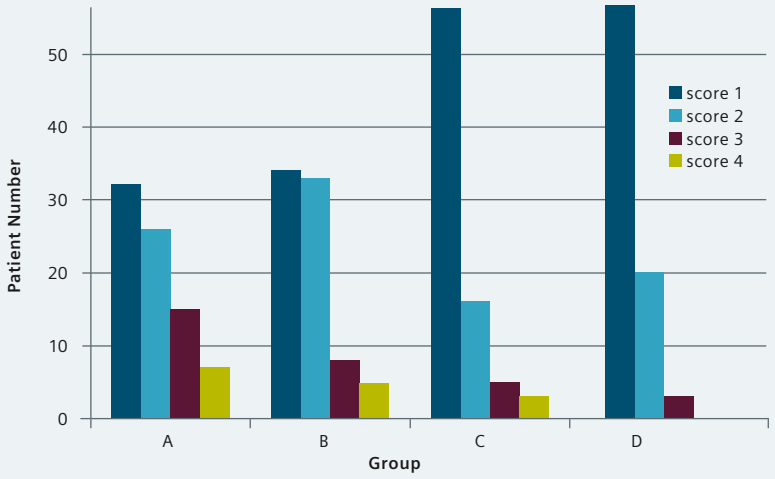

1 Frequency of image quality scores among the 4 groups.

Materials and methods

Subjects

This retrospective study was approved by the Institutional Review Board, and the requirement for informed consent was waived. We retrospectively enrolled a total of 320 eligible patients (198 men and 122 women; mean age, 58.8 ± 12.0 years; age range, 26–85 years) who underwent gadoxetic acid-enhanced liver MRI using different protocols on different systems during separate time periods. From January 2008 to March 2008, 80 patients underwent an examination using a conventional protocol on a standard 3T MRI system (group A); from July 2010 to September 2010, 80 patients underwent an examination using an optimized protocol with a standard 3T MRI system (group B); during July 2012, 80 patients underwent an examination using an optimized protocol and a newer 3T MRI system (group C); and during January 2013, 80 patients underwent an examination using a combination of an optimized protocol and the CAIPIRINHA technique on a newer 3T MRI system (group D).

MR imaging

All patients underwent MRI on one of two kinds of 3T MR systems. A standard 3T MRI machine (MAGNETOM Trio a Tim System; Siemens Healthcare, Erlangen, Germany) with a standard 6-channel body matrix coil and table-mounted 6-channel spine matrix coil had been employed for groups A and B; a newer 3T MRI machine (MAGNETOM Skyra; Siemens Healthcare, Erlangen, Germany) with a standard 18-channel body matrix coil and table-mounted 32-channel spine matrix coil had been employed for groups C and D.

For dynamic imaging, a T1-weighted 3D spoiled GRE sequence with fat saturation and VIBE images was acquired before and after the administration of an intravenous bolus of 0.1 ml/kg of gadoxetic acid (Primovist; Bayer Pharma AG, Berlin, Germany) through a 20- to 22-gauge antecubital venous catheter. The sequence parameters are summarized in Table 1. The hepatic arterial phase was defined differently depending on the group. For group A, the arterial phase acquisition commenced after a fixed scan delay of 20 s after the hand injection of con-

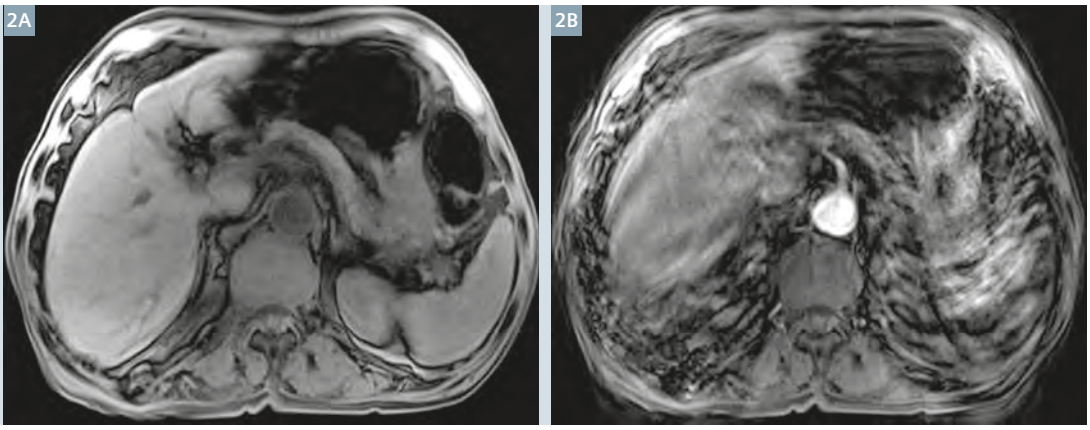

2

77-year-old male patient with liver cirrhosis from group C. **(2A, B)** Pre-contrast scan and hepatic arterial phase were obtained using a standard VIBE sequence during an 18 s breath-hold. Compared to the pre-contrast image, the hepatic arterial phase is degraded by severe artifacts, especially by a severe respiratory motion artifact.

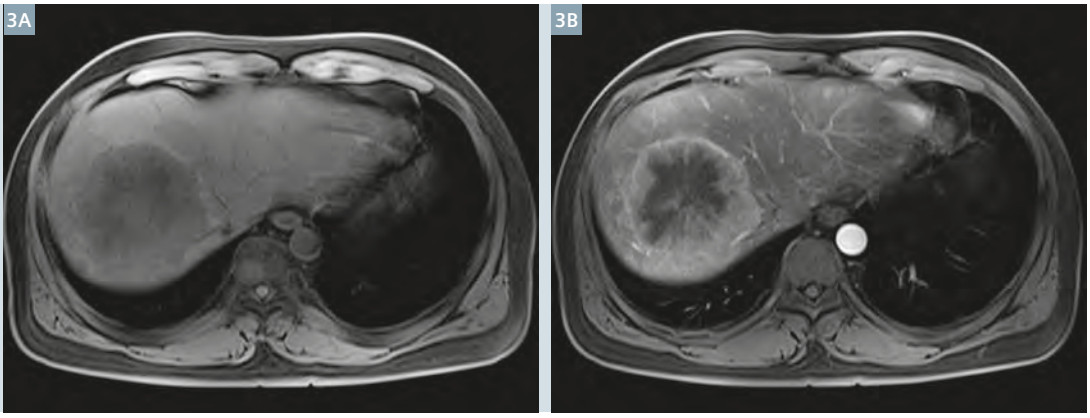

3

52-year-old male patient with hepatitis B from group D. **(3A, B)** Compared to the pre-contrast image, the hepatic arterial phase with CAIPIRINHA obtained during a 13 s breath-hold shows good image quality without any artifacts.

trast medium at a rate of 2 ml/s, followed by a 25 ml saline flush. For groups B–D, the arterial phase was ascertained using the bolus tracking method after the start of a mechanical contrast injection (Spectris MR; Medrad Europe, Maastricht, Netherlands) at a rate of 1 ml/s, followed by a 25 ml saline flush. Under real-time monitoring, arterial phase scanning was initiated immediately after the arrival of the contrast medium in the descending thoracic aorta for groups B and C. For group D, arterial phase scanning began immediately after the arrival of the contrast medium at the aortic arch. CAIPIRINHA-VIBE used a separate calibration scan to determine the coil sensitivity variation and to calculate the full field-of-view without aliasing, whereas the standard VIBE (GRAPPA) sequence for groups A–C used integrated calibration or autocalibration. Thus, the calibration scan for CAIPIRINHA-VIBE is separate from the acceleration scans, but requires only minimal additional time (approximately 3 s). The total breath-hold time for the hepatic arterial phase is approximately 13 s, which includes the 3 s calibration time and the 10 s acceleration time.

Portal venous phase, equilibrium phase, and hepatobiliary phase images were acquired 70 s, 2 min, and 20 min, respectively, after the injection of contrast medium for all patients.

In our study, the CAIPIRINHA technique was used with an acceleration factor of 4 (2 × 2) and a delta shift of 1, which includes 2-fold acceleration in the phase-encoding direction, 2-fold acceleration in the partition-encoding direction, and a reordering shift of 1 corresponding to a relative shift of the 2 neighboring acquired partition-encoding lines.

Image analysis

For the evaluation of hepatic arterial phase image quality, 2 radiologists (C. H. L. and Y. S. P., with 17 and 5 years of experience in abdominal imaging, respectively) blinded to the MR technique independently reviewed the hepatic arterial phase images and assigned a numeric image quality score using a 4-point rating scale. The scoring was as follows:
1 point, no artifacts;
2 points, mild artifacts with no effect on diagnostic quality;
3 points, moderate artifacts, but without a severe effect on diagnostic quality; and
4 points, non-diagnostic images with severe artifacts.

Statistical analysis

Differences in median image quality scores on the hepatic arterial phase among the 4 groups were assessed by using a Kruskal-Wallis test followed by the Dunn procedure for multiple comparisons. Statistical analyses were performed using commercially available software (SPSS, version 20.0, SPSS, Chicago, IL, USA; MedCalc, MedCalc Software, Mariakerke, Belgium).

Results and discussion

In terms of the patients' characteristics, there were no significant differences in age, sex, or the presence of liver

cirrhosis or ascites among groups A, B, C, and D (P = 0.674, 0.213, 0.076, and 0.055, respectively).

For the image quality scores of the hepatic arterial phase, agreement between the 2 observers was robust (weighted κ = 0.847). The median image quality score was 2 in groups A and B and 1 in groups C and D. Scores of 4 points (non-diagnostic images with severe artifacts) were observed in all groups except group D: 7 in group A, 5 in group B, and 3 in group C (Fig. 1). With optimized protocols and advanced techniques, the median image quality score decreased significantly from group A to group D (P = 0.0001), indicating that image quality was improved from group A to group D (Figs. 2, 3). The median image quality score was significantly lower in group D than in groups A and B (P = 0.0001 and 0.001, respectively). Additionally, group C showed a significantly lower median score than groups A and B (P = 0.0001 and 0.003, respectively). However, the median image quality score was not significantly different between groups A and B or between groups C and D (P = 0.448 and 0.656, respectively) (Fig. 4).

Respiratory motion artifacts are one of the major causes of image degradation in the hepatic arterial phase of dynamic-enhanced liver MRI. Currently, reducing scan time seems to be the best solution for avoiding the detrimental effects of respiratory motion. Our study demonstrated that using the CAIPIRINHA technique reduced the overall acquisition time from 20 s to 13 s (up to a 35% reduction in acquisition time), and shortened the breath-holding time (up to a 35% reduction) required to obtain arterial phase imaging. Using the CAIPIRINHA technique decreased the number of non-diagnostic arterial phase images and improved the general image quality of the hepatic arterial phase, although not to a significant extent when compared with an optimized protocol on a newer scanner.

In the past, degraded hepatic arterial phase images were more frequently observed on gadoxetic acid-enhanced liver MRI than with other gadolinium-based contrast agents [8, 12]. Image degradation caused by the narrow time window for precise arterial phase timing due to the small volume of gadoxetic acid might be prevented by optimized protocols, such as the test bolus technique, the bolus tracking technique, and a lower injection rate [6, 7, 10, 13]. Despite MR protocol optimization to obtain arterial phase images of diagnostic quality, various artifacts and non-diagnostic images are still occasionally encountered in clinical practice. Recently, gadoxetic acid has been shown to provoke subjective acute transient dyspnea significantly more often than other contrast media [8]. This can disturb breath-holding and can induce respiratory motion artifacts during the hepatic arterial phase. To overcome this problem, a reduction in scanning time is of paramount importance. Although parallel imaging techniques are already used to reduce scanning time [2, 14, 15], a further reduction of acquisition time necessitates a high-performance scanner with increased numbers of coil elements [14]. We implemented a new parallel imaging technique, CAIPIRINHA, using the newest generation MR scanner, including a standard 18-channel body matrix coil and table-mounted 32-channel spine matrix coil, which reduced the acquisition time for the hepatic arterial phase by up to 13 s.

The clinical feasibility of CAIPIRINHA has been researched for the hepatobiliary phase of gadoxetic acid-enhanced MRI and liver MRI using non-hepatocyte specific contrast agents [4, 16]. They reported that for single-phase imaging of the liver, CAIPIRINHA reduced the acquisition time to a minimum of 6 s with preserved or improved spatial resolution. In a previous study, CAIPIRINHA was valuable in improving the image quality of the hepatobiliary phase [16]. However, we believe that adopting CAIPIRINHA for the hepatic arterial phase is quite different from its application in the hepatobiliary phase, because the hepatobiliary phase does not require precise timing. As opposed to GRAPPA, CAIPIRINHA uses a separate calibration scan before the acceleration scan (actual imaging), and additional time (approximately 3 s) for calibration is required in addition to the acceleration scan time (actual imaging time, approximately 10 s). For this reason, we commenced the arterial phase

4

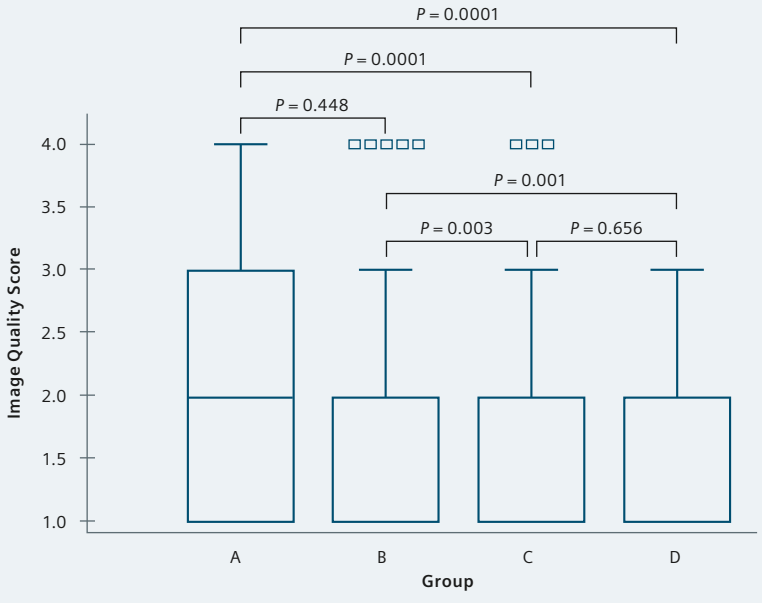

4 Box-and-whiskers plot showing the median image quality score among the 4 groups. The middle line in the box represents the median, and the lower and upper boundaries of the boxes represent the lower and upper quartiles (25th and 75th percentiles, respectively). The whiskers indicate the maximum and minimum scores.

scan immediately after detecting the arrival of the contrast media at the aortic arch, as opposed to GRAPPA, where the scan starts immediately after detecting the arrival of the contrast media in the descending thoracic aorta.

In addition, we found a significant improvement in image quality from group B to C ($P = 0.003$), even though both groups used the same optimized protocol on 3T MRI scanners. It is suspected that the increased number of coil elements in the newer MRI scanner (group C) may have accounted for the higher signal-to-noise ratio and better image quality observed. Moreover, there was no significant difference in image quality between groups A and B or between groups C and D, although a slight improvement in image quality was observed. This could explain why the type of MR scanner is a dependent factor in determining the image quality of the hepatic arterial phase, even among MR scanners of same field strength.

In conclusion, the use of the CAIPIRINHA technique reduced non-diagnostic arterial phase images and improved the image quality of the hepatic arterial phase in gadoxetic acid-enhanced liver MRI. Using CAIPIRINHA technique, the hepatic arterial phase can be clarified in gadoxetic acid-enhanced liver MRI.

References

1 Wile GE, Leyendecker JR. Magnetic resonance imaging of the liver: sequence optimization and artifacts. Magn Reson Imaging Clin N Am 2010;18(3):525-47.
2 Vogt FM, Antoch G, Hunold P, et al. Parallel acquisition techniques for accelerated volumetric interpolated breath-hold examination magnetic resonance imaging of the upper abdomen: assessment of image quality and lesion conspicuity. J Magn Reson Imaging 2005;21(4):376-82.
3 Breuer FA, Blaimer M, Mueller MF, et al. Controlled aliasing in volumetric parallel imaging (2D CAIPIRINHA). Magn Reson Med 2006;55(3):549-56.
4 Riffel P, Attenberger UI, Kannengiesser S, et al. Highly accelerated T1-weighted abdominal imaging using 2-dimensional controlled aliasing in parallel imaging results in higher acceleration: a comparison with generalized autocalibrating partially parallel acquisitions parallel imaging. Invest Radiol 2013;48(7):554-61.
5 Goodwin MD, Dobson JE, Sirlin CB, Lim BG, Stella DL. Diagnostic challenges and pitfalls in MR imaging with hepatocyte-specific contrast agents. Radiographics 2011;31(6):1547-68.
6 Ringe KI, Husarik DB, Sirlin CB, Merkle EM. Gadoxetate disodium-enhanced MRI of the liver: part 1, protocol optimization and lesion appearance in the noncirrhotic liver. AJR Am J Roentgenol 2010;195(1):13-28.
7 Cruite I, Schroeder M, Merkle EM, Sirlin CB. Gadoxetate disodium-enhanced MRI of the liver: part 2, protocol optimization and lesion appearance in the cirrhotic liver. AJR Am J Roentgenol 2010;195(1):29-41.
8 Davenport MS, Viglianti BL, Al-Hawary MM, et al. Comparison of acute transient dyspnea after intravenous administration of gadoxetate disodium and gadobenate dimeglumine: effect on arterial phase image quality. Radiology 2013;266(2):452-61.
9 Motosugi U, Ichikawa T, Sou H, et al. Dilution method of gadolinium ethoxybenzyl diethylenetriaminepentaacetic acid (Gd-EOB-DTPA)-enhanced magnetic resonance imaging (MRI). J Magn Reson Imaging 2009;30(4):849-54.
10 Haradome H, Grazioli L, Tsunoo M, et al. Can MR fluoroscopic triggering technique and slow rate injection provide appropriate arterial phase images with reducing artifacts on gadoxetic acid-DTPA (Gd-EOB-DTPA)-enhanced hepatic MR imaging? J Magn Reson Imaging 2010;32(2):334-40.
11 Park YS, Lee CH, Kim IS, et al. Usefulness of controlled aliasing in parallel imaging results in higher acceleration in gadoxetic Acid-enhanced liver magnetic resonance imaging to clarify the hepatic arterial phase. Invest Radiol. 2014;49(3):183-8.
12 Tanimoto A, Higuchi N, Ueno A. Reduction of ringing artifacts in the arterial phase of gadoxetic acid-enhanced dynamic MR imaging. Magn Reson Med 2012;11(2):91-7.
13 Schmid-Tannwald C, Herrmann K, Oto A, Panteleon A, Reiser M, Zech C. Optimization of the dynamic, Gd-EOB-DTPA-enhanced MRI of the liver: the effect of the injection rate. Acta Radiologica 2012;53(9):961-5.
14 Deshmane A, Gulani V, Griswold MA, Seiberlich N. Parallel MR imaging. J Magn Reson Imaging 2012;36(1):55-72.
15 McKenzie CA, Lim D, Ransil BJ, et al. Shortening MR image acquisition time for volumetric interpolated breath-hold examination with a recently developed parallel imaging reconstruction technique: clinical feasibility. Radiology 2004;230(2):589-94.
16 Yu MH, Lee JM, Yoon JH, Kiefer B, Han JK, Choi BI. Clinical application of controlled aliasing in parallel imaging results in a higher acceleration (CAIPIRINHA)-volumetric interpolated breathhold (VIBE) sequence for gadoxetic acid-enhanced liver MR imaging. J Magn Reson Imaging 2013. 2013;38(5):1020-6.

Contact

Chang Hee Lee, M.D., Ph.D.
Department of Radiology
Korea University Guro Hospital
Korea University College of Medicine
80 Guro-dong, Guro-gu,
Seoul 152-703, Korea
Phone: +82-2-2626-1338
Fax: +82-2-863-9282
chlee86@korea.ac.kr

Case Study: CAIPIRINHA-Dixon-TWIST-VIBE Imaging of Liver Metastasis

Wang Xuan[1]; Xue Huadan[1]; Liu Hui[2]; An Jing[3]; Dominik Nickel[4]; Kiefer Berthold[4]; Jin Zhengyu[1]

[1]Department of Radiology, Peking Union Medical College Hospital, Beijing, China
[2]MR Collaboration, Healthcare, Siemens Ltd., China, Shanghai, China
[3]MR Application, Siemens Shenzhen Magnetic Resonance Ltd., Shenzhen, China
[4]MR Development, Healthcare, Siemens AG, Erlangen, Germany

Introduction

Magnetic Resonance Imaging (MRI) plays an important role in the detection and characterization of focal and diffuse liver diseases. There is now a large amount of literature describing the value of dynamic contrast-enhanced (DCE) T1-weighted (T1w) imaging using extracellular and liver-specific contrast agents. The patterns of contrast enhancement, in combination with other contrast mechanisms (diffusion-weighted imaging, in/opposed phase, T2-weighted imaging, etc.), provide well-described criteria for detection and characterization of hepatic lesions.

However, conventional liver DCE-T1w imaging requires one breath-hold (~15–20 s) for one phase, and in this case, the lesion enhancement pattern may be weakened or missed due to improper timing or the fast uptake and washout of the contrast agent in certain types of lesions. In order to solve this problem, Siemens recently developed a CAIPIRINHA-Dixon-TWIST-VIBE (CDT-VIBE) sequence* allowing 3D T1w imaging with high temporal resolution and with preserved high spatial resolution. The primary study showed that CDT-VIBE has 21% diagnostic improvement for smaller lesion detection [1].

In our hospital, we are interested in using CDT-VIBE in combination with a liver specific contrast agent (Primovist, Bayer Healthcare, Berlin, Germany) to evaluate the enhancement pattern of arterial phase, portal venous phase, and hepatobiliary phase, and the dynamic signal-time curves of liver metastasis from pancreatic neuroendocrine cancer.

Protocol

CDT-VIBE allows us to acquire 5 phases of arterial and portal venous phases in 20 s breath-hold each. The delayed phases and hepatobiliary phase are acquired with only 1 phase for each

1

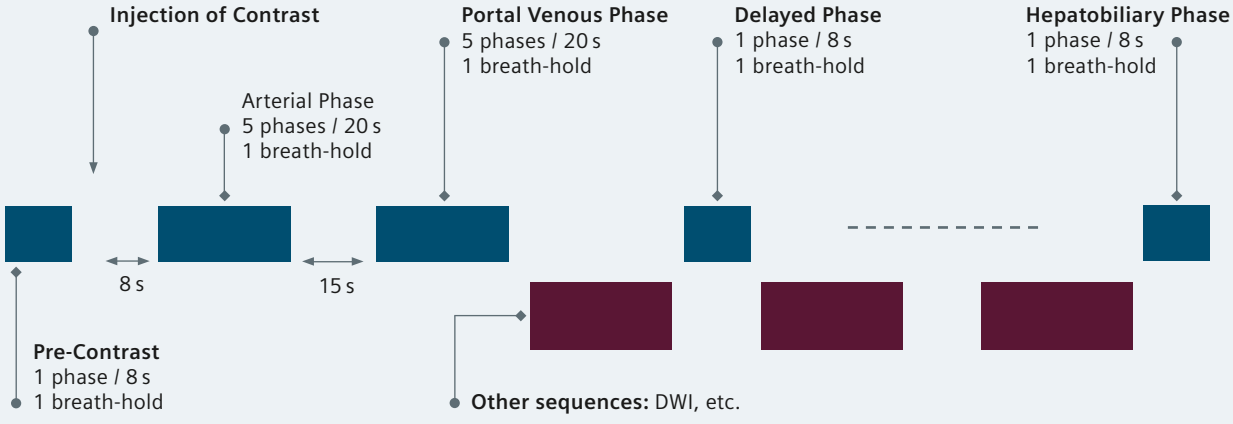

1 Breath-hold CDT-VIBE protocol after injection of Primovist contrast agent is configured for vascularity characterization (multiple arterial and portal venous phases) and lesion/parenchyma contrast enhancement (delayed and hepatobiliary phases). This CDT-VIBE examination is performed with a spatial resolution of 1.3 ×1.3 × 3 mm on a 3T MAGNETOM Skyra system. Other scans during the examination include transverse DWI, transverse in-phase and out-of-phase T1w VIBE, breath-hold and PACE triggered T2w TSE, coronal T2w HASTE and post-contrast coronal T1w VIBE.

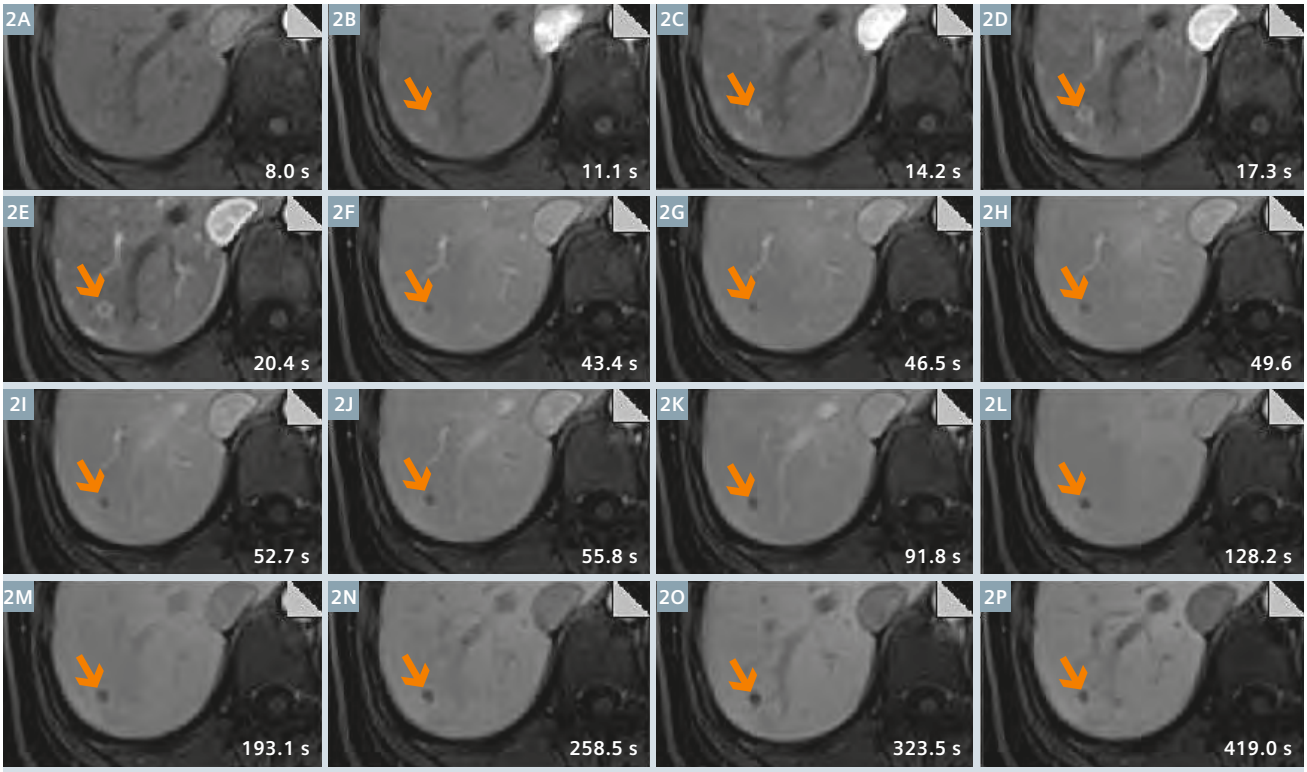

2 Contrast-enhanced T1w dynamic series of liver using CDT-VIBE. The lesion is indicated by the arrow.

breath-hold with the same parameters as arterial and portal venous phases. The acquisition of the arterial phase begins at 8 s after the start of contrast injection. Protocol details are given in Figure 1.

Imaging findings

It is widely known that hepatobiliary phase imaging enables an increase in sensitivity in the detection of metastasis by exploring the liver-lesion-contrast generated by the uptake of liver-specific contrast agents by the liver parenchyma. However, the specificity of metastasis characterization using the hepatobiliary phase only remains a challenge. Specifically, the ability to differentiate metastasis from malignant lesions (such as HCC, which also gives hypo intensity in the hepatobiliary phase) and benign lesions (such as cysts and hemangiomas, which appear hypointense in the hepatobiliary phase) is still a problem, not to mention the grading of metastasis.

There is a section of literature that combines the features from arterial enhancement and lesion/parenchyma contrast enhancement in the hepatobiliary phase to differentiate metastases from other lesions by using conventional single phase acquisition per breath-hold sequence. The metastasis shows ring-like enhancement in the arterial phase, and appears hypointense in the hepatobiliary phase. Multiple arterial and portal venous phase imaging enables new opportunities to explore the vascular enhancement features. CDT-VIBE provides the capability of multiple arterial and portal venous phase imaging.

Figure 2 shows a contrast-enhanced T1w dynamic series of metastasis from pancreatic neuroendocrine cancer using the above mentioned CDT-VIBE protocol. In the later arterial phase, the lesion appears as a ring-like enhanced pattern, and in the later hepatobiliary phase, the lesion shows hypointensity compared to the parenchyma. These observations are consistent with previous reports in the literature on the enhancement pattern for metastasis [2]. We also observed that in the early arterial phase (11.1 s), the ring-enhanced pattern is not as apparent as in the later arterial phase (20.4 s). As evidenced in Figure 3, the estimated biggest contrast difference between lesion core and lesion ring is identified at the peak of the arterial phase. In this case, if the conventional single breath-hold protocol is used, the ring-enhanced pattern might be missed, while the multiple arterial phases offer a larger observation window.

In addition, as shown in Figure 4, the subtracted arterial phase images (5^{th} phase – 1^{st} phase) show the visualization of the feeding vessels to the lesion. In this way, it shows the potential to guide surgery to identify arterial and portal venous features, especially the feeding vessel in making a therapy plan.

3

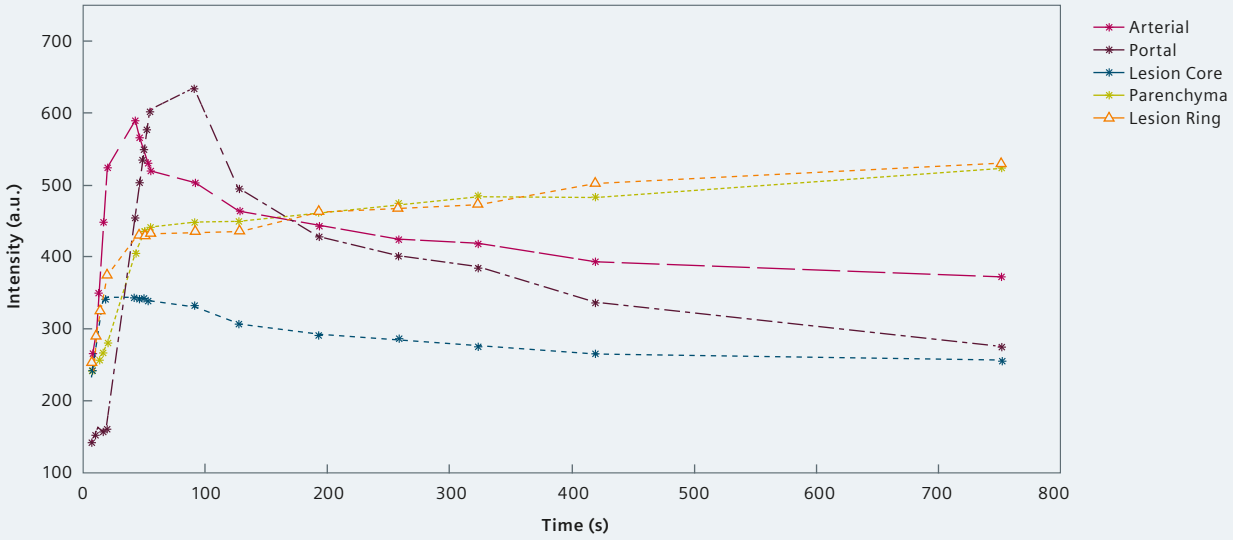

3 Dynamic signal-time curve of arterial phase, portal venous phase, core of lesion (defined hypointensive region in the hepotabiliary phase), ring around lesion core, and parenchyma. The vertical dash line indicates the estimated peak of the arterial phase.

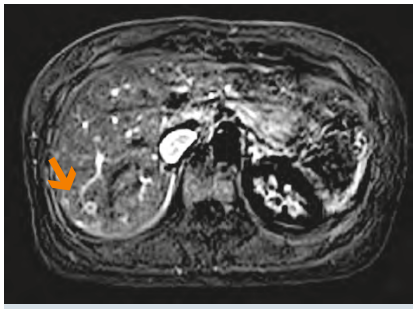

4 Feeding vessel of the lesion is visualized in the 3D subtracted arterial phase images.

Conclusion

CDT-VIBE offers better illustration of arterial and portal venous features of lesions due to the multiple arterial and portal venous phases imaging capability. By combining these findings with features of hepatobiliary phases, the metastasis can be well described. For the feature of metastasis, CDT-VIBE not only provides the ring-like enhancement pattern, but also clearly shows the feeding vessel of the lesion. Furthermore, by applying a dual input pharmacokinetic modeling for the liver, a quantitative analysis of lesions will be possible using CDT-VIBE.

References

1 Michaely HJ, Morelli JN, Budjan J, Riffel P, Nickel D, Kroeker R, Schoenberg SO, Attenberger UI, CAIPIRINHA-Dixon-TWIST (CDT)-volume-interpolated breath-hold examination (VIBE): a new technique for fast time-resolved dynamic 3-dimensional imaging of the abdomen with high spatial resolution. Invest Radiol. 48(8):590-7, 2013 Aug.

2 Van Beers BE, Pastor CM, Hussain HK., Primovist, Eovist: what to expect? J Hepatol. 57(2):421-9, 2012 Aug.

Xuan Wang, M.D.

Huadan (Danna) Xue, M.D.

Contact

Xuan Wang, M.D.
Dept. of Radiology
Peking Union Medical College Hospital
Beijing, China, 100730
Phone: +86-13661147518
wxpumc@163.com

Huadan (Danna) Xue, M.D.
Associate Professor
Dept. of Radiology
Peking Union Medical College Hospital
Beijing, China, 100730
Phone: +86-13146115223
xuehd@pumch.cn

Case Report: Assessment of Renal Allograft Function with DTI and Tractography

Wenjun Fan[1, 2]; Wen Shen[1]

[1]Department of Radiology, Tianjin First Center Hospital, Tianjin, China
[2]Armed Police Corps Hospital of Henan, Zhengzhou, Henan, China

Introduction

Kidney transplantation is the therapy of choice for patients with end-stage chronic kidney disease. In our hospital, there are about 150 cases of renal transplantation each year. Intense monitoring of renal allograft after surgery is crucial to identify renal allograft's dysfunction at an early stage and thus to carry out appropriate treatment to prevent serious adverse effects.

Functional imaging with magnetic resonance imaging (MRI) is a fast-growing field in clinical application, which aims at characterizing function parameters and changes. Diffusion tensor imaging (DTI) provides diffusion measurements in at least six directions. Information obtained from DTI contains not only the amount of diffusion but also the anisotropy of diffusion, which is quantified by the fractional anisotropy (FA), ranging from 0 (no preferred diffusion direction, isotropic diffusion) to 1 (only one diffusion direction, completely anisotropic diffusion). In recent years, DTI has been used in assessing renal damage of chronic parenchymal diseases and diabetic nephropathy [1-3]. Here we used DTI and tractography in assessing the function of renal allograft at an early stage after transplantation.

Patient history

Three kidney-transplanted recipients and a healthy volunteer were examined to investigate the feasibility of DTI in assessing the function of allograft during the early post-transplantation period. Serum creatinine concentrations were obtained on the same day as the MRI examination and used to calculate estimated glomerular filtration rate (eGFR) by utilizing the modification of diet in renal disease formula.

Subject 1 (25-year-old, female) is a healthy volunteer without any history of renal disease, hypertension, diabetes or other vascular diseases.

Subject 2 (31-year-old, male, 14 days after kidney transplantation, eGFR = 93.5 ml/min / 1.73 m^2) is a recipient with good function (eGFR ≥ 60 ml/min / 1.73 m^2).

Subject 3 (24-year-old, female, 20 days after kidney transplantation, eGFR = 53.6 ml/min / 1.73 m^2) is a recipient with moderately impaired allograft function (30 ≤ eGFR < 60 ml/min / 1.73 m^2).

Subject 4 (28-year-old, female, 17 days after kidney transplantation, eGFR = 7.23 ml/min / 1.73 m^2) is a recipient with severely impaired allograft function (eGFR < 30 ml/min / 1.73 m^2).

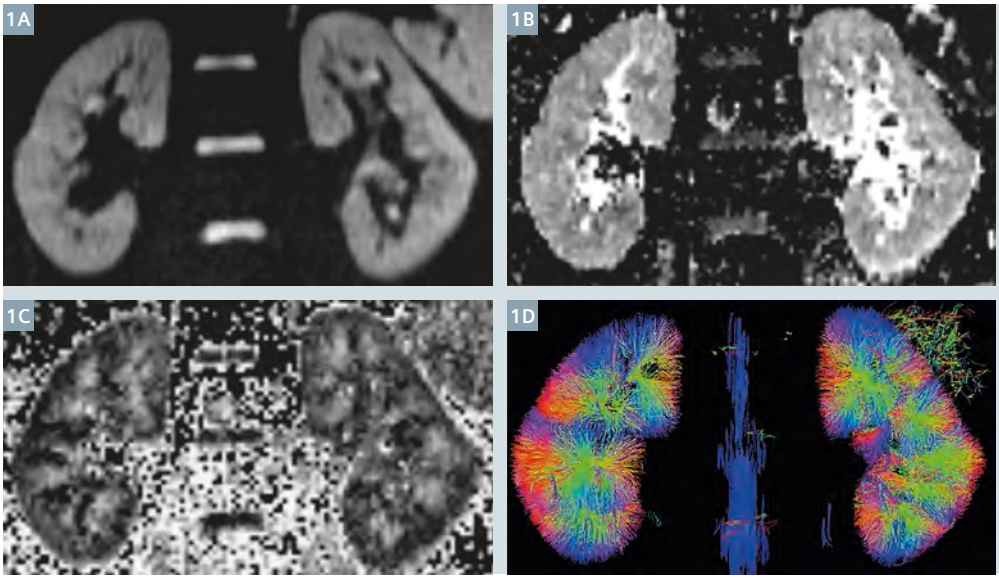

1 Healthy volunteer (25-year-old female) without any history of renal disease, hypertension, diabetes or other vascular diseases.

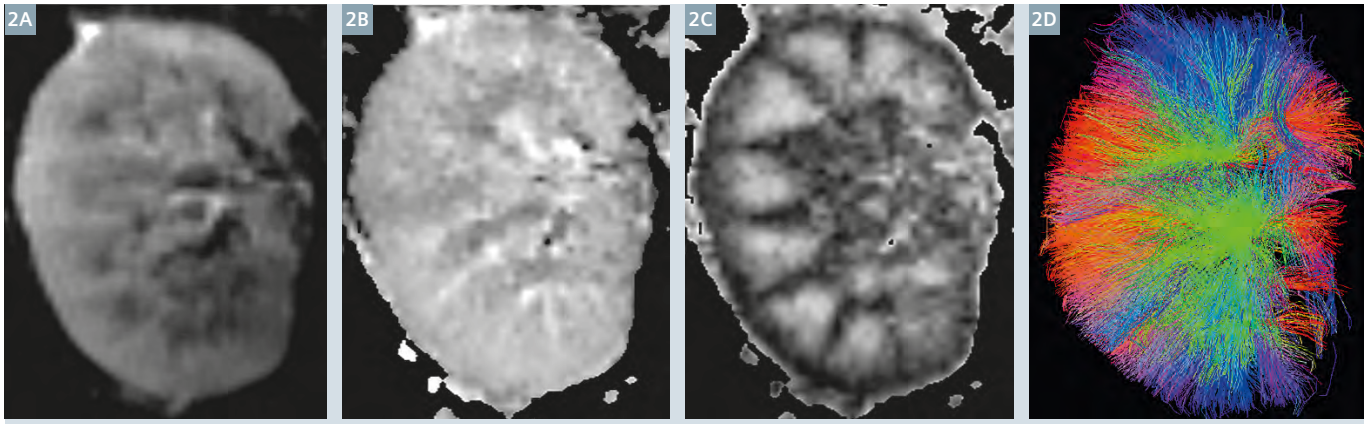

b0-map | ADC-map | FA-map | Tractography

2 Recipient with good allograft function, 31-year-old male, 14 days after kidney transplantation, eGFR = 93.5 ml/min / 1.73 m².

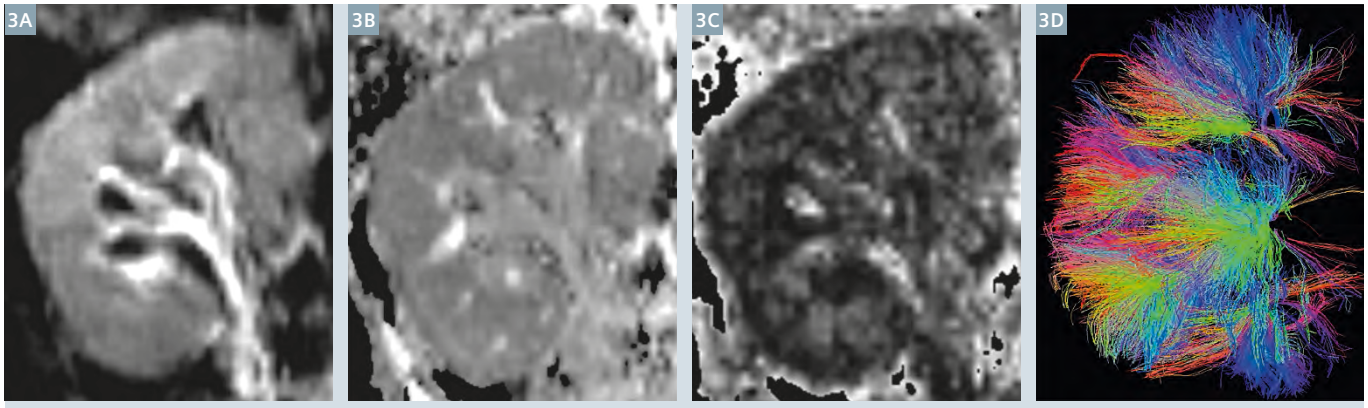

b0-map | ADC-map | FA-map | Tractography

3 Recipient with moderately impaired allograft function, 24-year-old female, 20 days after kidney transplantation, eGFR = 53.6 ml/min / 1.73 m².

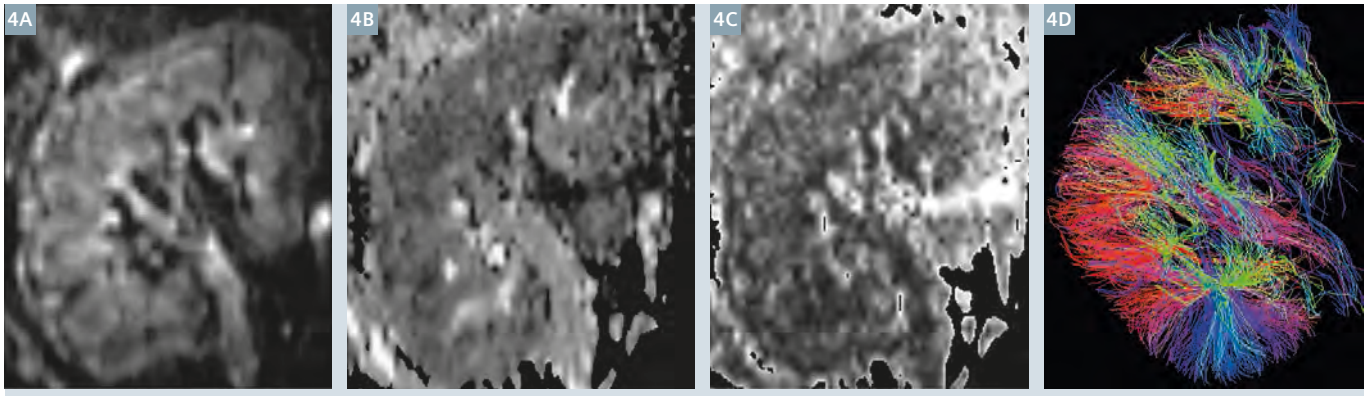

b0-map | ADC-map | FA-map | Tractography

4 Recipient with severely impaired allograft function, 28-year-old female, 17 days after kidney transplantation, eGFR = 7.23 ml/min / 1.73 m².

Sequence details

MR imaging of the kidney was performed at 3T (MAGNETOM Trio a Tim System, Siemens Healthcare, Erlangen, Germany) with a 32-element surface coil and with the spine coil integrated into the table.

In all subjects, axial breath-hold turbo spin-echo T1-weighted images and coronal fat-saturated single-shot spin-echo T2-weighted images were obtained for morphological analysis. DTI images were acquired with a fat-saturated oblique-coronal multi-section echo-planar imaging sequence with the following parameters: 6 diffusion directions, b-values 0 and 300 s/mm^2, TR 1800 ms, TE 103 ms, 9 averages, 30 slices at a slice thickness of 1.8 mm with no intersection gap, FOV 230 × 230 mm^2, matrix 128 × 128, voxel size 1.8 × 1.8 × 1.8 mm^3, parallel imaging acceleration factor 2. To weaken the impact of respiratory motion, respiratory-triggered technique was conducted in the healthy volunteer. For the renal allograft recipients, the respiratory-triggered technique was not applied because respiratory motion was negligible in the transplanted kidney owing to their location in the iliac fossa.

The Neuro 3D software (MAGNETOM Trio a Tim System, Siemens Healthcare, Erlangen, Germany) was used for DTI data analysis.

A 3D whole-kidney tractography was created by using Diffusion Toolkit software package (http://trackvis.org/) with an FA threshold of 0.1 and angle threshold of 60°.

Imaging findings

For the healthy volunteer, FA-map demonstrates perfect cortical-medullary discrimination with much higher signal of the medulla, while the signal of the cortex is much higher in ADC-map. Tractography illustrates numerous tracts with a distinct radial arrangement and closely convergence into pyramids, matching the anatomical arrangement of the renal parenchyma (Fig. 1).

For the allograft with good function, manifestations of FA-map and tractography are nearly identical to the healthy kidney. ADC-map shows unclear cortical-medullary differentiation with slightly higher signals of both the cortex and the medulla compared to the healthy kidney (Fig. 2).

For the allograft with moderately impaired function, signals of ADC-map and FA-map apparently decrease with poorly cortical-medullary discrimination. Meanwhile, the number and density of radial tracts also decrease with partly loose arrangement in tractography (Fig. 3).

For the allograft with severely impaired function, ADC-map and FA-map both show significantly lower signals with much worse cortical-medullary discrimination compared to the healthy kidney and allograft with good function. In tractography, the radial tracts arrange more loosely with many hallow spaces compared to the other three cases, especially in the upper pole (Fig. 4).

Conclusion

As these cases demonstrate, DTI and tractography is a promising way to quantitatively and visually assess renal allograft function after kidney transplantation.

References

1 Levey AS, Bosch JP, Lewis JB, Greene T, Rogers N, Roth D: A more accurate method to estimate glomerular filtration rate from serum creatinine: a new prediction equation. Modification of Diet in Renal Disease Study Group. Ann Intern Med 1999, 130(6):461-470.

2 Jaimes C, Darge K, Khrichenko D, Carson RH, Berman JI: Diffusion tensor imaging and tractography of the kidney in children: feasibility and preliminary experience. Pediatr Radiol 2013.

3 Lanzman RS, Ljimani A, Pentang G, Zgoura P, Zenginli H, Kropil P, Heusch P, Schek J, Miese FR, Blondin D et al: Kidney transplant: functional assessment with diffusion-tensor MR imaging at 3T. Radiology 2013, 266(1):218-225.

Contact

Shen Wen, M.D.
Chief Radiologist
Dept. of Radiology
Tianjin First Center Hospital
24 Fukang road, Nankai district,
Tianjin, China, 300192
Phone: +86-11-22-23626583
shenwen66happy@163.com

MAGNETOM Trio Upgrade to Prisma^{fit} Better Imaging Technique Combined with Higher Throughput in Clinical Practice

Stephan Zangos; Thomas J. Vogl

Institute for Diagnostic and Interventional Radiology, University Hospital Frankfurt, Frankfurt/Main, Germany

The decision to purchase a new MRI system is based on several factors. The cost of the purchase and installation are a particularly important factor in such a decision. However, a new MRI system with innovative technology offers unique features and the opportunity to develop into new markets. The use of new technology can lead to improved patient comfort, better image quality and an increase in the number of examinations.

The installation of a new MRI system in an ongoing clinical routine always poses a logistical challenge. In a worst-case scenario this may involve the decommissioning of neighboring devices. However, replacing the devices after several years cannot be avoided for ever.

The MAGNETOM Trio a Tim System was used in the clinical routine in our institution for 6 years to obtain images across the entire diagnostic spectrum, including angiograms, as well as musculoskeletal, thoracic and abdominal imaging.

In order to regain access to the latest MR technology in our clinic and to pursue new research areas, the possibility of a new acquisition was evaluated.

Due to the physical layout of our Institute, our working area would have

1

1 This plan shows the problem of access via the pathway to our department. This would require shutting down the 1.5T MAGNETOM Espree and 3T MAGNETOM Trio and installing dust protection walls (blue) to be used in the work area.

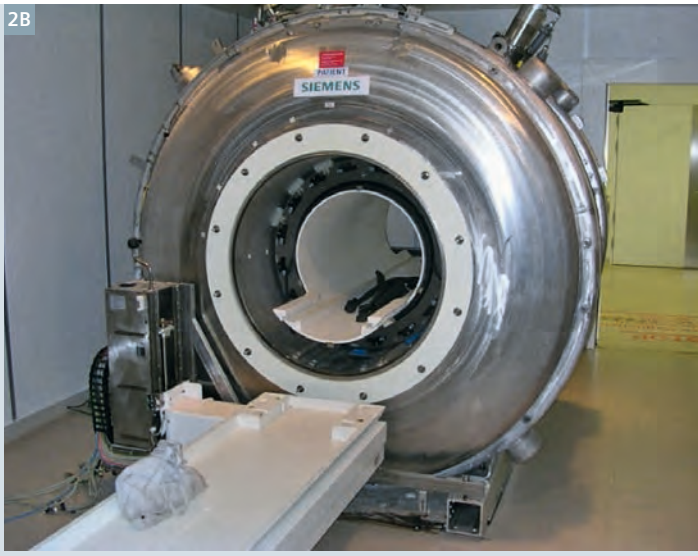

2 These images show the building steps during the fit-upgrade of the MAGNEOM Trio a Tim System **(2A)**. After removing all the old system components **(2B)** the installation of the new Prisma^{fit} components was carried out by introducing the new gradients **(2C)** the new Tim covers **(2D)** and examination table **(2E)**.

had to be used for the installation of this new device. This would have led to additional decommissioning of the neighboring 1.5T MAGNETOM Espree for at least 10 days (Fig. 1).

In addition to the initial cost of the new unit, considerable additional costs for the use of a crane, the cabin construction, the clearance of the transport paths and the restoration of the premises would have been incurred (Table 1). Examining alternatives, an upgrade to the Trio a Tim System was offered by a Prisma^{fit}. The upgrade included the latest MRI technology including an XR 80/200 gradient system, Tim 4G architecture and Dot (Day optimizing throughput) workflow engines. The new Tim table can combine up to 204 coil elements.

After analysis of the additional costs, an upgrade seemed to be the only economically meaningful option. After successfully upgrading our 1.5T MAGNETOM Avanto to Avanto^{fit} in the spring, the decision was easily made for a MAGNETOM Prisma^{fit} upgrade.

During the upgrade of the scanner, the original 3 Tesla magnet was left in the magnet room (Fig. 2). All covers, the body coil, and the gradients were replaced with new ones. All analog cables were eliminated and the new all digital-in/ digital-out DirectRF design was installed directly at the scanner. In the technical room, all cabinets were removed and a new cooling control unit and gradient power amplifier were installed. Additionally, all workstations, monitors, and keyboards were removed and replaced with new ones. Finally, all installed licenses were migrated into the new software version *syngo* MR D13.

After installation and quality tests, the upgrade to the MAGNETOM Prisma^{fit} was completed in only 15 working days. A great advantage of this upgrade during the installation was that there were no restrictions to the operational capability of the surrounding MRI in the working area. For this reason, the upgrade could be made without limitations to patient care and the workflow. After a short training phase, the system was smoothly integrated into the clinical routine. Since the focus of our department is on abdominal and hepatobiliary imaging, the use of the Abdomen Dot Engine in particular has led to an improvement of the workflow.

The resulting reproducibility of the investigations has led to a better comparability of the images during follow-up. In particular, the timing of the arterial phase is made much more efficient by using Dot. In general, the new technology has led to improvement in image quality. In liver imaging, the use of CAIPIRINHA Dixon VIBE technology has led to a significant improvement in image quality compared to the standard VIBE sequence.

For the technical staff, the Dot software provides a significant reduction in study planning and implementation through the automatic positioning of the examination area, as well as automatic breathing commands. In addition, the Dot engines are routinely used for neurological, cardiac, and spinal diagnostics. Whenever the workflow allows, we try to investigate the joints in the new 3 Tesla system due to the significantly better image quality compared to the other MRI systems in the department.

Over the last half year, the Prisma^{fit} could be used after the upgrade without any problems in routine clinical practice and research, and more than 1,700 patients have been examined to date. In particular, there has been improvement of image quality resulting in clinical partners stimulating demand for Prisma^{fit} examinations.

Table 1

Costs	Upgrade (fit)	Ex-Factory
Invest costs	<<<	>>>
Local costs		
Architectural		
Structural	not necessary	new infrastructure
Power	not necessary	new infrastructure
Cooling	not necessary	new infrastructure
RF-Cabin	not necessary	high cost (customer choice)
Other		
Crane	not necessary	depends on site, high cost
Local permits	not necessary	see above
System downtime	15 working days	n.a.
Taxes	Local (Germany: 19%)	Local (Germany: 19%)
Applications Training Standard 1–2 (weeks)	equal for either option	
Service	equal for either option	

Table 1 shows a comparison of the construction costs between an upgrade and a new installation.

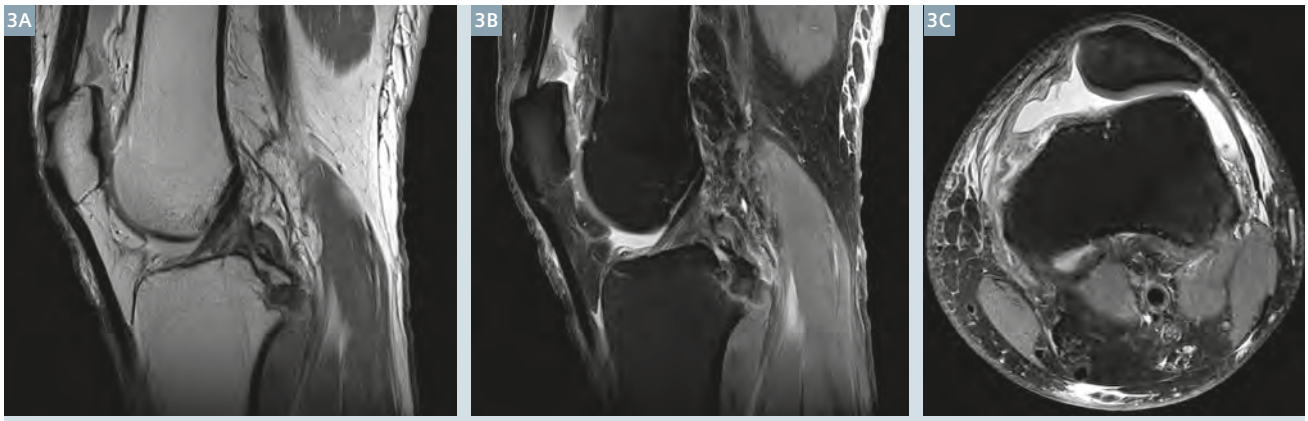

3 Figure 3 shows a patient with bony avulsion of the posterior cruciate ligament: T1-weighted **(3A)** and T2w PD FS sequences **(3B, C)** in sagittal and transverse orientation. For imaging, a 15-channel knee coil was used.

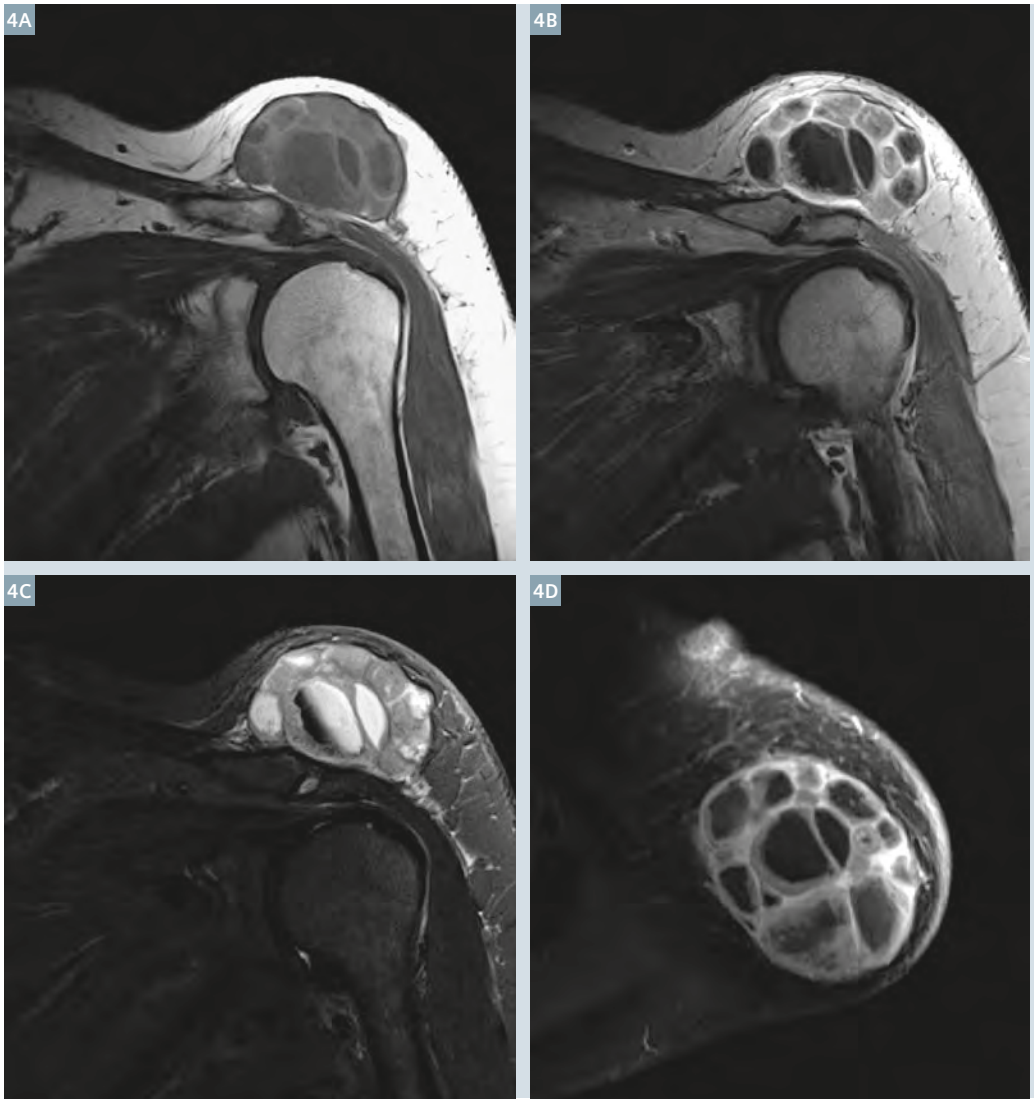

4 Metastasis of a malignant melanoma investigated in a shoulder coil. Native and contrast-enhanced T1w sequences **(4A, B)** and T2w PD FS **(4C)** in paracoronal orientation. Contrast-enhanced T1w FS sequence in transverse orientation **(4D)**.

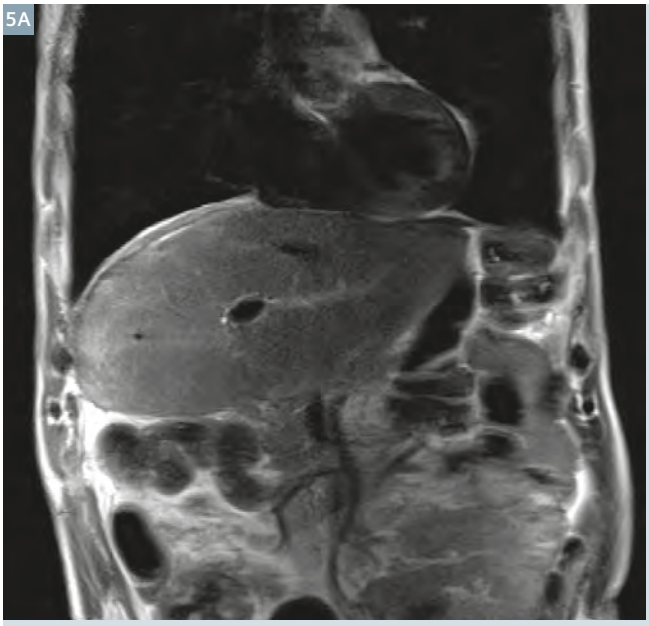
5A

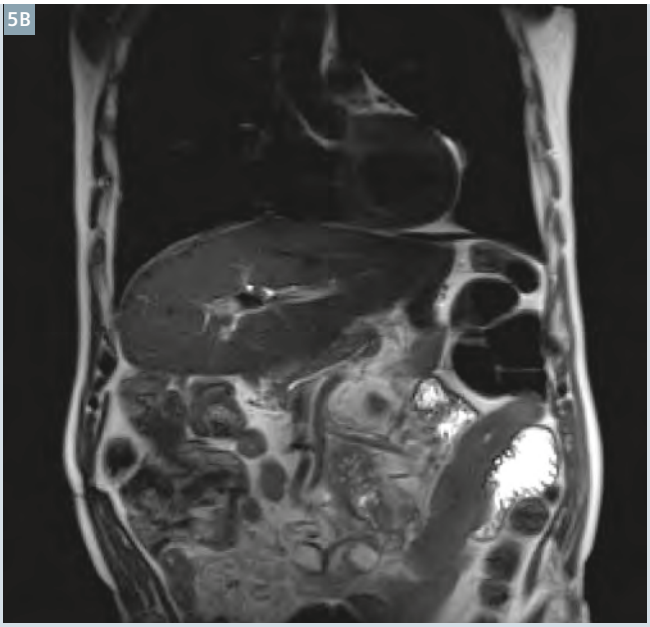
5B

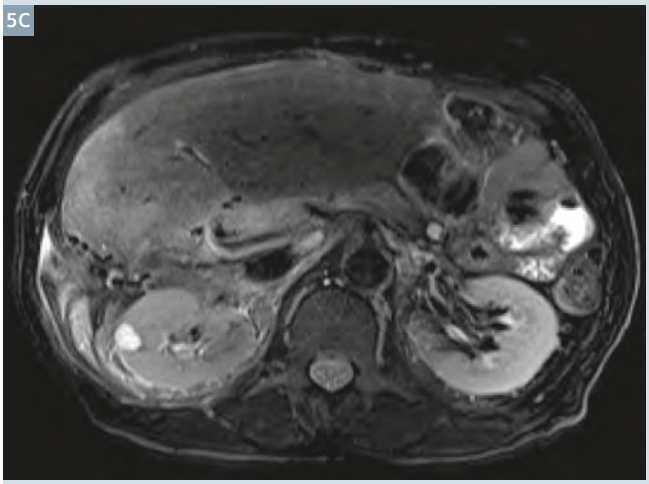
5C

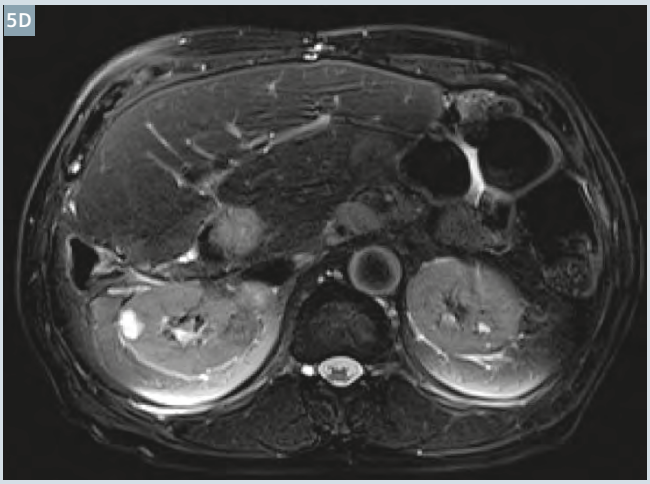
5D

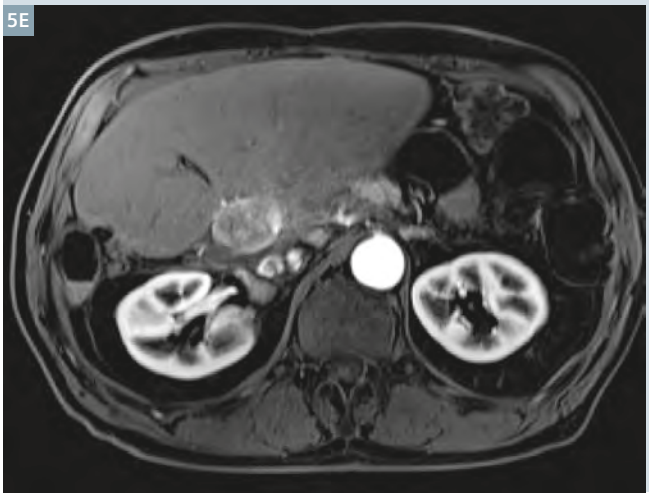
5E

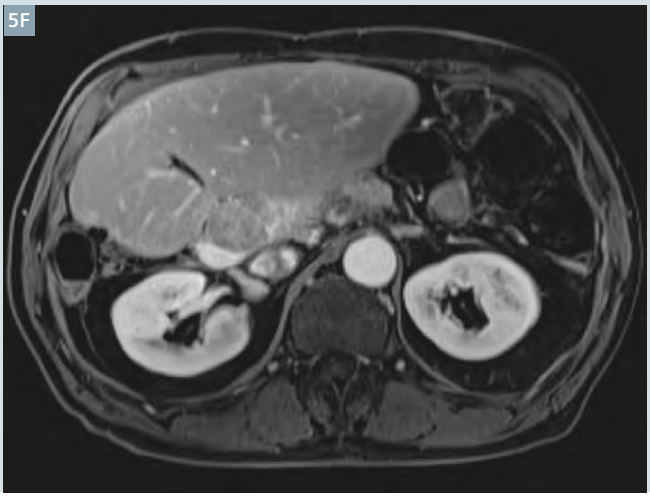
5F

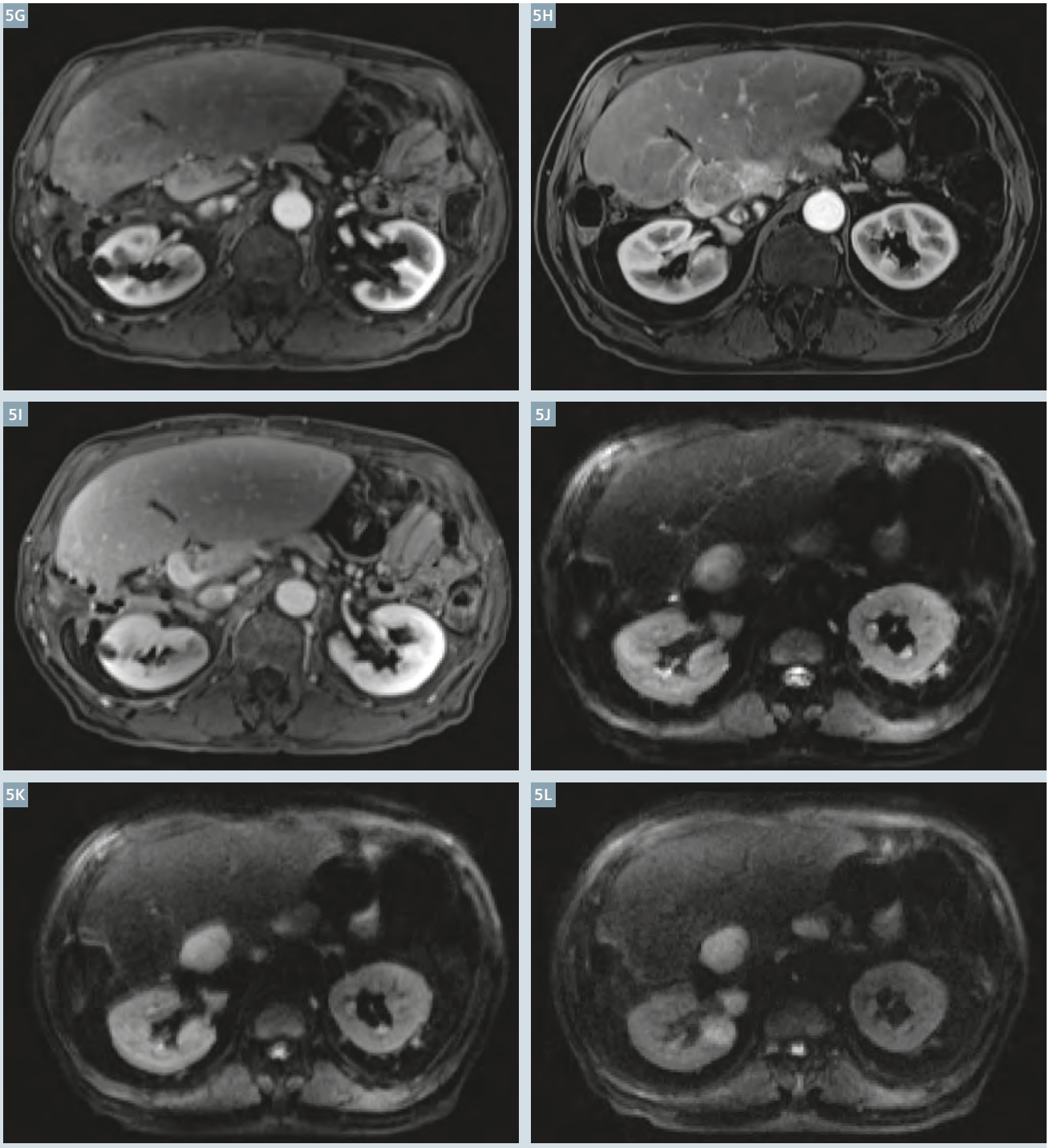

5 Staging in a patient with a neuroendocrine tumor of the pancreas. In the follow-up, one examination was performed with the MAGNETOM Trio a Tim System and one with the Prisma^{fit}. In direct comparison, an improvement in image quality could be observed in all sequences after the upgrade: Coronal HASTE sequence (Trio vs. Prisma^{fit}) **(5A, B)** / T2-weighted TSE FS (Trio vs. Prisma^{fit}) **(5C, D)** / T1-weighted VIBE FS (Trio) **(5E, F)** vs. CAIPIRINHA Dixon VIBE (Prisma^{fit} early and late arterial, venous phase) **(5G–L)**. But even in the diffusion-weighted scans (b 50/400/800) the anatomical structures and pathologies can be better distinguished after the upgrade.

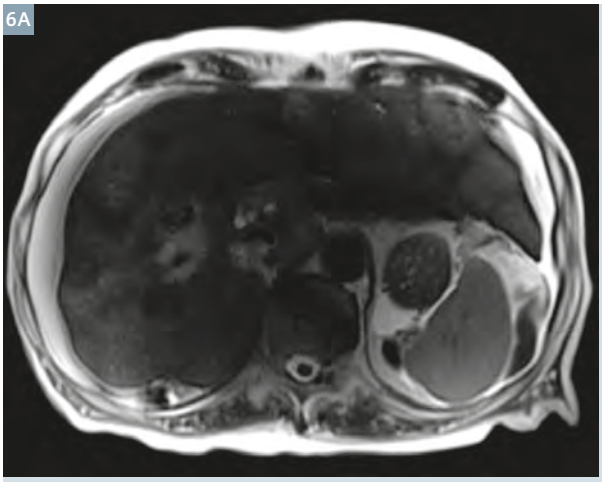

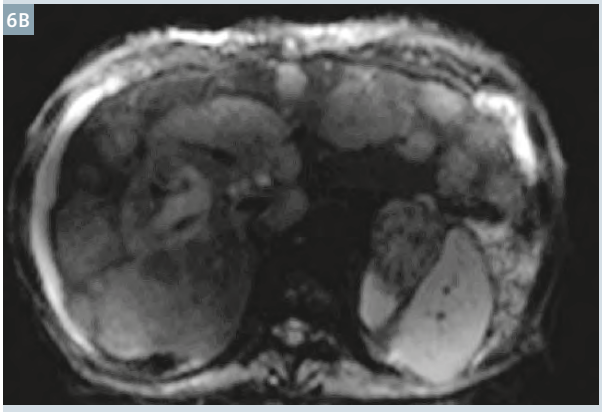

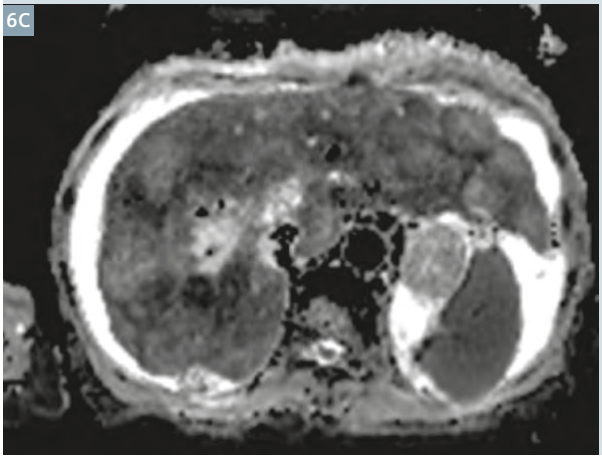

6

Even in patients with ascites, examinations on a 3 Tesla system are possible due to the new technology by the Prisma^{fit} upgrade.
(6A) HASTE sequence

(6B) diffusion-weighted imaging

(6C) ADC map

In our department, work is ongoing to optimize MRI scanning techniques in various parts of the body and for various diseases.

Summary

We have implemented the first upgrade of a MAGNETOM Trio a Tim System to a MAGNETOM Prisma^{fit} without any problems either during or after the upgrade. This upgrade has allowed us to access the latest technology on a 3T system for research and in daily routine, which has led to a significant improvement in image quality as well as the facilitation of the workflow through the use of Dot technology.

Prisma^{fit} is not commercially available in all countries. Due to regulatory reasons its future availability cannot be guaranteed.

Contact

Prof. Dr. med. Stephan Zangos
Institute for Diagnostic and Interventional Radiology
University Hospital Frankfurt
Theodor-Stern-Kai 7
Haus 23c
60590 Frankfurt am Main
Germany
Phone: + 49 (0)69 6301-87287
Fax: +49 (0)69 6301-7288
zangos@em.uni-frankfurt.de

Stephan Zangos

Thomas J. Vogl

Amide Proton Transfer MRI in Patients with High-Grade and Low-Grade Gliomas

Yan Bai[1]; Panli Zuo[2]; Benjamin Schmitt[3]; Dapeng Shi[1]; Jinyuan Zhou[4]; Meiyun Wang[1]

[1]Department of Radiology, Henan Provincial People's Hospital, Zhengzhou, Henan, China
[2]Siemens Healthcare, MR Collaborations NE Asia
[3]Siemens Healthcare, Erlangen, Germany
[4]Department of Radiology, Johns Hopkins University, Baltimore, MD, USA

Introduction

The grading of gliomas has clinical significance in determining a treatment strategy and evaluating prognosis. Despite the accumulated knowledge in clinical practice, differentiating high-grade and low-grade gliomas has persistently posed a dilemma for radiologists in many cases, because of the overlapping imaging findings on conventional MR imaging. One of the differences between solid tumors and normal tissue is the acidic micro-environment around the tumor caused by hydrolysis of Amide Proton Transfer (APT) and an upregulated anaerobic metabolism. As a consequence of the increased intracellular generation of acidic values, the transport of acidic compounds to the extracellular space is upregulated correspondingly to prevent the cellular metabolism from breaking down, which, in turn, can result in slightly increased intracellular pH values [1]. APT is a new MRI technique which detects endogenous mobile proteins and peptides in biotissues, such as tumors [2]. Previous studies have showed that APT MRI is sensitive to changes in cellular pH and protein concentration [3]. Here we used APT MRI, which does not require exogenous contrast agents, as a tool to distinguish high-grade and low-grade gliomas.

Theory

Chemical exchange-dependent saturation transfer (CEST) imaging, which was introduced by Balaban in the early 1990s, is a type of magnetization transfer (MT) imaging to measure exchangeable protons in proteins. As shown in figure 1, the low-concentration proteins are labeled by saturating their exchangeable protons (e.g., hydroxyl, amine, and amide) via selective radio-frequency (RF) irradiation at their specific resonance frequency, and then the labeled protons are transferred to the bulk water via chemical exchange at an exchange rate. The

1

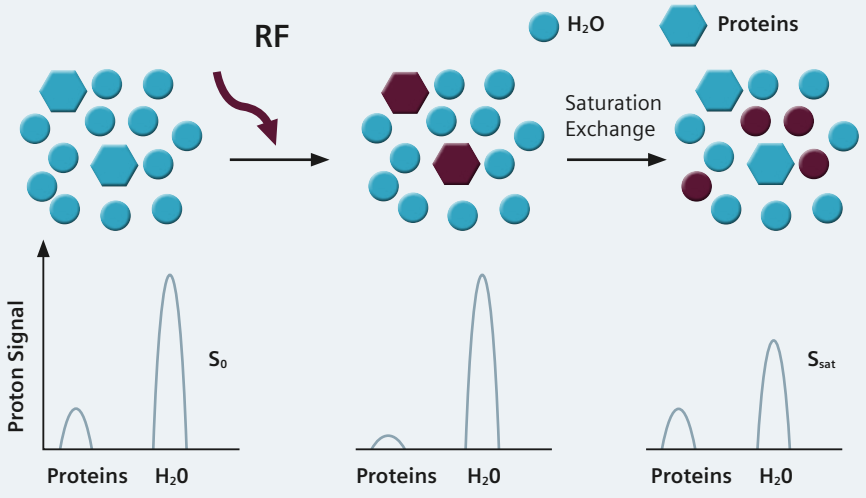

1 A schematic of chemical exchange saturation transfer (CEST). Water and proteins are two pools of protons and have distinct chemical shifts. Protons of proteins are saturated at their specific resonance frequency via RF irradiation. This saturation is transferred to water and decreases the water signal.

solute protons are always at a very low concentration and hard to detect directly using standard MR protocols. However, after a certain time of continuous transfer, this effect decreases the MRI signal and the protons are detected indirectly through the attenuation of the water signal. This effect is measured by using the ratio of water signals with (S_{sat}) and without saturation (S_0).

For the CEST analysis, the most common metric used is the magnetization transfer asymmetry (MTR_{asym}) analysis by subtracting the right and left MT ratio ($MTR=1-S_{sat}/S_0$) to reduce the interference of the coexisting conventional MR and direct saturation effects:

$$MTR_{asym} = S_{sat}(-\Delta\omega)/S_0 - S_{sat}(+\Delta\omega)/S_0 \quad (1)$$

in which $\Delta\omega$ is the frequency difference with water. Plotting MTR with the saturation frequency gives a Z-spectrum (also called CEST spectrum). The amide protons resonate at 8.3 ppm of the proton MR spectrum (3.5 ppm to water signal) and are used for amide proton transfer (APT) imaging.

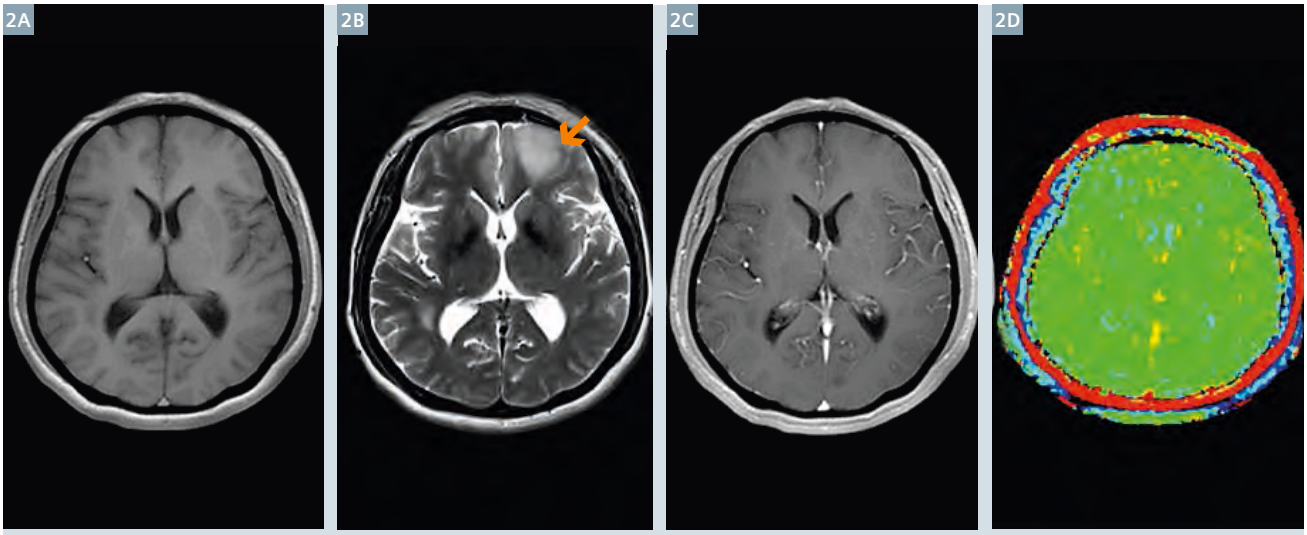

2 51-year-old female patient with astrocytomas (WHO grade II) in the left frontal lobe. **(2A)** T1-weighted image; **(2B)** T2-weighted image; **(2C)** Post-gadolinium T1-weighted image; **(2D)** APT map.

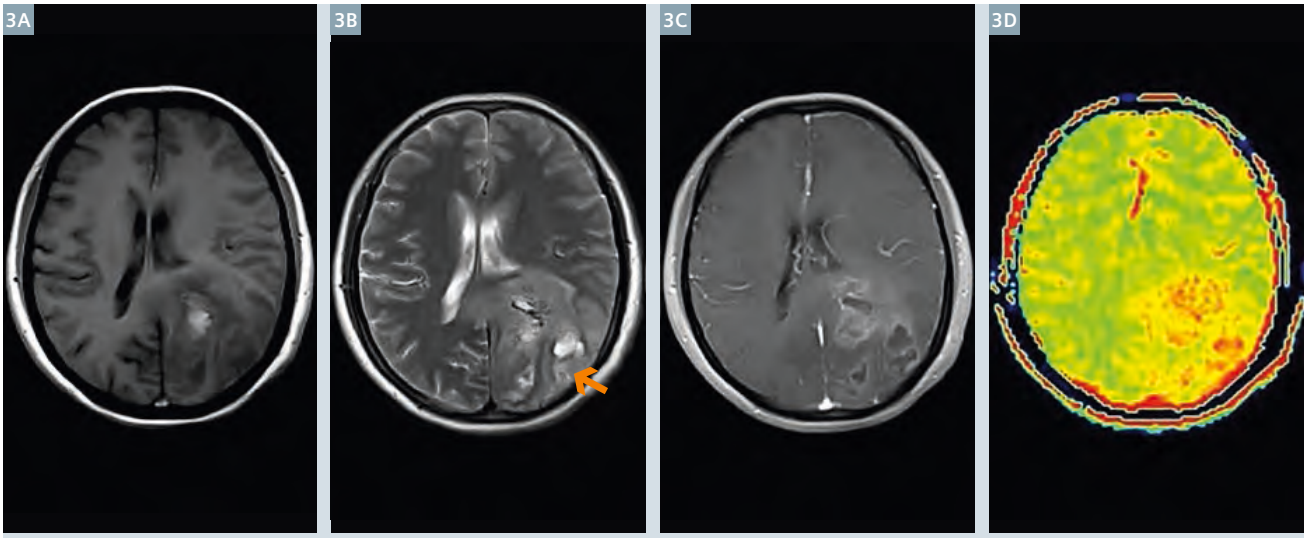

3 47-year-old male patient with glioblastoma (WHO grade IV) in the left occipital lobe. **(3A)** T1-weighted image; **(3B)** T2-weighted image; **(3C)** Post-gadolinium T1-weighted image; **(3D)** APT map.

Patient history

Case 1 is a 51-year-old female patient with astrocytomas (WHO grade II) in the left frontal lobe (Fig. 2). She had neurologic complaints including dizziness, nausea and vomiting for 5 hours before the MRI examination.

Case 2 is a 47-year-old male patient with glioblastoma (WHO grade IV) in the left occipital lobe (Fig. 3). He had a two months history of insomnia and a five hours history of complaints including dizziness, nausea and vomiting before the MRI examination.

Sequence details

The patients were examined at a 3T MR system (MAGNETOM Trio a Tim System, Siemens AG, Erlangen, Germany). The APT images were acquired using a GRE-based CEST* WIP sequence with the following parameters: TR 3200 ms, TE 2.87 ms, FA 10 degrees, slice thickness 5 mm. The saturation module was applied before the imaging readout. Four RF pulses were repeated for 21 different offset frequencies from +5 to -5 ppm (interval is 0.5 ppm) with respect to the water frequency. MTR asymmetry analysis at the offset around 3.5 ppm is calculated to obtain APT images.

*WIP, the product is currently under development and is not for sale in the US and other countries. Its future availability cannot be ensured.

Imaging findings

In Case 1, the low-grade glioma in the left frontal lobe is not very apparent on the T1-weighted image (Fig. 2A), but shows hyperintensity on the T2-weighted image (Fig. 2B). No enhancement is revealed on the contrast-enhanced T1-weighted image (Fig. 2C). The APT map demonstrates the tumor's isointensity (Fig. 2D).

In Case 2 the solid part of the high grade glioma shows hypointensity on the T1-weighted image (Fig. 3A) and heterogeneous hyperintensity on the T2-weighted image (Fig. 3B). The hemorrhage area in the tumor shows isointensity to hyperintensity on the T1-weighted image (Fig. 3A) and hyperintensity on the T2-weighted image (Fig. 3B). Irregular enhancement is revealed on contrast-enhanced T1-weighted image (Fig. 3C). The APT map demonstrates that the tumor, including the solid and hemorrhage components, is hyperintense (Fig. 3D).

Conclusion

Our preliminary results demonstrate that this GRE-based CEST sequence can provide APT images with good quality. It has been shown that intracellular pH is almost the same in tumor and in normal tissue. High APT signal in high-grade cerebral gliomas is usually due to high protein concentration [2, 3]. The non-invasive technique of APT may be a useful tool to detect the mobile cellular proteins and an upward pH shift *in vivo*. It has the potential to be an alternative imaging modality to improve the diagnostic accuracy in grading gliomas.

References

1 Zhou J, Lal B, Wilson DA, et al. Amide Proton Transfer (APT) Contrast for Imaging of Brain Tumors. Magn Reson Med. 2003;50:1120-1126.

2 Zhou J, Blakeley JO, Hua J, et al. Practical data acquisition method for human brain tumor amide proton transfer (APT) imaging. Magn Reson Med. 2008;60(4):842-849.

3 Zhou J, Tryggestad E, Wen Z , et al. Differentiation between glioma and radiation necrosis using molecular magnetic resonance imaging of endogenous proteins and peptides. Nat Med. 2011;17(1):130-134.

Contact

Meiyun Wang, M.D., Ph.D.
Associate Director
Department of Radiology
Henan Provincial People's Hospital
Zhengzhou, Henan 450003
China
Phone: +86-371-6558-0267(0)
marian9999@163.com

Improving MR Joint Diagnostics with T1 Water Contrast Using a RESTORE Pulse

Wilhelm Ruempler, M.D.

Klinik Dr. Hancken, Stade, Germany

Inspired by a little-known publication by Radlbauer et al. [1], we have been using T1 RESTORE measurements in all joint diagnostics since June 2011, adding a -90° pulse to the T1 sequence. This option is also available for Turbo Spin Echo (TSE) sequences with turbo factor 3–4.

Extending the TE echo times from 11 to 22 and 33 ms had a similar 'whitening effect'. The RESTORE version of the T1 measurement did not cause any significant increase to the measurement time. High bandwidths (BW) were selected to produce as few chemical-shift artifacts as possible: 250 Hz/pixel for 1.5T and 450 Hz/pixel for 3T.

The 'flip-back pulse' (known as RESTORE, DRIVE, or DEFT, for example, by the various manufacturers) was originally intended for T2-weighted measurements, both to save time and to obtain a bright fluid signal in the case of a short TR. In T2-weighted spinal examinations, this lightens the cerebrospinal fluid and evens out the myelon contrast, which has proven to be unfavorable in diagnosing encephalomyelitis disseminata, yet ideal for detecting herniated discs.

T1 weightings are robust with a low artifact count, while their high fat contrast allows them to produce excellent anatomic images. The lack of fluid contrast, however, proves to be a disadvantage. Connecting a -90 degree pulse at the end of the read-out (RESTORE or flip-back pulse) shifts all transverse magnetization back towards the z-direction, thereby increasing the number of protons available for the next stimulation. As a result, the synovial fluid obtains a higher signal, meaning a new contrast is achieved in the structures surrounding the joint: synovia, capsule, cartilage, and periarticular fat. This allows synovial pathologies and/or disorders with this modified T1 weighting to be displayed without any contrast agents.

Adaptation of a standard T1 sequence: High bandwidth to ensure less chemical shift in the case of 1.5T BW 250 Hz/pixel (less than 1 pixel shift). 450 Hz/pixel for 3T BW (approximately 1 pixel shift). In the Siemens toolbox, select the RESTORE pulse on the contrast card and offset the TR against the couplings to remain in the 500 to 700 ms TR range for many of the slices.

1

35-year-old patient with recurrent swelling and pain in the left knee. **(1A)** Native conventional T1-weighted measurement, **(1B)** T1 RESTORE in the same position and the same slice thickness reveals the synovial fluid in the recessus suprapatellaris, thereby highlighting a synovia in this case with inhomogenous thickening.
The patient was back to full health after 6 weeks of rheumatic therapy.

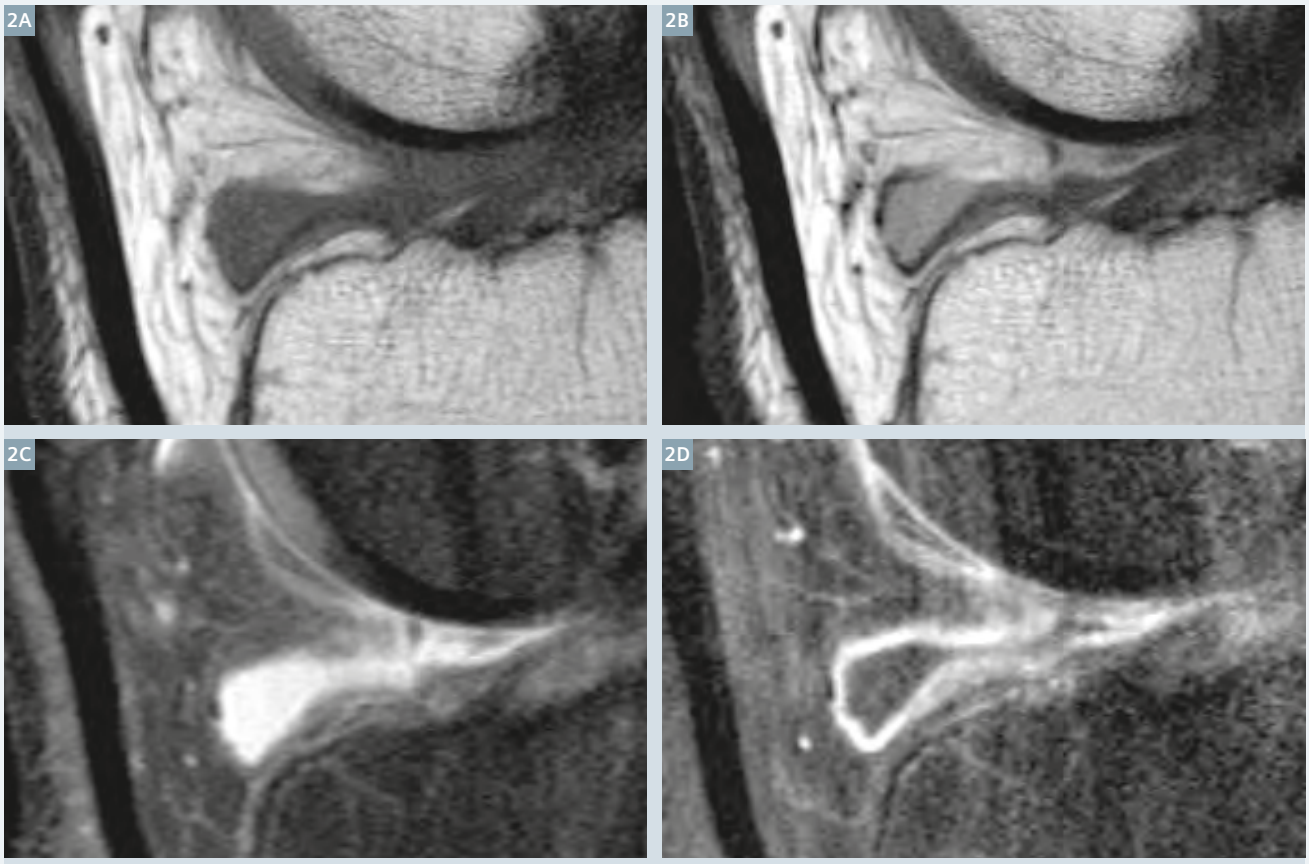

2 T1 native comparison: **(2A)** Fluid is concealed in the conventional T1-weighted sequence. T1 RESTORE **(2B)** highlights the synovial fluid and in this case reveals the significantly thickened synovia: Findings indicate psoriatic monoarthritis. **(2C)** In the proton-density-weighted sequence with fat saturation, the synovia which is thickened to 2 mm is concealed by the high T2 contrast. **(2D)** The synovia is only visible in the T1 FS sequence for a few minutes following the addition of an intravenous contrast agent. In the later measurements, the contrast agent is excreted into the joint cavity and blurs the outline of the synovia on the side of the joint once again.

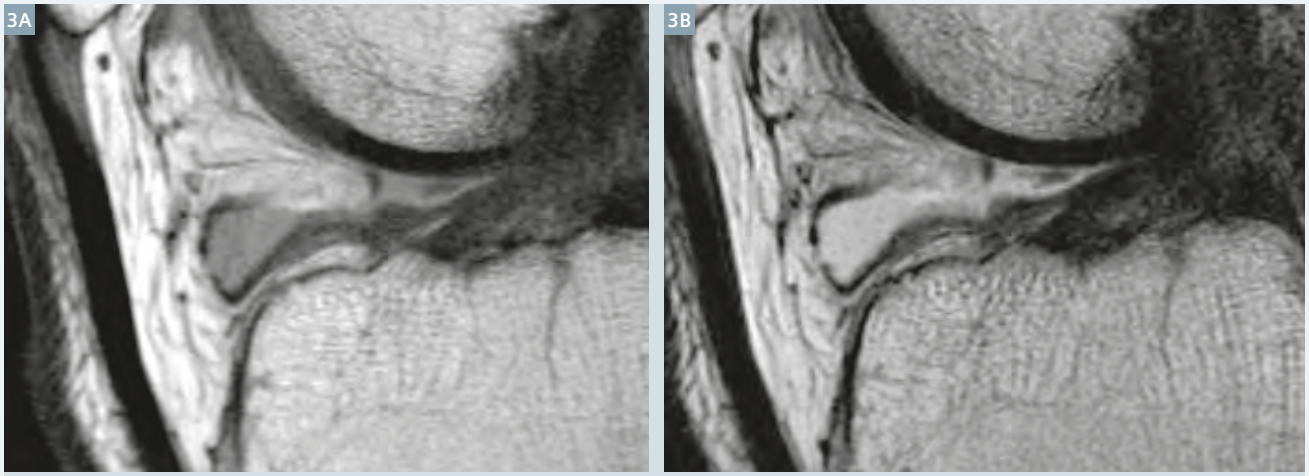

3 **(3A)** T1 RESTORE highlights fat/synovia/synovial fluid, whereas **(3B)** no contrast between fat/fluid can be detected in the PD-weighted sequence without FS, i.e. fat and water are equally light. Once again, significant thickening of the synovial membrane can be seen along with an effusion that spreads over the infrapatellar fat pad.

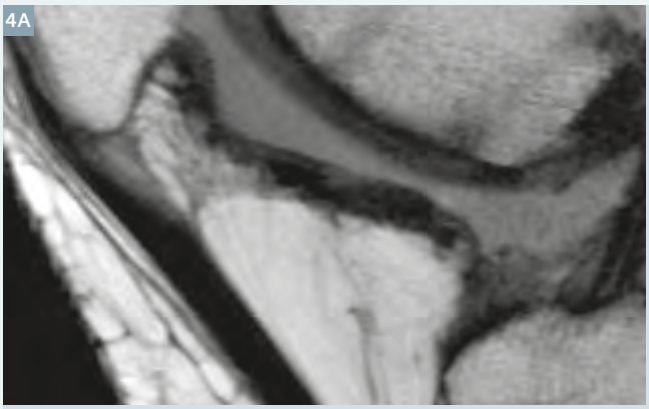

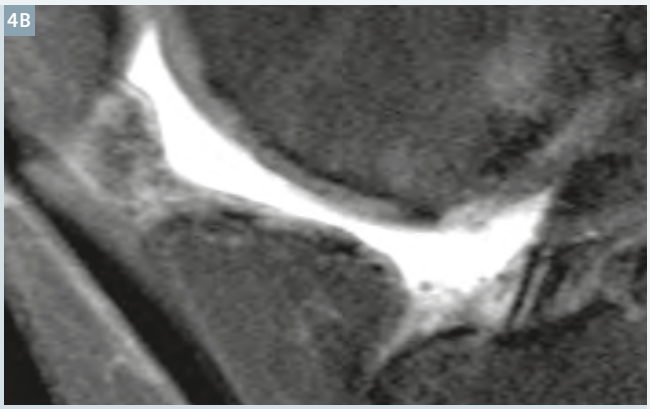

4 **Arthrofibrosis.** Unlike common PD FS sequences **(4A)**, T1 RESTORE **(4B)** highlights the severe fibrotic synovial proliferation. The knee joint is suffering from extreme limitations to its range of flexion/extension consistent with this type of membrane scarring. Condition after three rounds of arthroscopic surgery (cartilage grinding) and a partial resection of the medial meniscus. One of the most common causes of this frequently painful scarring, along with primary inflammatory rheumatic diseases.

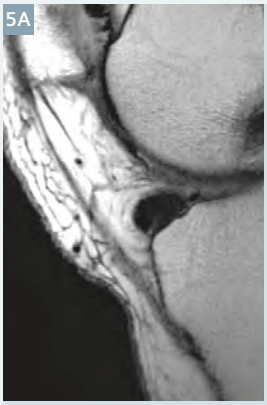

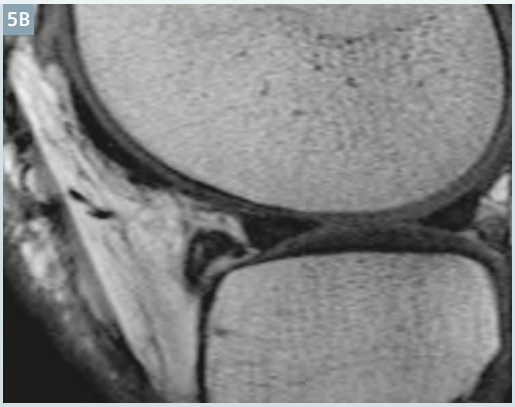

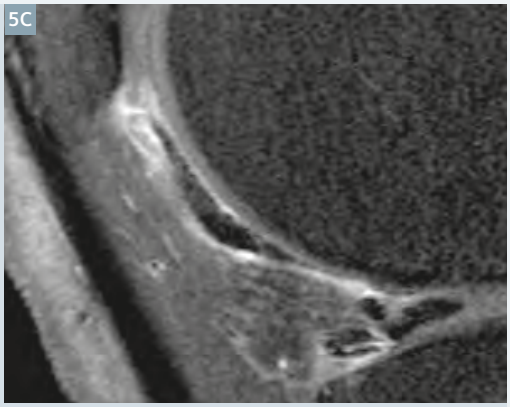

5 Thanks to its fluid contrast with high spatial resolution, the T1 RESTORE sequence **(5A, B)** displays conical or even oval-shaped synovial villi, along with low-signal lesions in the synovia that indicate hemosiderin (blood) or calcium (the latter is easily excluded with an X-ray). The distribution pattern of the synovial specks is typical of diffuse pigmented villonodular synovitis (PVNS), which has been histologically confirmed.

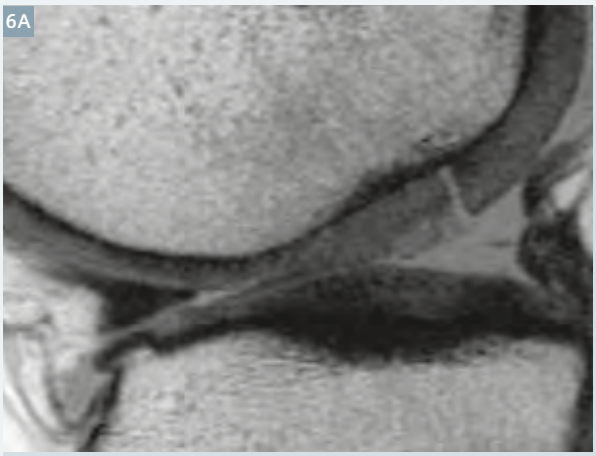

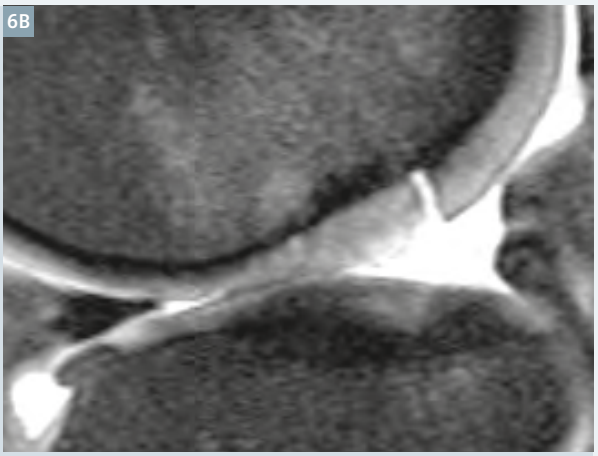

6 **Cartilage diagnostics with T1 RESTORE**. **(6A)** The moderate T1 fluid contrast reveals a one-millimeter-small, free fragment that can no longer be seen in the sharp PD FS contrast image **(6B)**. Furthermore, the third-degree cartilage lesion – including the reactive accompanying subchondral cortical sclerosis – is illustrated more clearly in the T1 measurement. The fibrillar protrusion of cartilage on the surface is displayed equally clearly, if not better.

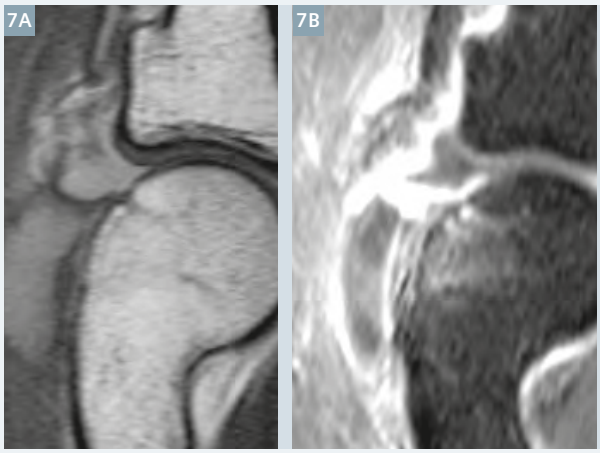

7

RESTORE in ligament diagnostics. Even capsule pathologies can frequently be examined with significantly greater accuracy (using the moderate fluid contrast). The extravasation of synovial fluid is particularly clear in the contrast agent study on the right. The type of capsule lesion (in this case, atraumatic) and the leakage in the capsule that has been destroyed by inflammation are concealed in the T1 FS post-gadolinium contrast agent.

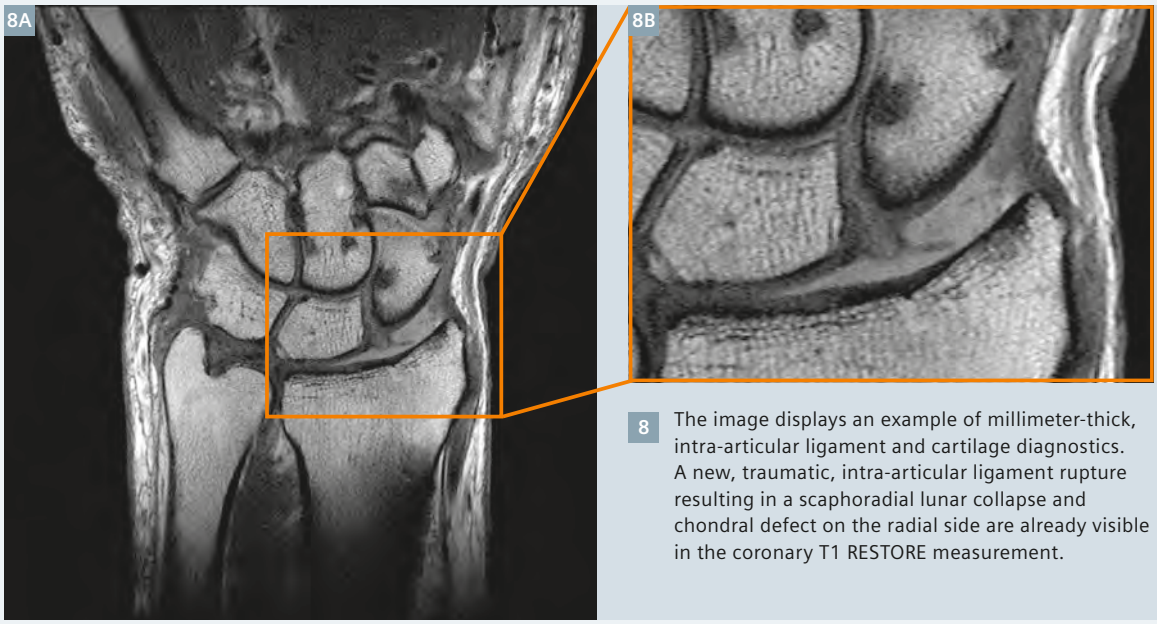

8 The image displays an example of millimeter-thick, intra-articular ligament and cartilage diagnostics. A new, traumatic, intra-articular ligament rupture resulting in a scaphoradial lunar collapse and chondral defect on the radial side are already visible in the coronary T1 RESTORE measurement.

Summary

It is thanks to the moderate fluid contrast in the T1 RESTORE sequence that it is possible to depict the smallest synovial, cartilage, and ligament pathologies, which are frequently concealed (at least partially) in the significantly sharper contrast of the conventional PD FS measurements. Furthermore, PD FS sequences are often blurred due to their significantly greater susceptibility to artifacts, which is why we always perform T1 measurements with a RESTORE pulse in joint diagnostics. Amongst other reasons, this allows us to focus much more attention on the chronic, fibrotic joint pathologies that are frequently concealed in the imaging data. In such cases, contrast agents are only required to verify the florid-vascular part of the inflammation.

References

1 Radlbauer R, Lomoschitz F, Salomonowitz E, Eberhardt KE, Stadlbauer A. MR imaging of the knee: Improvement of signal and contrast of T1 Weighted turbo spin echo sequences by applying a driven equilibrium pulse (DRIVE). Eur J Radiol. 2010 Aug;75(2).

Contact

Wilhelm Ruempler, M.D.
Harsefelder Str. 8
21680 Stade
Germany
Phone: +49 (0) 4141/604100
ruempler@hancken.de

Case Report: Perthes Lesion

Coley C. Gatlin, M.D.; Charles P. Ho, Ph.D., M.D.

Steadman Philippon Research Institute, Vail, CO, USA

History of present illness

A 23-year-old female with no significant past medical history sustained a traumatic left anterior shoulder dislocation (1st time) while doing a back tuck (standing back flip). She was able to relocate the dislocation on her own after approximately 3 to 4 minutes and reported significant pain relief after reduction. The injury occurred 4 days prior to presenting to the orthopedic physician for further evaluation. Since the initial event, she complains of diffuse shoulder pain, weakness, and instability. She reports being unable to lift or reach for objects secondary to pain.

Physical examination

There is no external rash, bruising, swelling, deformity, or shoulder girdle muscle atrophy. Range of motion passively is 160 degrees of forward elevation, 90 degrees of abduction, and 40 degrees of external rotation. Active range of motion was deferred. Strength testing is 4+/5 with forward elevation, abduction, external rotation, and internal rotation. She has 5/5 deltoid strength. The patient had negative provocative testing of the rotator cuff and acromioclavicular joint. She had positive anterior shoulder apprehension and a positive O'Brien's test (labral provocative testing).

Radiographs

Left shoulder radiographs demonstrated anatomic alignment of the glenohumeral and acromioclavicular joints with no fracture, bony lesion, or rim avulsion fragments.

Clinical assessment

First-time traumatic anterior shoulder dislocation with resultant anterior shoulder instability.

Differential diagnosis for anterior glenolabral injuries

- Bankart lesion
- bony Bankart lesion
- anterior labroligamentous periosteal sleeve avulsion (ALPSA)
- Perthes lesion
- glenolabral articular disruption (GLAD)
- humeral avulsion of the glenohumeral ligament (HAGL)
- bony humeral avulsion of the glenohumeral ligament (BHAGL)

Plan

At the patient's initial presentation, the treatment options included conservative treatment versus conservative therapy and obtaining additional diagnostic imaging studies. After discussion with the patient, additional imaging was performed to assess further the degree of injury and inform better the treatment options.

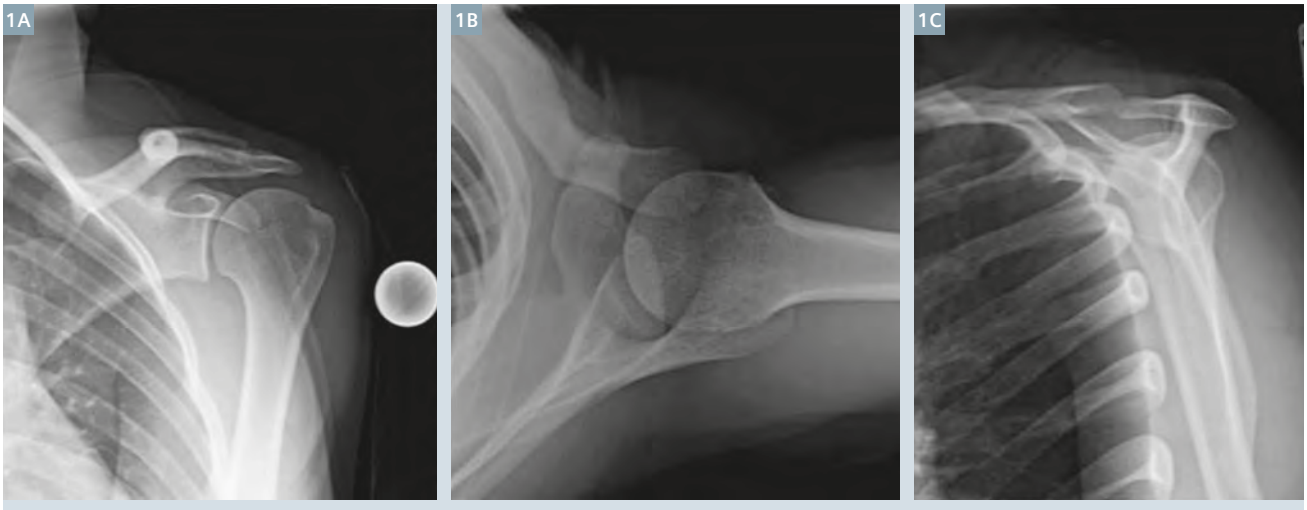

1 Unremarkable left shoulder AP **(1A)** and axillary **(1B)** and scapular Y **(1C)** views radiographs of the left shoulder.

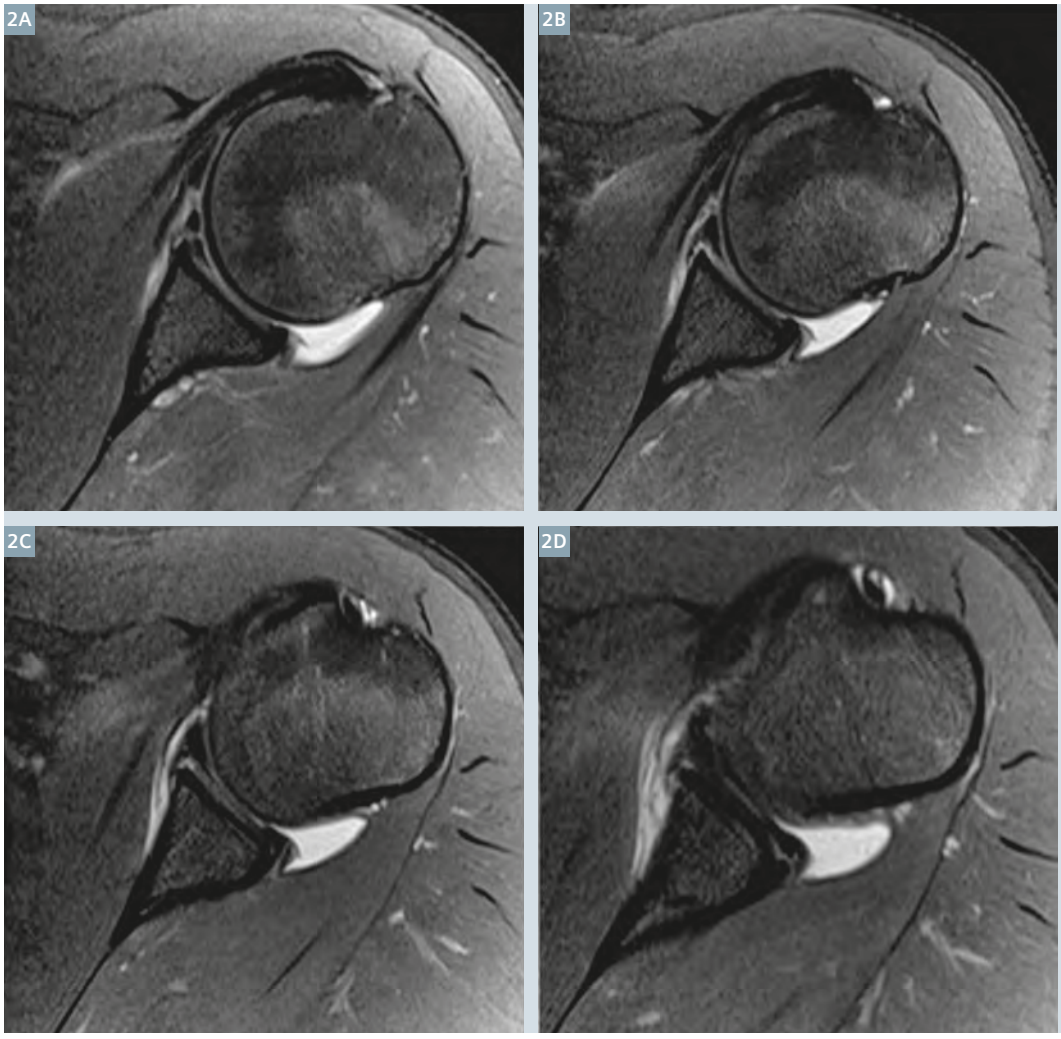

2

Sequential axial proton density turbo spin echo fat saturation images of the left shoulder from superior to inferior. Sequential MR images extending from superior to inferior along the anterior labrum. The images show labral undermining and partial detachment of the anterior inferior labrum with anterior inferior capsular and periosteal stripping along the anterior inferior glenoid rim and neck.

MR imaging findings

1. Mild rotator cuff tendinosis. No focal rotator cuff tear.
2. Undermining and partial detachment of the anterior inferior labrum with anterior inferior capsular and periosteal stripping along the anterior inferior glenoid rim and neck, with little or no displacement, compatible with a Bankart lesion and Perthes lesion variant.
3. Broad shallow Hill-Sachs impaction lesion (1–2 mm depth) over about 3 cm wide area of posterolateral humeral head.
4. Strain and possible slight undermining or partial tearing of the long head biceps tendon at the biceps anchor.
5. Moderate glenohumeral joint effusion with capsular distention, stripping, and sprain and partial tearing stripping of the anterior shoulder capsule along anterior labrum and glenoid.

Discussion

The Perthes lesion was initially described by a German surgeon named Georg Clemens Perthes (1869–1927) in 1905 [1, 3]. The injury is an anterior glenohumeral injury in which the anterior labrum is lifted from the edge of the glenoid along with a sleeve of periosteum which is undermined but not torn, stripped extending medially off the glenoid rim and scapular neck [1]. Although the labrum may be normally positioned, it no longer provides functional stability to the humeral head. This is predominantly due to the loss of the normal stabilizing influence of the anterior inferior labrum and inferior glenohumeral ligament. There is little/no displacement of the labrum, in contrast to the typical anterior medial capsulolabral and periosteal sleeve displacement of the ALPSA lesion.

Radiographic features

Standard shoulder radiographs may be normal or show a Hill Sachs lesion.

MR imaging: The Perthes lesion may be demonstrated by fluid extending beneath the labrum and filling the space between the elevated periosteum anteriorly and the scapula

posteriorly. The labrum is often normally positioned and it may be difficult to appreciate the lesion especially if scarring obliterates the space deep to the labrum [1, 7]. The presence of a joint effusion, typically present in more acute injury (as in this patient), or MR arthrogram (which may be considered in more chronic presentation) may help in the detection of this lesion [5, 6]. Some authors have recommended special positioning of the shoulder joint, specifically the ABER (abduction-external rotation) position, in cases of anterior glenohumeral injury to further enhance sensitivity and specificity for the detection of this lesion [4, 6].

In one small study, the Perthes lesion was best seen on images obtained in the abduction–external rotation position, which allowed visualization of the labral tear in all patients. On the images obtained for five out of 10 patients (for three of the five, these were MR arthrograms), the tear could be seen only in abduction–external rotation position views [1]. However, the ABER position, by putting abduction external rotation traction on the anterior to anterior inferior capsulolabral complex, may also tend to reduce the separation and elevation of the labrum and periosteum back to the glenoid margin and perhaps then decreasing detection of the Perthes lesion.

Treatment and prognosis

Once the diagnosis is made, all cases are surgically repaired because otherwise the shoulder joint remains unstable. Typically, these lesions are repaired via an arthroscopic approach. During arthroscopic surgery, the Perthes lesion may appear indistinguishable from a normal labrum and intraoperative probing of the labrum is necessary to show the labral detachment from the glenoid rim. Therefore, the treating surgeon should be aware of the MR findings that indicate the possibility of a Perthes lesion prior to surgery as it may alter surgical treatment approach and planning [5, 8].

References

1 Wischer Thorsten K., Miriam A. Bredella, Harry K. Genant et al. "Perthes Lesion (A Variant of the Bankart Lesion): MR Imaging and MR Arthrographic Findings with Surgical Correlation." Am. J. Roentgenol. 178, no. 1 (January 1, 2002): 233-237.

2 Bankart A. The pathology and treatment of recurrent dislocation of the shoulder joint. Br J Surg 1938;26:23–29

3 Perthes G. Ueber operationen bei habitueller schulterluxation. Dtsch Z Chir 1906;85:199–227

4 Cvitanic O, Tirman PF, Feller JF, Bost FW, Minter J, Carroll KW. Using abduction and external rotation of the shoulder to increase the sensitivity of MR arthrography in revealing tears of the anterior glenoid labrum. AJR 1997;169:837–844

5 Arciero A, Boone JL. First-time anterior shoulder dislocations: has the standard changed? Br J Sports Med 2010; 44:355–360.

6 Waldt S, Burkart A, Imhoff AB, Bruegel M. Anterior Shoulder Instability: Accuracy of MR Arthrography in the Classification of Anteroinferior Labroligamentous Injuries Radiology November 2005 237:2 578-583

7 Stoller DW. MR arthrography of the glenohumeraljoint. Radiol Clin North Am 1997; 35:97–116.

8 Taylor DC, Arciero RA. Pathologic changes associated with shoulder dislocations: arthroscopic and physical examination findings in first-time, traumatic anterior dislocations. Am J Sports Med 1997; 25:306–311.

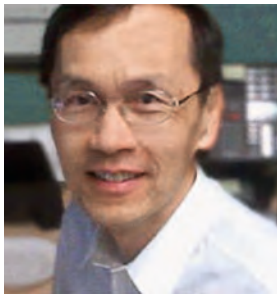

Contact

Charles P. Ho, Ph.D., M.D.
Steadman Philippon Research Institute
181 W. Meadow Drive,
Suite 1000,
Vail, CO 81657, USA
charles.ho@thesteadmanclinic.com

Listen – Discuss – Share

9th MAGNETOM World Summit

June 12-15, 2014, Heythrop Park, Oxfordshire, UK

The MAGNETOM World Summit is an excellent platform to establish personal contacts, exchange valuable information, learn from the experience of other users and to share your own expertise.

Lectures and presentations from experts in the field will allow you to be exposed to new ideas and alternative clinical approaches that might help you to improve your clinical and financial outcomes.

> "The 8th MAGNETOM World Summit in Paris was such a fantastic experience and I learnt so much and enjoyed the time there immensely. I have made some great professional contacts that will be incredibly useful in furthering some projects at Peter MacCallum. I would never have had the opportunity to form these contacts had it not been for this summit. It was one of the best organized conferences I have been to and the calibre of the presentations was astounding."
>
> Noelene Bergen, Peter MacCallum Cancer Centre, Melbourne, Australia

For details on the agenda and registration, please contact your local Siemens Representative.

MAGNETOM Aera – Combining Throughput and Highest Quality Spine Imaging in an Optimized Clinical Workflow

Johan Dehem, M.D.

VZW Jan Yperman, Ieper, Belgium

Cervical spine imaging

Thanks to Tim's flexibility with coil combinations, MR imaging of the cervical spine is in 99% percent of the cases a swift and easy standard program evaluating degenerative disease.

Figure 1 shows a case of herniated disk where you can clearly exclude myelopathie since the T2-weighted MEDIC sequence demonstrates the 'butterfly' of normal gray matter in the myelon.

1 T2-weighted MEDIC sequence to exclude myelopathie.

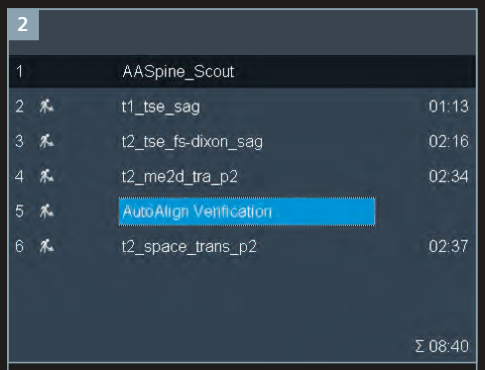

2 AutoAlign in the Spine Dot Engine.

Despite the high resolution (2.1 mm slice thickness for the sagittal T2w Dixon TSE) scanning times for the c-spine are very patient friendly. Moreover the Spine Dot Engine (Fig. 2) helps to align and plan the slices speeding up the scanning by avoiding planning gaps during scanning. We are thus able to schedule patients every 10 minutes.

The cervical spine can sometimes be quite challenging, be it technically or diagnostically.

In this case metal* susceptibility artifacts are reduced using WARP imaging (Fig. 3). The Spine Dot Engine has a convenient option to change the scanning protocol on the fly from normal to 'metal suppression' WARP mode by a simple mouse click, thereby eliminating the need to obtain sequences from another program or to change all of your parameters in the sequence card for each and every sequence. Metal artifact reduction is only a mouse click away.

3 WARP imaging to reduce metal susceptibility artifacts.

*The MRI restrictions (if any) of the metal implant must be considered prior to patient undergoing MRI exam. MR imaging of patients with metallic implants brings specific risks. However, certain implants are approved by the governing regulatory bodies to be MR conditionally safe. For such implants, the previously mentioned warning may not be applicable. Please contact the implant manufacturer for the specific conditional information.
The conditions for MR safety are the responsibility of the implant manufacturer, not of Siemens.

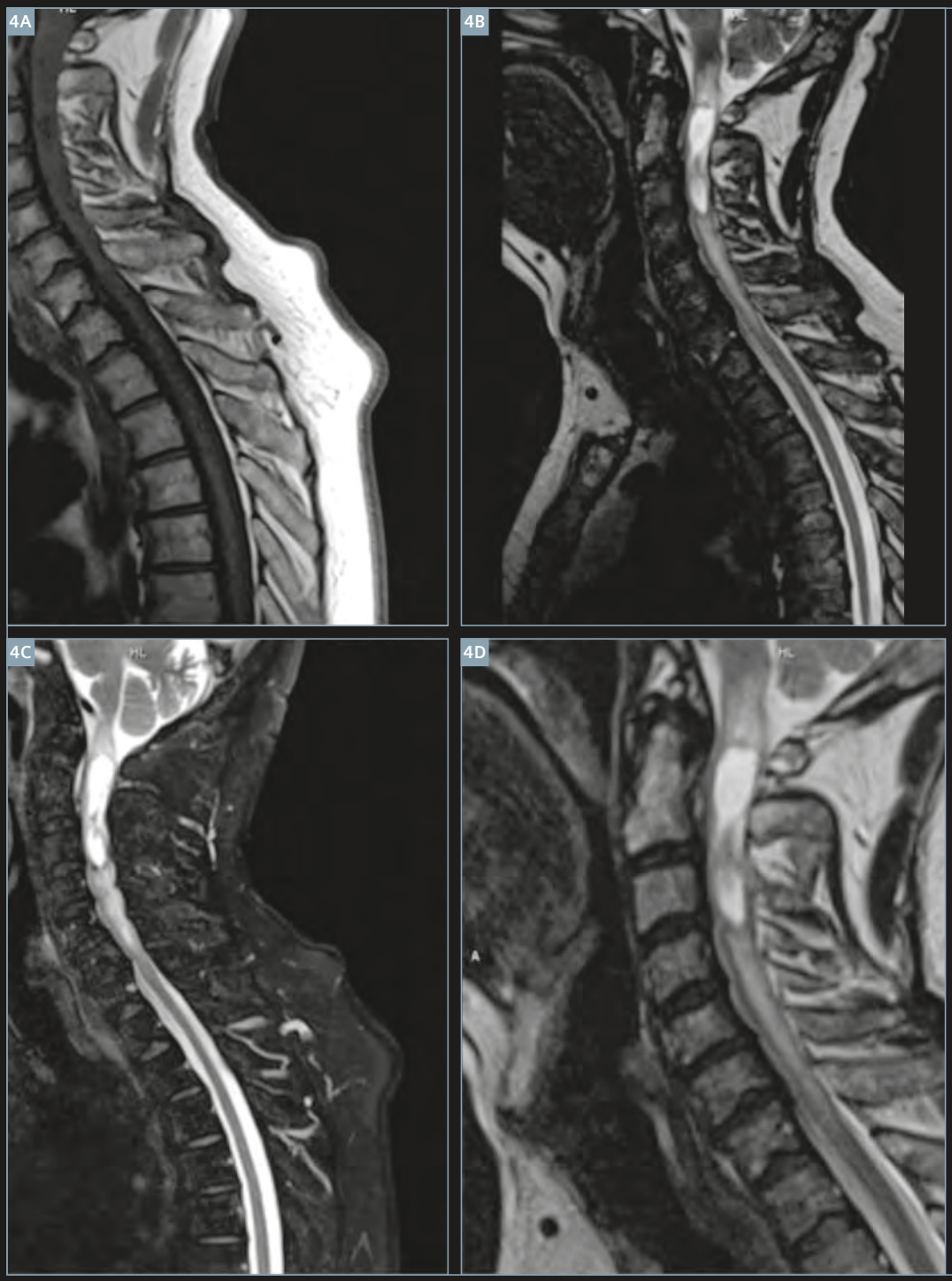

4

T2-weighted TSE Dixon nicely demonstrates intramedullary partly cystic mass with apical T2 hypointense capping and adjacent edema cranially and caudally extending.

This 65-year-old man suffers from numbness in both hands and loss of force in the upper limb bilaterally. An MRI c-spine was ordered to exclude myelopathy. On T1 the lesion is slightly hypointense. T2w TSE Dixon nicely demonstrates intramedullary partly cystic mass with apical T2 hypointense capping and adjacent edema cranially and caudally extending (Fig. 4).

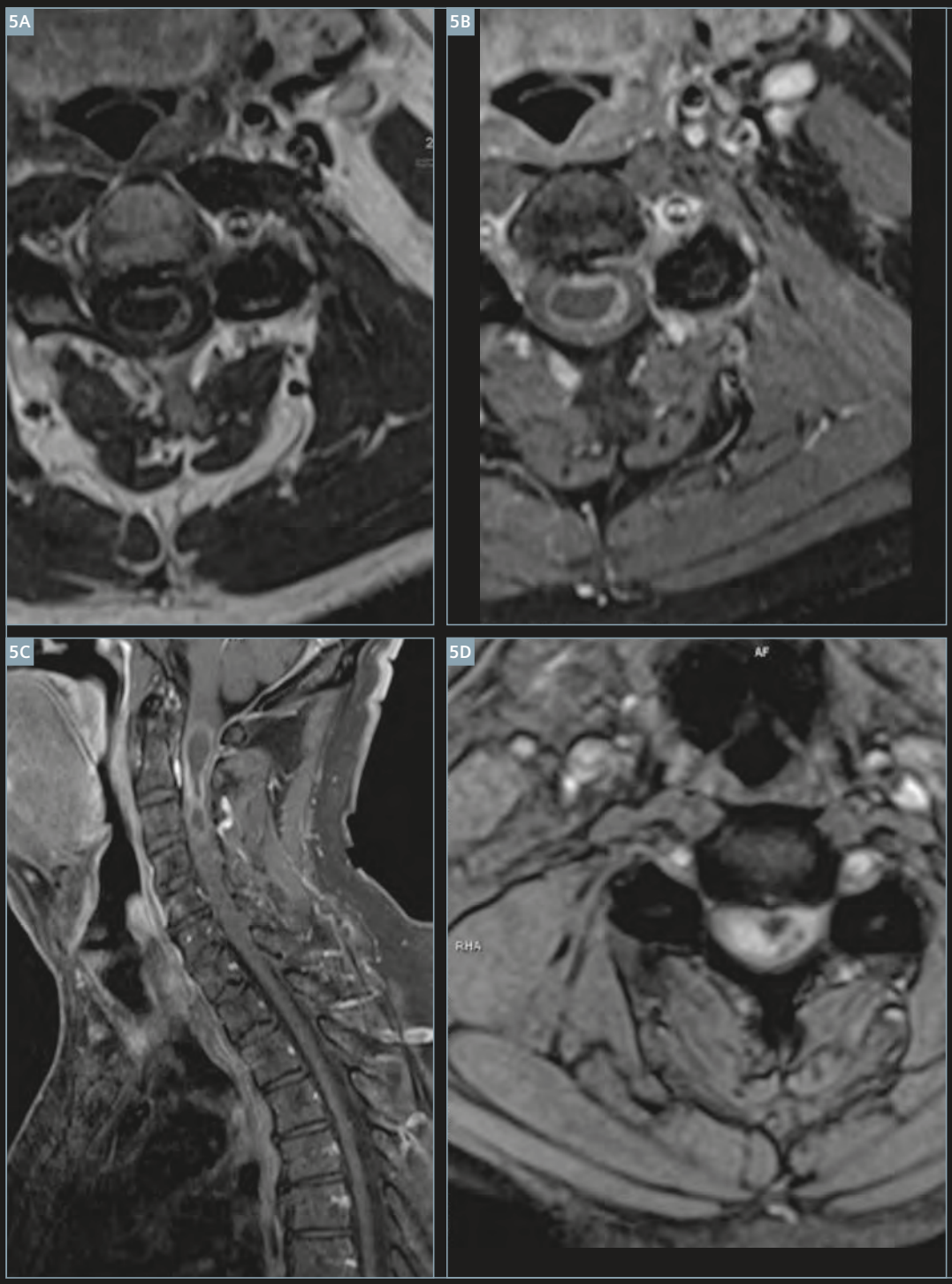

5

T1w **(5A)**, axial T1w FS Dixon technique **(5B)**, sagittal Dixon fat sat **(5C)** and T2w MEDIC **(5D)**.

Axial T1w and T1w FS Dixon technique and sagittal Dixon fat sat (impeccable as always) nicely demonstrate the peripheral contrast enhancement and central necrosis. The T2w MEDIC demonstrates inlaying hemosiderine, giving away the diagnosis of ependymoma.

Spine Dot Engine

Since the Spine Dot Engine starts with a 3D localizer on C2 level – be it for lumbar, dorsal or cervical spine – a full-spine scan is no big deal. We start the Spine Dot Engine on the lumbar region and simply add the T2, T2 STIR and T1 TSE once for the cervico-dorsal spine. Inline composing or adjusted composing in *syngo*.via gives you highest quality full-spine images with good detail of e.g. adjacent lymph nodes in mediastinum or retro peritoneum.

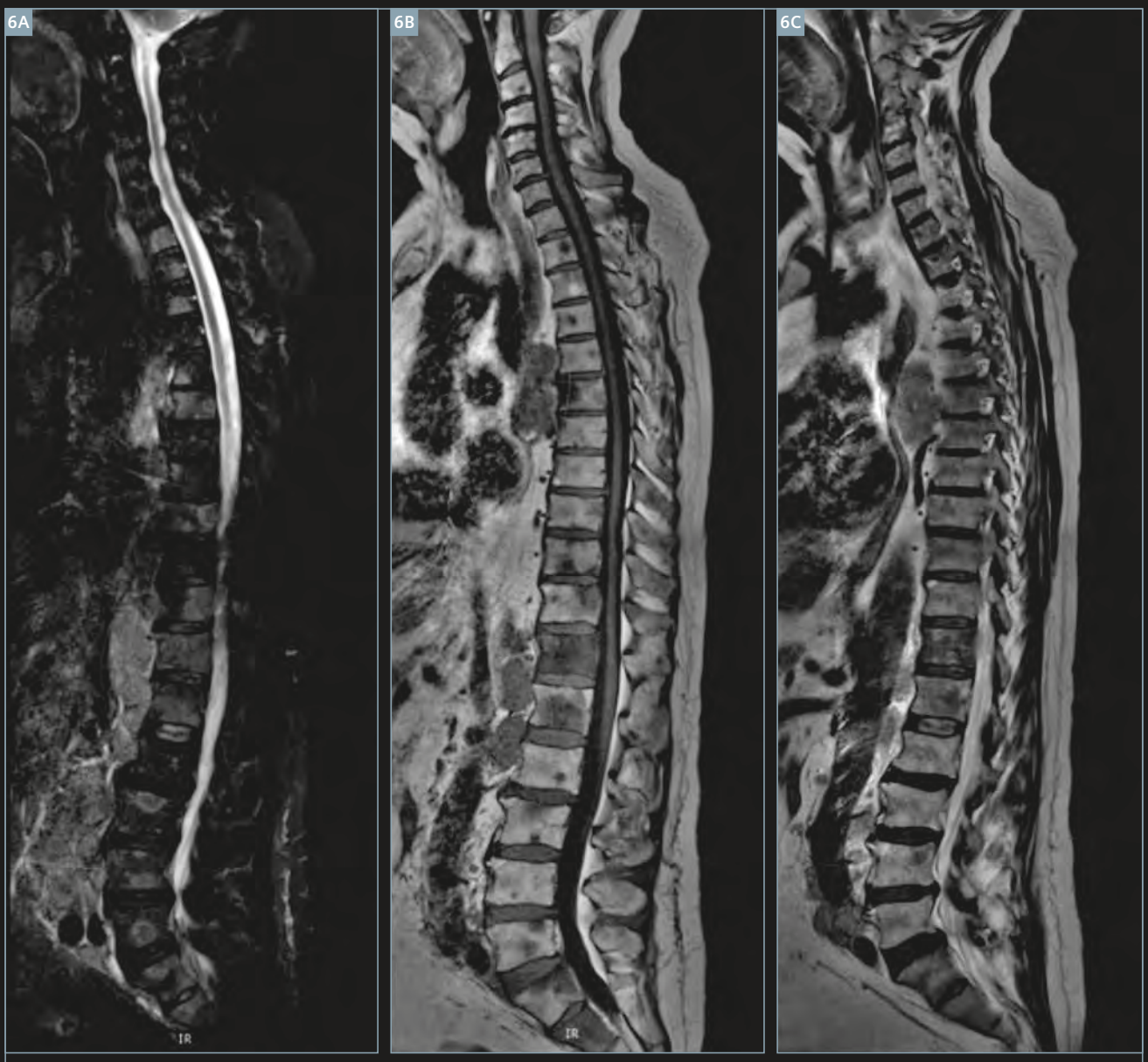

6 Example of prevertebral detail: Full spine examination clearly depicts bone metastasis in this prostate cancer patient but at the same time reveals retroperitoneal and mediastinal lymphadenopathies.

Lumbar spine imaging

Lumbar spine examination is part of the daily routine of radiology, so maintaining high image quality is paramount. Since most patients complain of pain, imaging time should also be as short as possible to make optimal use of the window of opportunity that you have to scan the patient. In our institution we need 10 minutes to install the patient, and scan 3 sagittal views, one coronal and one axial series.

7

In this young patient a herniated disk with ascending extrusion is demonstrated. Comprehensive imaging using 5 high res sequences in a 10-minute scanning slot.

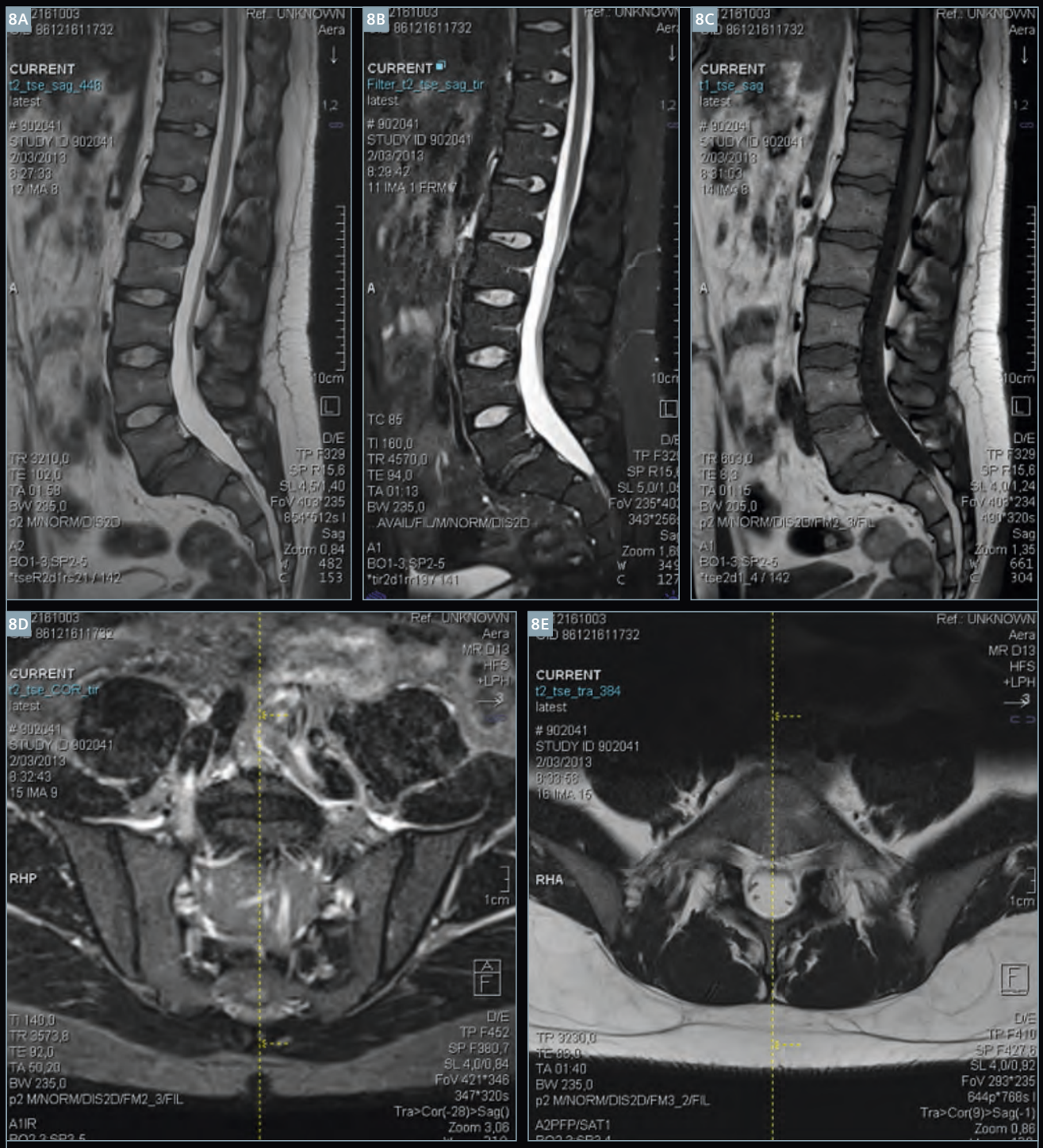

8 Spondylolysis and listhesis.

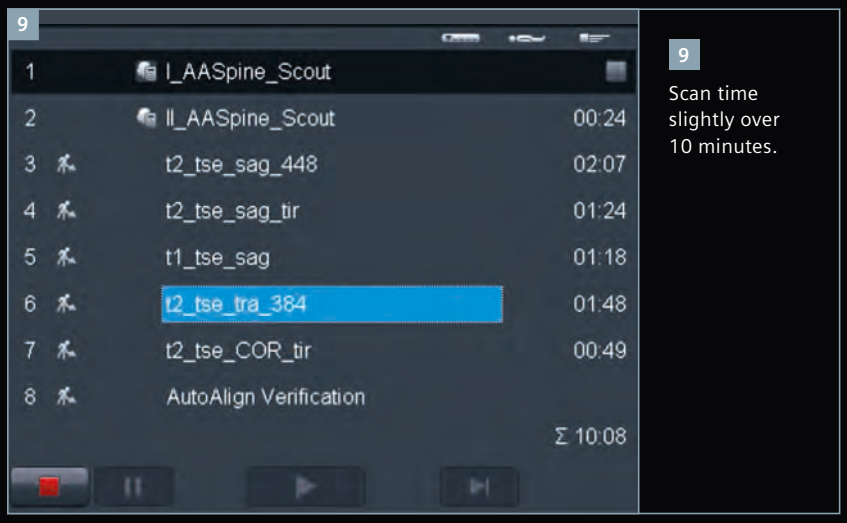

9 Scan time slightly over 10 minutes.

High quality and high speed do go together indeed! When you compare a contemporary lumbar spine on MAGNETOM Aera (Fig. 11) with the spine examination we used to do on the MAGNETOM Symphony a Tim System (Fig. 10) you do see an improvement in scanning times (up to 50% faster) for better image quality. Figures 10 (SATS) and 11 (Aera) show a case of a patient with a tethered cord where the image quality improvement is visible at 30% faster examination time.

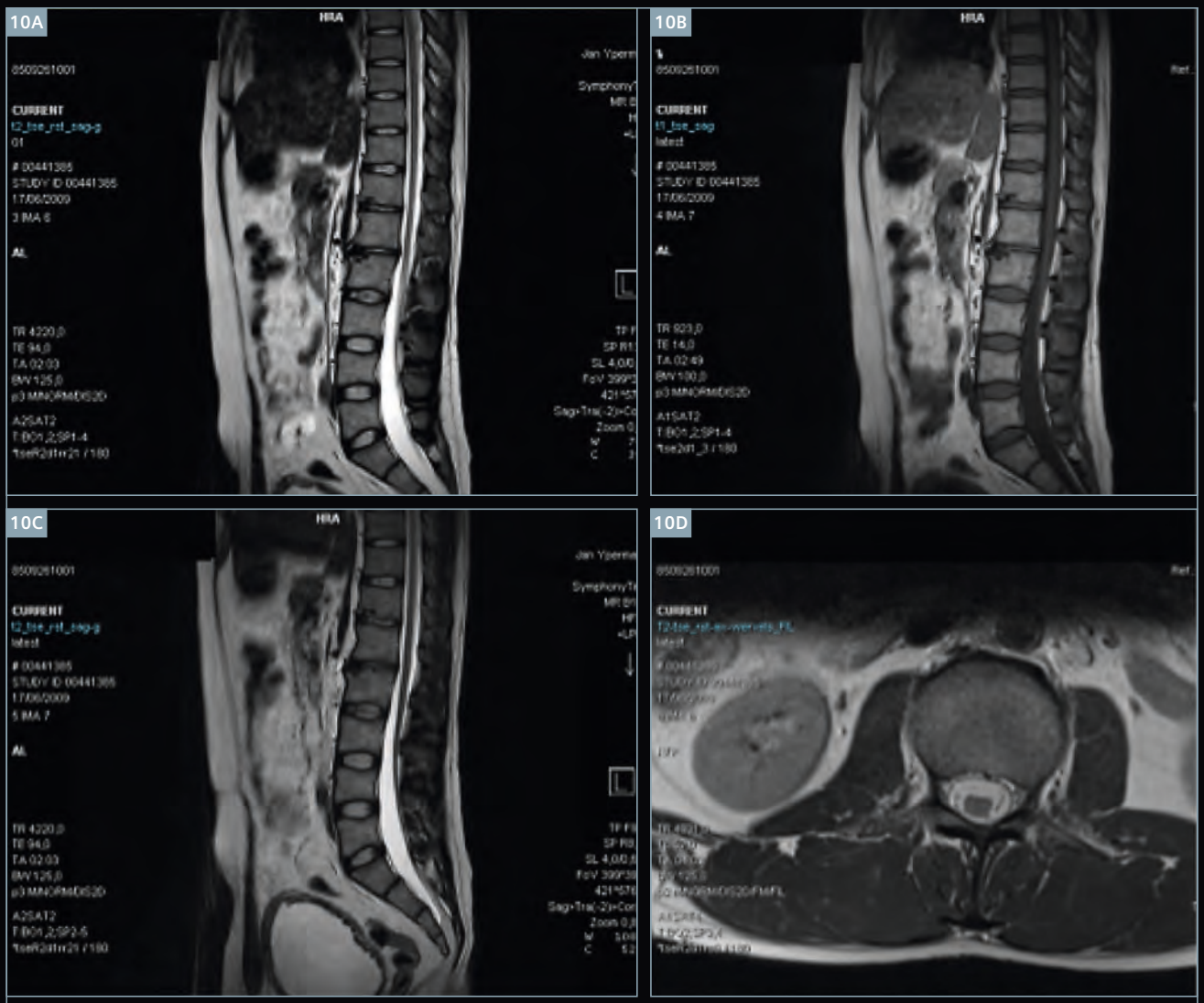

10 A patient with a tethered cord. Note the neurogenic bladder and the small lipomeningocele. Images have been acquired using a MAGNETOM Symphony, a Tim system. The imaging time was well over 2 minutes for each acquisition.

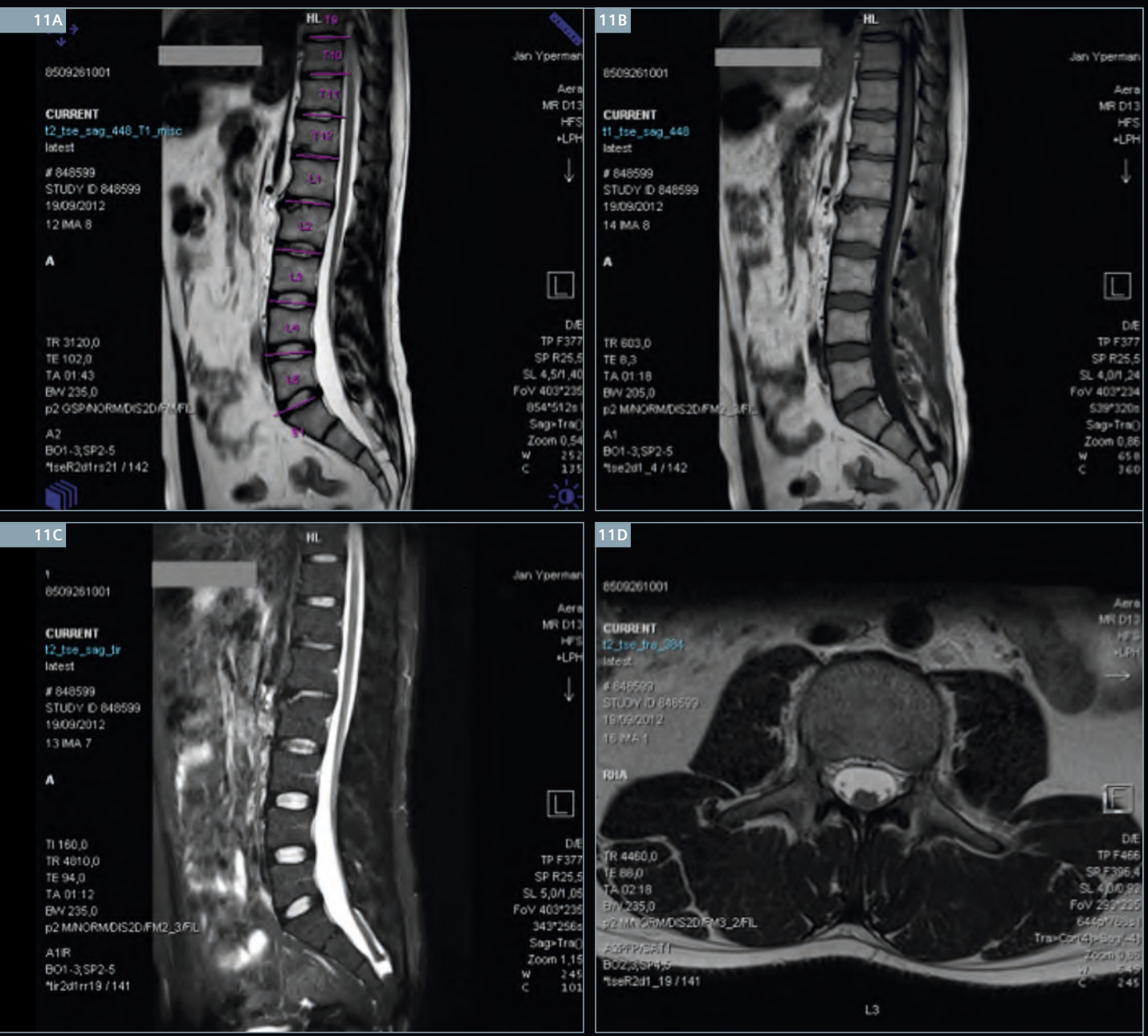

11 Same patient as in figure 10 on the MAGNETOM Aera system. Sharpness and homogeneity of the images has improved while acquisition times have dropped up to 50% (just take a look at the sag T1). Note tethered cord, neurogenic bladder and the small lipomeningocele.

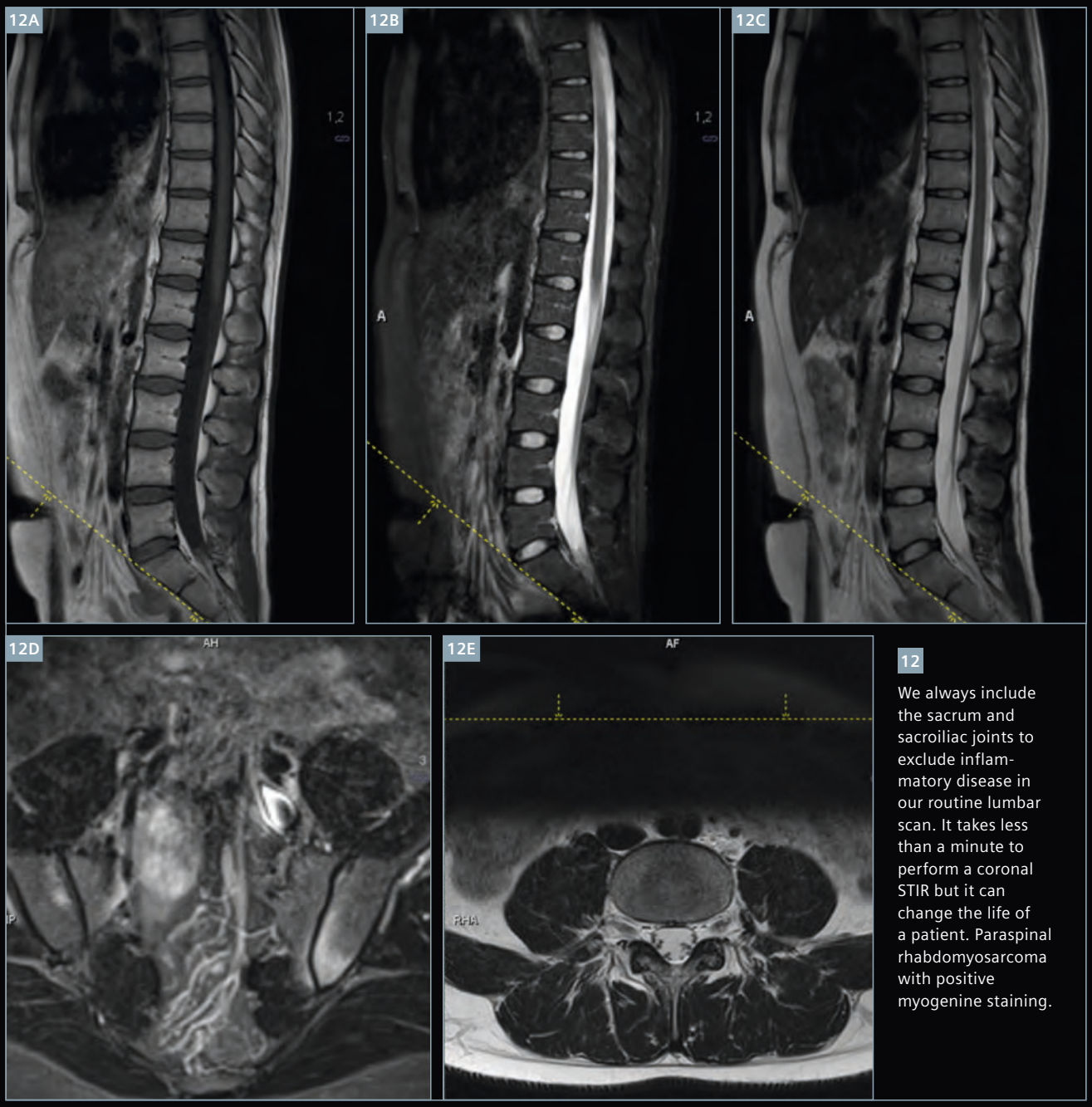

12
We always include the sacrum and sacroiliac joints to exclude inflammatory disease in our routine lumbar scan. It takes less than a minute to perform a coronal STIR but it can change the life of a patient. Paraspinal rhabdomyosarcoma with positive myogenine staining.

Sometimes, however, a simple lumbar spine scan turns out to be not so simple at all and we require additional imaging such as in the case of this 40-year-old lady in agony for the previous 8 days (Fig. 13–16). It turned out to be nerve root and thecal sac compression by a neoplastic lesion in the L3 vertebra. Additional sequences after gadolinium were performed. Dixon axial and sagittal T1w and T1w FS images nicely demonstrate the tumor. The additional 3D VIBE CP (with breath-hold 21 s) gives a nice 3D overview. The axial diffusion-weighted imaging is in favor of malignant disease with a low ADC value. Again speed is important while imaging a patient in pain. It turned out to be a paraspinal rhabdomyosarcoma with positive myogenine staining.

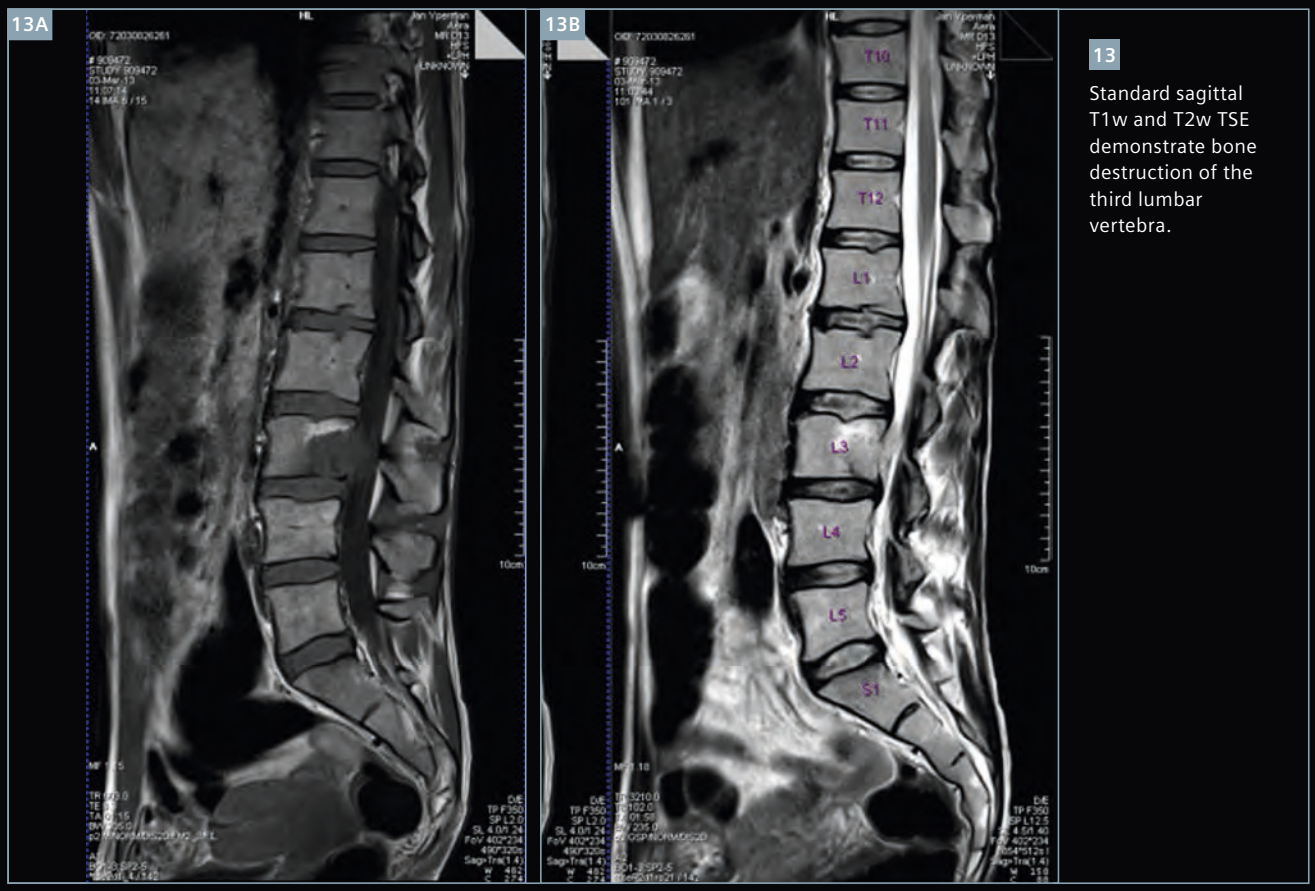

13

Standard sagittal T1w and T2w TSE demonstrate bone destruction of the third lumbar vertebra.

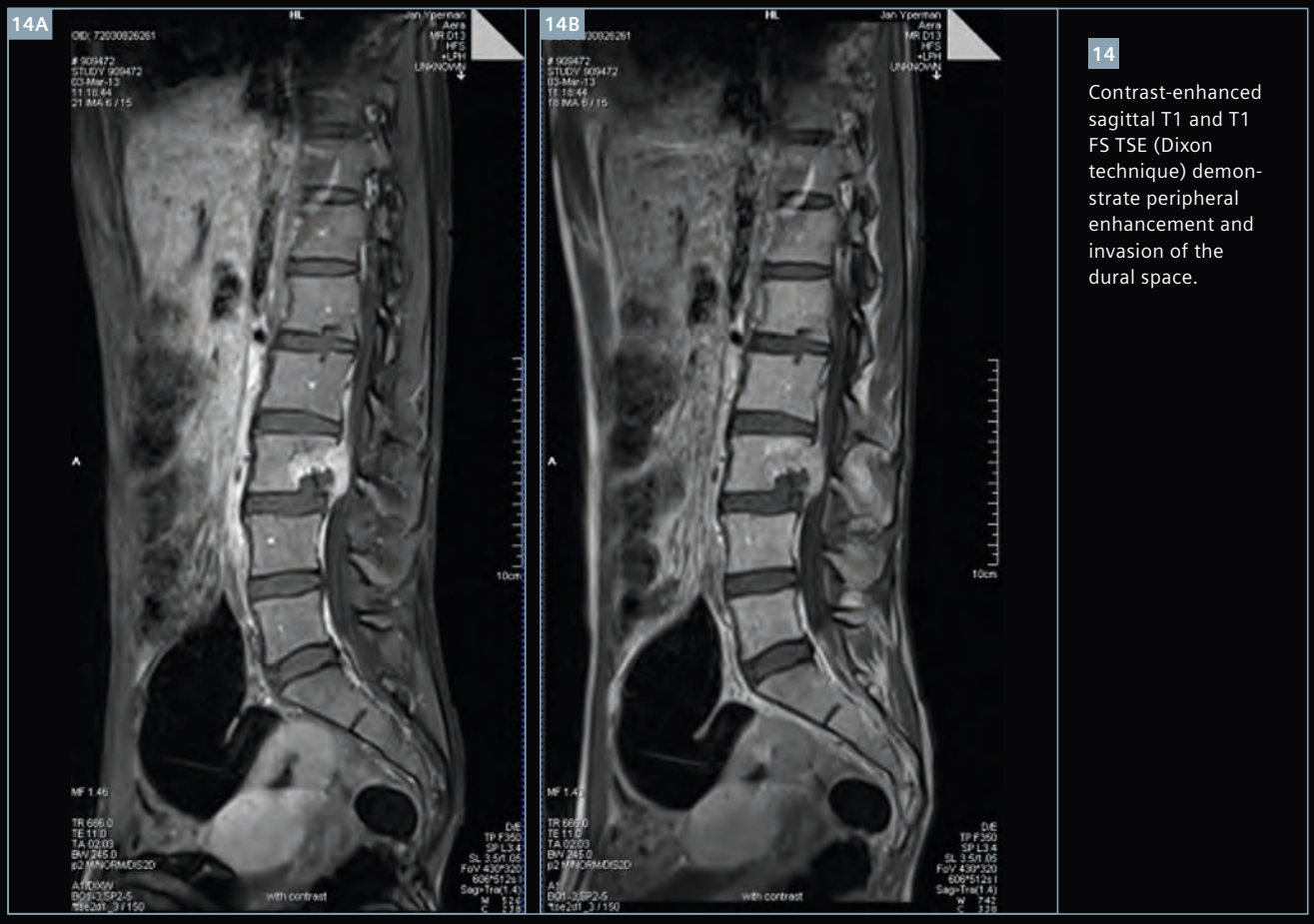

14

Contrast-enhanced sagittal T1 and T1 FS TSE (Dixon technique) demonstrate peripheral enhancement and invasion of the dural space.

15

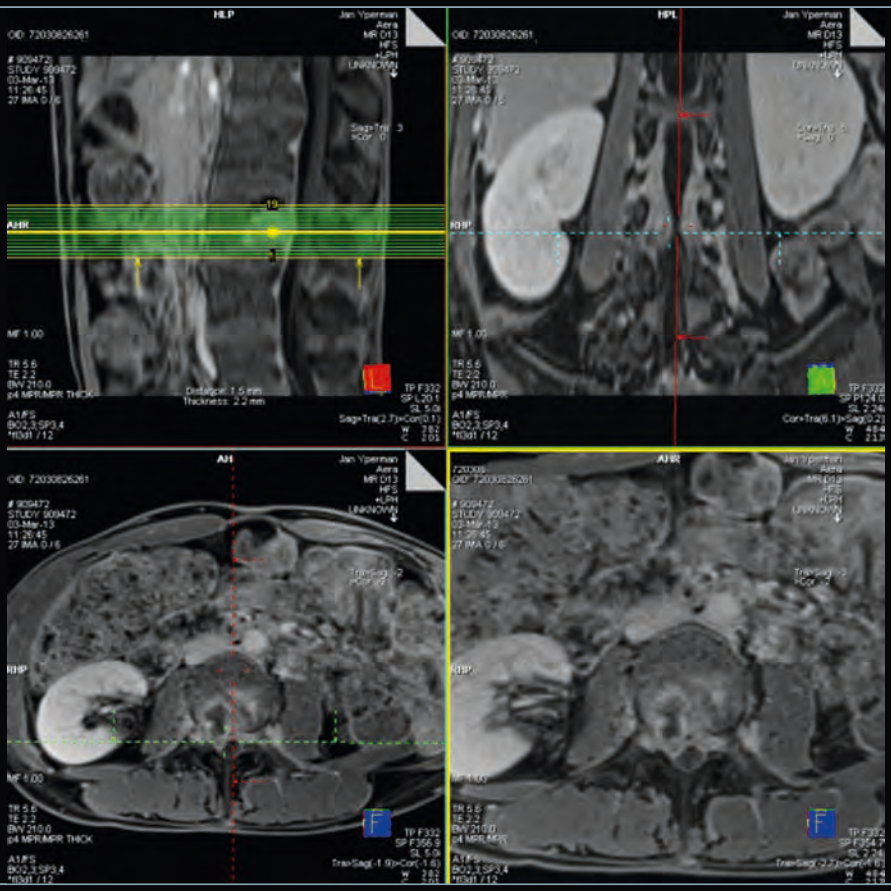

15

Contrast-enhanced T1w VIBE: breath-hold 21 seconds axial acquisition with coronal reconstructions demonstrate tumor extending in the spinal canal.

16

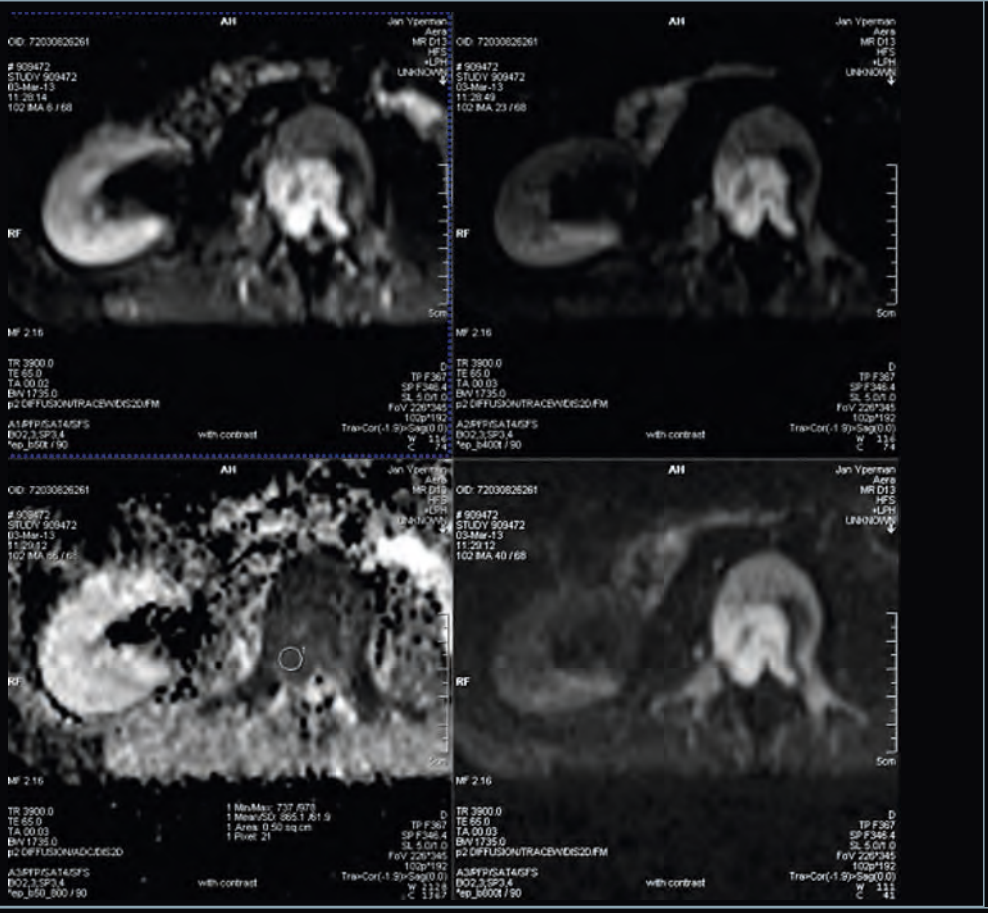

16

Diffusion-weighted imaging demonstrates restricted diffusion in favor of highly malignant lesion.

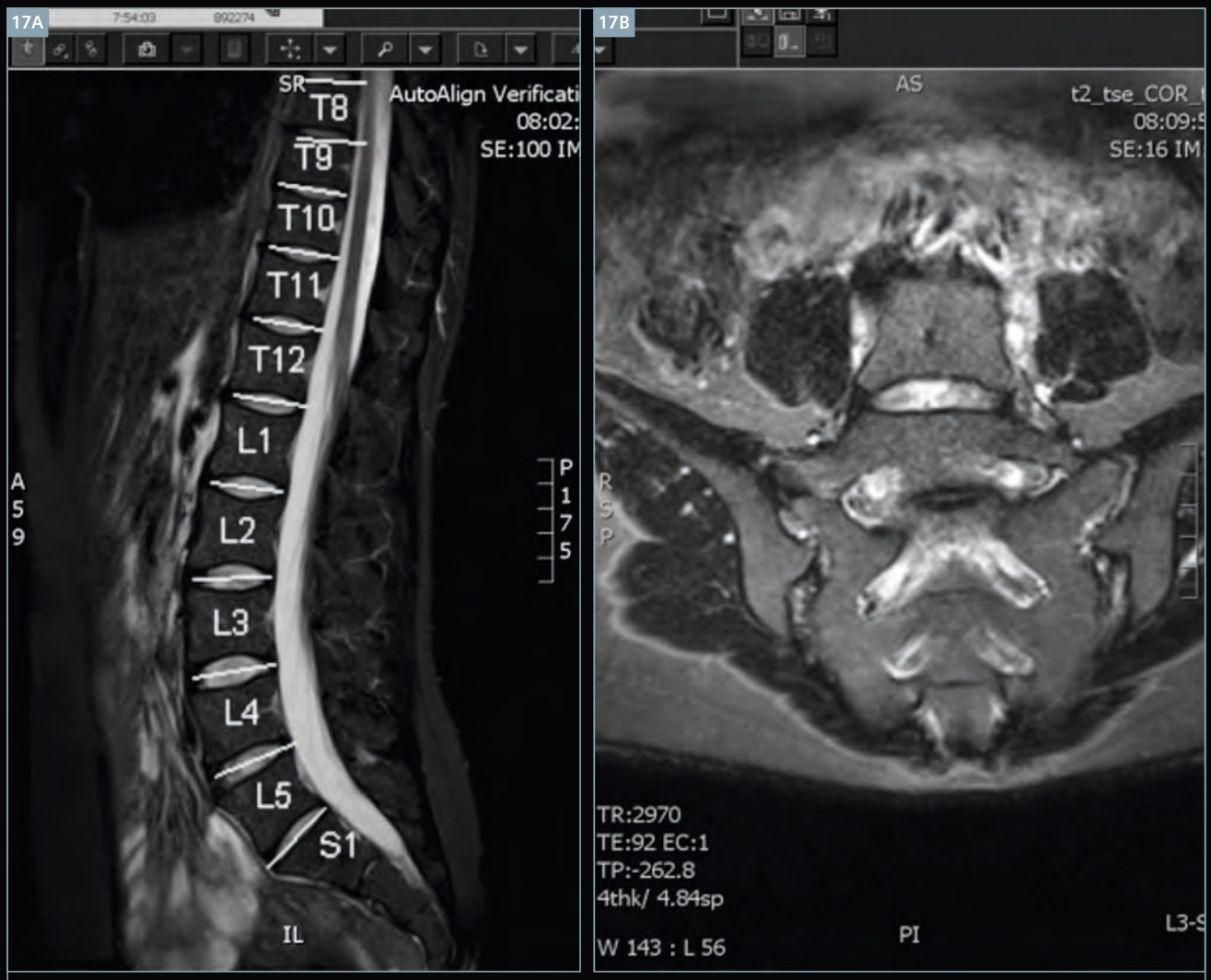

17 Unilateral right sided sacralisation of L5 (Type I) accurately labeled by the Spine Dot Engine in a patient with lower back pain.

Automatic vertebra numbering

Last but not least: Automatic numbering of vertebrae (starting your examination with the localizer at the level of the chin to include C2 as a reference) is a game changer.

Knowing the trouble that can occur with lumbosacral transitional anomalies and the detective work needed to discover if you are dealing with yet another sacralisation or lumbarisation, the accurate and reliable labeling of the vertebrae by the Spine Dot Engine is a very convenient way of improving the quality and speeding up your reporting of lumbar spine examinations. Reported incidence of these transitional anomalies can be as high as up to 35.9% in some populations [1]

References

1 Erken E, Ozer HT, Gulek B, Durgun B. The association between cervical rib and sacralization. Spine 2002 ; 27:1659-1664.

Contact

Johan Dehem, M.D.
VZW jan Yperman
Yeper
Belgium
johan.dehem@gmail.com

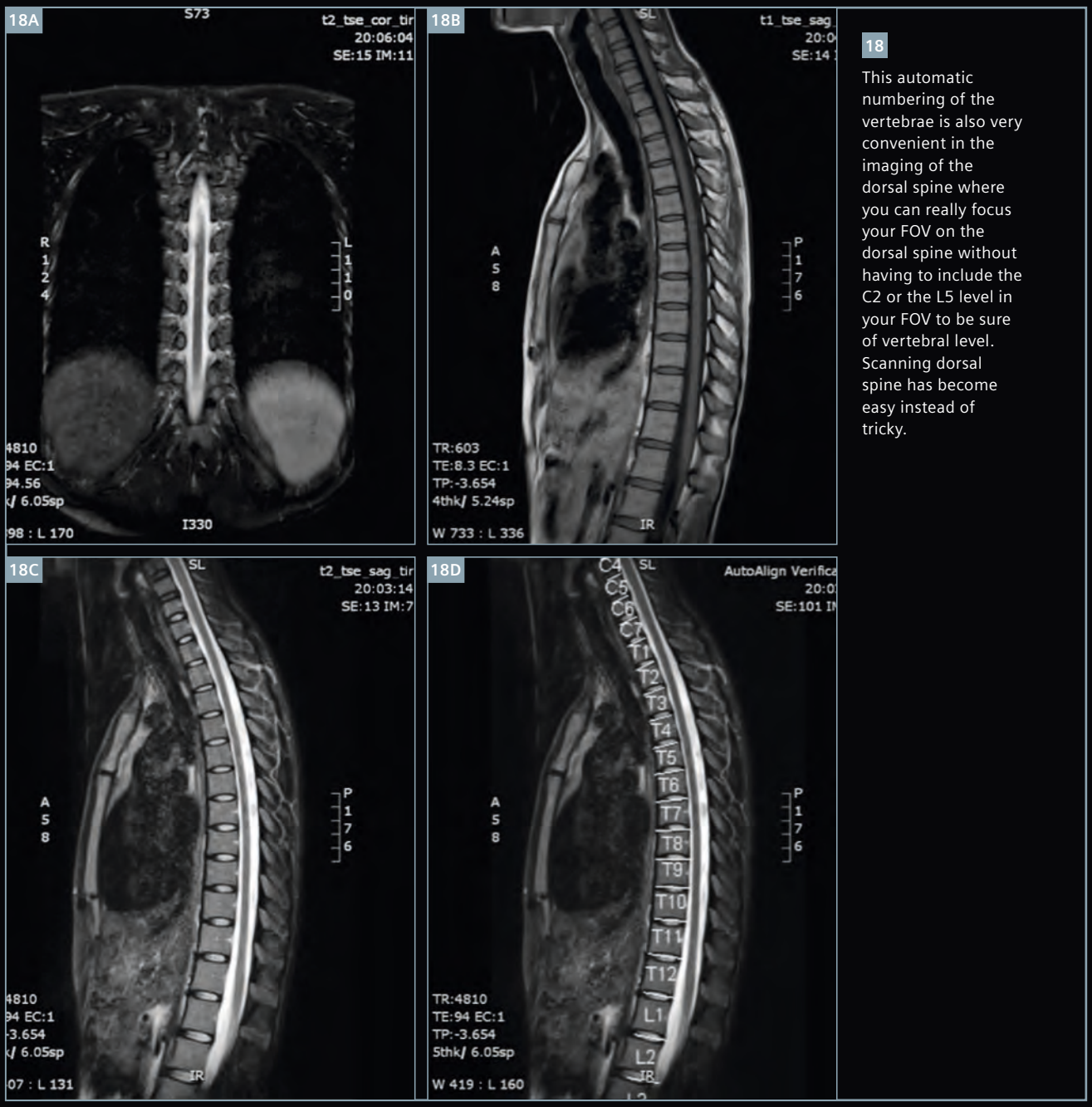

18

This automatic numbering of the vertebrae is also very convenient in the imaging of the dorsal spine where you can really focus your FOV on the dorsal spine without having to include the C2 or the L5 level in your FOV to be sure of vertebral level. Scanning dorsal spine has become easy instead of tricky.

Further information

Visit us at
www.siemens.com/magnetom-world
to listen to Dr. Dehem's talk on
Highest Quality Imaging in an Optimized Clinical Workflow
given during the lunch symposium at the 15th International MRI Symposium MR 2013 in Garmisch-Partenkirchen, Germany.

Johan Dehem, M.D.
VZW Jan Yperman
(Ieper, Belgium)

Kawasaki Disease on CMRI

Gregory L. Compton, MBBS; Lars Grosse-Wortmann, M.D.

Labatt Family Heart Centre at The Hospital for Sick Children, The University of Toronto, Toronto, Ontario, Canada

Cardiac magnetic resonance (CMR) is a valuable tool in the diagnostic work-up of patients with congenital and acquired heart disease, including Kawasaki Disease (KD). In this article we review the epidemiology, pathophysiology, and clinical presentation of KD and illustrate how CMR can aid in the care of patients with this condition.

KD is an acute self-limited vasculitis that was first described in Japan in 1967 [1]. It most commonly affects children between the ages of 1 and 5 years, with an incidence of approximately 112 per 100 000 children per year [1] in Japan. Although KD remains more common amongst persons of Asian and Pacific Islander descent, it is now recognized as a near worldwide endemic and epidemic disease with no racial predilection [1]. In the industrialized world, KD has now surpassed rheumatic fever as the leading cause of acquired heart disease in children [1, 2].

The rare occurrence of this disease during the first few months of life, as well as during later child- and adulthood suggests an infectious etiology, against which adult immunity and maternal antibodies are protective [1], although no specific causative agent has been identified.

KD is typically a febrile illness characterized by fever, rash, conjunctivitis and cervical lymphadenopathy. The condition is diagnosed based on the presence of at least 5 days of fever and more than 4 of the five clinical features [3]. Fewer than 4 clinical features suffice for the diagnosis in the presence of fever with at least 5 days duration and coronary artery aneurysm development [1].

The most serious manifestation is that of an arterial vasculitis which affects both medium and small sized vessels, with a predilection for the coronary arteries. The latter are virtually always involved [1] with aneurysms of the coronary arteries developing in 15–25% of untreated cases [1, 4]. The proximal segment of the left anterior descending (LAD) coronary artery is the most frequent site of aneurysmal involvement, followed by the proximal aspect of the right coronary artery (RCA) and the left main coronary artery. The left circumflex is the least affected of the coronary artery branches [13].

Patient 1

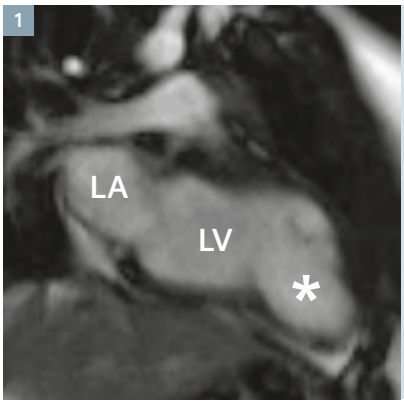

1 Cine steady state free precession image in the 2-chamber plane showing the abnormal contour of the left ventricle (LV) consistent with an aneurysm (asterisk). Note the abnormal thinning of the myocardium in this region.
LA = left atrium.

2 Late gadolinium enhancement following phase-sensitive inversion recovery reconstruction of the data. The left ventricular myocardium near the apex is signal-intense, in keeping with a transmural myocardial infarction and scar formation.

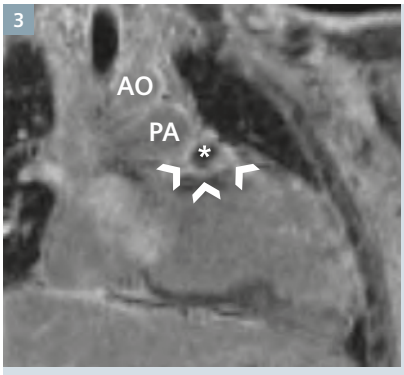

3 Post-gadolinium 3D inversion recovery image demonstrating the low signal thrombus (asterisk) within an aneurysm of the left anterior descending (LAD) coronary artery. This image also demonstrates an abnormally high signal (arrowheads) in the walls of the LAD aneurysm which appear thickened in comparison to those of the main pulmonary artery and aortic arch. This finding is most in keeping with vessel wall injury (fibrosis and/or inflammation) rather than rim-enhancement of the thrombus.
AO = aortic arch, PA = pulmonary artery

Initially, the affected arterial vasculature demonstrates edematous dissociation of the smooth muscle cells, along with destruction of the internal elastic lamina [1]. Fibroblastic proliferation can result in vessel stenoses through intimal thickening. Even after complete regression of the aneurysms residual histological abnormalities of the affected vasculature are often present [1, 2, 5], manifesting in reduced vascular reactivity indicative of endothelial dysfunction [1, 6].

Other cardiovascular involvement is seen in the form of myocarditis, valvulitis and pericarditis with pericardial effusions as a common imaging finding in up to 25% of cases [3, 7]. Acute mitral valvar regurgitation occurs in up to 2% of cases [1, 7, 8] secondary to valvar inflammation or to papillary muscle dysfunction caused by myocarditis or ischaemia. Aortic insufficiency is present in up to 5% of patients [9].

Despite these additional complications of KD, the leading cause of death remain sequelae from coronary artery involvement and the development of coronary artery aneurysms. These may rupture, thrombose or become stenotic [2] – all of which predispose to myocardial ischemia and infarction. Risk factors for the development of coronary artery aneurysms include: (1) longer duration of fever (2) leucocytosis (3) thrombocytopaenia (4) elevated inflammatory markers (5) decreased hematocrit (6) hypoalbuminemia (7) age less than 1 year old (8) male sex [1, 7].

Current treatment algorithms aim at (1) reducing inflammation, (2) avoiding thrombus formation, and (3) preventing aneurysms. Aspirin, initially administered at doses with anti-inflammatory properties followed by lower dosing for anti-platelet aggregation, as well as intravenous immunoglobulin are the mainstay of treatment. These measures reduced the incidence of coronary artery aneurysms to 3–5% [10, 11].

Coronary artery aneurysms tend to regress within 1–2 years of disease onset [12] with approximately 50% showing complete angiographic resolution [1] within this time period. 16% of patients with persistent aneurysms develop coronary artery stenosis [4]. Factors that are associated with aneurysm regression include: onset of disease at less than 12 months of age, female gender, as well as fusiform (as opposed to saccular) shape and distal location of aneurysm [13]. The highest rate of progression to coronary artery stenosis is seen in patients with giant aneurysms (> 8 mm) [1].

With improved imaging detection of complications as well as advances in the medical and surgical management the population of pediatric and adult KD survivors continues to grow. Real risks of long-term sequelae mandate regular imaging follow-up. In fact, new coronary artery aneurysms have been found up to 19 years after disease onset [14].

Imaging findings

2D Echocardiography is the most widely used screening method for coronary artery aneurysms in KD patients. Echocardiograpy typically visualizes the proximal and mid portions of the coronary artery system sufficiently in infants and small children, but its sensitivity and specificity decrease with patient age [15] and distal aneurysms are frequently missed. If visualization of the coronary arteries by echocardiography is poor, regardless of patient age and size, consideration should be given to other imaging modalities, including CMR [16]. The gold-standard of coronary artery imaging remains X-ray angiography. However, cardiac catheterization carries inherent risks including vessel injury and infection, as well as the added burden of exposure to ionizing radiation [17, 18]. Computed tomography is now an alternative to fluoroscopic angiography for coronary artery imaging [19] in many cases, but remains unidimensional with regards to the functional information it provides.

Cardiac Magnetic Resonance

CMR is part of the routine diagnostic algorithm in pediatric* and adult heart disease. Its non-invasive nature (apart from the need for general anesthesia in young children) and the avoidance of ionizing radiation advocate for its use in pediatric patients, particularly when serial follow-up examinations are required. CMR is emerging as the modality of choice for the imaging of structural damage late after KD (level of evidence C, recommendation Class IIa) [5].

Table 1

Sequence	Orientation	Purpose
Cine Steady State Free Precession	Vertical long axis, horizontal long axis, short axis	Ventricular function and regional wall motion abnormalities
3D Steady State Free Precession	Whole heart	Coronary artery anatomy, stenosis & aneurysms
Native 3D Inversion Recovery[$]	Whole heart	Intra-aneurysmal thrombus
First-Pass Perfusion during adenosine infusion and at rest[$]	3 short axis slices, 1 vertical long axis and 1 horizontal long axis slice if heart rate allows	Baseline and inducible myocardial perfusion defects
Whole body angiography	Coronal slabs	Extracardiac arterial involvement
Late Gadolinium Enhancement	Horizontal long axis, short axis	Mycoardial scars
Post-contrast 3D Inversion Recovery[$]	Whole heart	Vessel wall inflammation / scars

Sample MRI protocol for assessment of patients with Kawasaki Disease.
[$]Inversion Time (TI) time set to null blood

Patient 2

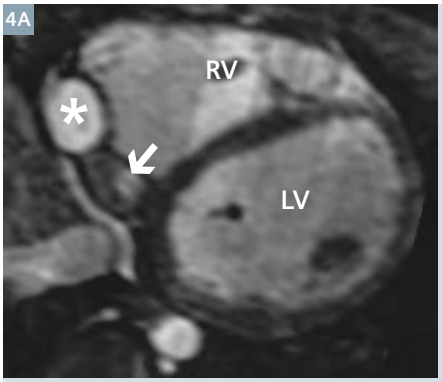

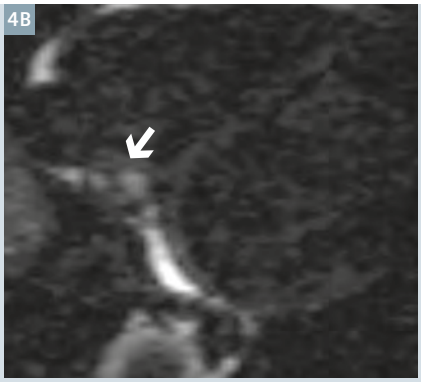

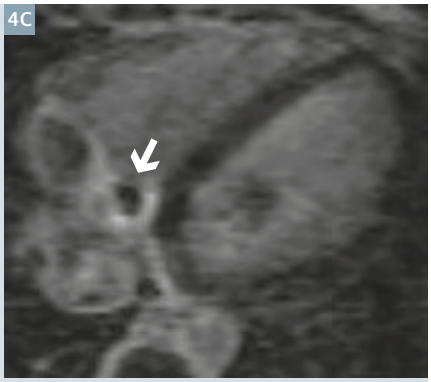

4 **(4A)** Reformat from a non-contrast 3D steady state free precession acquisition (SSFP): The distal right coronary artery is aneurysmal in two places (asterisk in the proximal aneurysm) with the most distal containing thrombus material (arrow). RV = right ventricle, LV = left ventricle **(4B)** Pre-contrast 3D inversion recovery (IR) image reformatted in the same plane as (4A) demonstrating the high signal thrombus in the distal aneurysm (arrow). **(4C)** Post-gadolinium 3D IR image showing enhancement surrounding the thrombus (arrow) with no central enhancement.

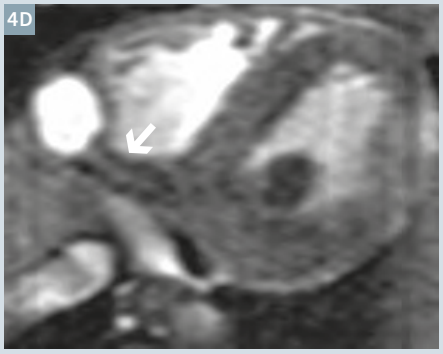

(4D) Reformat from 3D SSFP performed 18 months after (4A) demonstrating absence of blood flow signal within the distal aneurysm (arrow) indicating occlusion due to thrombus. This aneurysm is shown as patent in (4A).

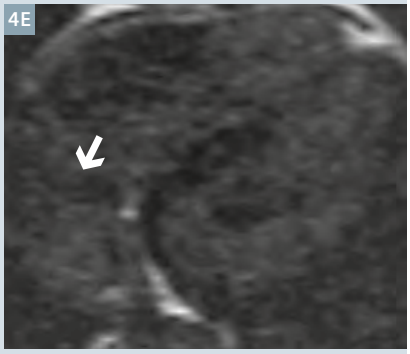

(4E) Pre-contrast 3D IR image, also obtained 18 months after figure (4B) with decreased signal of thrombus within the distal aneurysm (arrow), compatible with evolution (aging and organization) of clot.

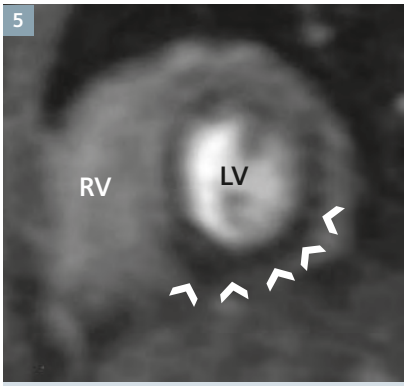

5 Stress perfusion imaging in the short axis plane at the midventricular level in the same patient as in figure 4, demonstrating decreased first pass contrast uptake in the subendocardial region (arrowheads) consistent with ischemia in the inferoseptal, inferior and inferolateral segments of the left ventricle at this level. RV = right ventricle, LV = left ventricle

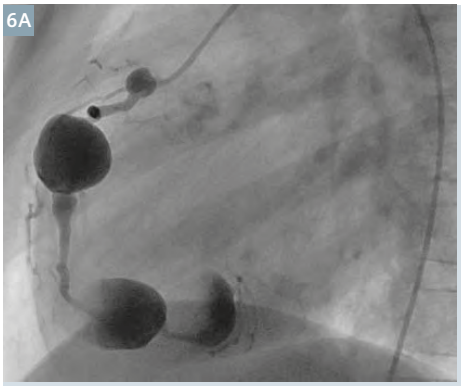

6 **(6A)** Right coronary artery (RCA) selective catheterization and fluoroscopic angiography in the same patient described in figures 4 & 5. Multiple aneurysms of the RCA are seen, with a 'filling defect' in the most distal giant aneurysm in keeping with thrombus as demonstrated in figure (4B).

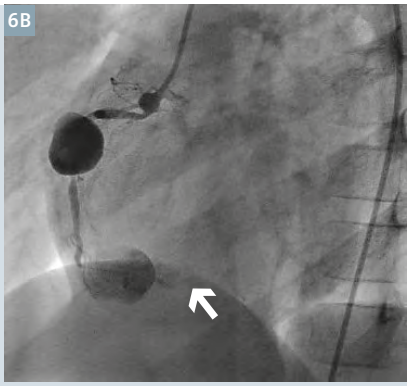

(6B) RCA selective catheterization and fluoroscopic angiography obtained 18 months after (6A) demonstrating lack of filling of most distal aneurysm (arrow) in keeping with thrombus progression and complete occlusion of this aneurysm as shown in figure (4E).

The goals of CMR for KD include the following:

1. Assessment of coronary arteries for aneurysm formation and its complications including thrombosis and stenosis
2. Quantification of ventricular function
3. Evaluation of myocardial perfusion and viability
4. Detection of extra-cardiac aneurysm formation

1. Assessment of the coronary arteries

CMR angiography using an ECG gated 3D steady state free precession (SSFP) sequence with diaphragm navigation is equivalent to fluoroscopic angiography and superior to echocardiography in detecting aneurysms in patients older than 4 months of age with KD [20]. Likewise, Mavrogeni and colleagues have demonstrated excellent agreement between findings on 3D SSFP magnetic resonance angiography and fluoroscopic angiography in KD patients with coronary artery aneurysms [15]. Some groups administer a slow infusion of gadolinium during the 3D SSFP scan to enhance vascular signal. The use of an intravascular contrast agent serves the same purpose, but conflicts with the desire for viability imaging using late gadolinium enhancement (LGE), although some centers are now using extracellular and intravascular contrast agents in the same examination.

Coronary arteries should be assessed with regards to their size and morphology. The upper normal limit beyond which an artery is ectatic varies with age and no uniformly accepted normal values by CMR have been established. The morphology is described as saccular if the axial and sagittal diameters are nearly equal or fusiform if there is asymmetric dilatation with proximal and distal tapering [1, 12].

Coronary artery stenosis can be identified with high sensitivity and moderately good specificity in adult patients [16, 21, 22], but remains more difficult in pediatric patients due to their smaller size and higher heart rates. A relatively fresh clot within a coronary artery aneurysm can be readily visualized using pre and post contrast 3D inversion recovery (IR) sequences with the inversion time chosen to 'null' the signal from blood [23] for both sequences. Recent thrombi carry a high signal (compared to the nulled blood) on the pre-contrast 3D IR and often show peripheral enhancement on the post-gadolinium 3D IR images. This post-gadolinium sequence also allows assessment of the coronary arterial walls which may show thickening and higher signal compared to unaffected arteries [23, 24] indicative of active inflammation or fibrosis [25]. Research in patients after heart transplantation and those with other types of vasculitis has established a relatively long time interval of 20–40 minutes after gadolinium injection for the detection of vessel wall enhancement [25, 26].

2. Ventricular function

CMR is the gold standard for right and left ventricular volumetry and ejection fraction assessment. Either a short axis or an axial cine stack in the SSFP technique is acquired and processed in the usual fashion using Simpson's method of multiple discs. Several short axis slices and a family of horizontal and vertical long axis slices in cine mode should be acquired in every patient to assess for regional wall motion abnormalities. These sequences also are suitable for the detection of pericardial effusions and valvar involvement, although echocardiography remains the technique of choice for the latter. These sequences can be performed using breath-holding for older children and adults, or non-breath-hold for younger children and intubated patients under general anesthesia.

3. Myocardial perfusion and viability

Myocardial perfusion imaging directly images the integrity of macroscopic blood supply to the muscle via the coronary artery system. It can be performed at rest and during stress with adenosine and dipyridamole both of which serve as vasodilators.

Myocardial stress perfusion imaging is currently recommended for all KD patients, with an AHA risk factor profile of III or greater [1]. As compared to nuclear medicine stress perfusion imaging CMR offers superior spatial resolution and radiation-free imaging.

There is some preparation involved for CMR perfusion scans with adenosine: Patients must be screened for contra-indications to adenosine administration including inducible bronchospasm; and, they must abstain from caffeine for at least 24 hours prior to the examination – as this may inhibit the effect of adenosine. Upon arrival at the MRI unit, 2 peripheral intravenous (IV) cannulas are inserted for the administration of the gadolinium contrast and the adenosine infusion required for the stress perfusion imaging. Adenosine is administered at an infusion rate of 140 mcg/kg/minute over up to 6 minutes to induce coronary vascular steal. Most centers inject 0.05 mmol/kg of gadolinium (half-dose) as a rapid push, followed by a saline chaser. Intensive monitoring using q 1 min blood pressure measurements, continuous oxygen saturation measurements and ECG are mandatory, as well as a reliable means of communicating with the patient prior to, during and after the perfusion scan.

In the case of serious side effects that are not controlled by stopping the adenosine infusion aminophylline is administered as an antidote.

Further details of state-of-the-art perfusion imaging can be found elsewhere [27].

If a perfusion defect is identified on the first-pass perfusion stress imaging then a second non-stress sequence is performed, to see if the abnormality was stress induced, i.e. reversible. If no perfusion defect is seen with adenosine the maneuver does not need to be repeated at rest.

LGE imaging is performed 10 to 15 minutes after injection of another 0.05 to 0.1 mmol/kg of gadolinium contrast medium in multiple short and long axis slices, covering the entire heart. Imaging during systole may enhance detection of right ventricular scars by imaging when the myocardium appears 'thicker'. Systolic LGE is performed earlier after contrast administration (typically 5–7 minutes), taking advantage of the shorter inversion times at that interval which allow for acquisition earlier in the cardiac cycle.

Patient 3

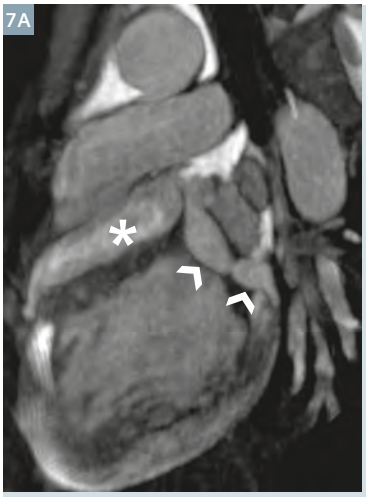

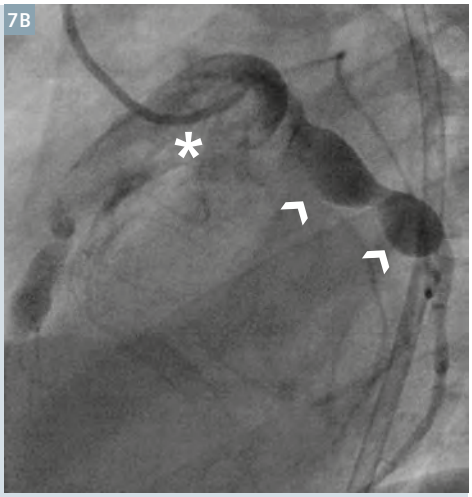

7 **(7A)** Reconstruction from 3D SSFP dataset illustrating a giant fusiform aneurysm of the LAD (asterisk) and multiple saccular aneurysms of the left circumflex (LCx) coronary artery (arrowheads). Note the signal distortion within the LAD aneurysm secondary to flow disturbance from thrombus (not seen). **(7B)** Left coronary artery selective catheterization and fluoroscopic angiography demonstrating the left-sided aneurysms with a filling defect (asterisk) in the LAD aneurysm consistent with thrombus. The LCx aneurysms are shown, corresponding to the magnetic resonance images in (7A).

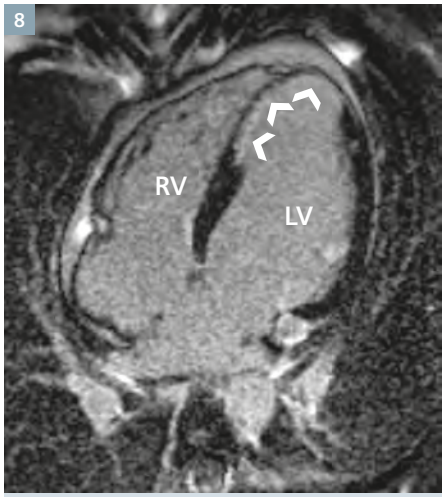

8 Late gadolinium enhancement image in the 4-chamber view depicting high signal involving the apex of the left ventricle (LV) and interventricular septum (arrowheads) consistent with scar formation secondary to myocardial infarction.
RV = right ventricle

Along with ventricular function and any regional wall motion abnormalities myocardial perfusion and viability imaging aid in the decision whether revascularization should be attempted.

4. Extracardiac aneurysms

Although KD preferentially involves the coronary arteries, other arteries can also be affected and show aneurysmal dilatation or other complications including obstruction due to thrombosis and/or stenosis. The axillary, iliac and renal arteries are the most frequently involved extra-cardiac vessels [7]. In one patient series, axillary artery aneurysms were seen in 2% of the cohort, and were found to be 100% predictive of coronary artery aneurysms [7].

In order to visualize the entire arterial tree a whole-body contrast-enhanced magnetic resonance angiogram is helpful.

*Siemens disclaimer: MR scanning has not been established as safe for imaging infants less than two years of age. The responsible physician must evaluate the benefits of the MR examination compared to those of other imaging procedures.

References

1 Newburger JW. Diagnosis, Treatment, and Long-Term Management of Kawasaki Disease: A Statement for Health Professionals From the Committee on Rheumatic Fever, Endocarditis and Kawasaki Disease, Council on Cardiovascular Disease in the Young, American Heart Association. Circulation 2004;110:2747–71.
2 Greil GF. Coronary Magnetic Resonance Angiography in Adolescents and Young Adults With Kawasaki Disease. Circulation 2002;105:908–11.
3 Cox JR, Sallis RE. Recognition of kawasaki disease. Perm J 2009;13:57–61.
4 Kato H, Sugimura T, Akagi T, Sato N, Hashino K, Maeno Y, et al. Long-term consequences of Kawasaki disease. A 10- to 21-year follow-up study of 594 patients. Circulation 1996;94:1379–85.
5 Gordon JB, Kahn AM, Burns JC. When Children With Kawasaki Disease Grow Up. Jac 2009;54:1911–20.
6 Iemura M, Ishii M, Sugimura T, Akagi T, Kato H. Long term consequences of regressed coronary aneurysms after Kawasaki disease: vascular wall morphology and function. Heart 2000;83:307–11.
7 Kato H, Inoue O, Akagi T. Kawasaki Disease: Cardiac Problems and Management. Pediatrics in Review 1988;9:209–17.
8 Akagi T, Kato H, Inoue O, Sato N, Imamura K. Valvular heart disease in Kawasaki syndrome: incidence and natural history. American Heart Journal 1990;120:366–72.
9 Nakano H, Nojima K, Saito A, Ueda K. High incidence of aortic regurgitation following Kawasaki disease. The Journal of Pediatrics 1985;107:59–63.
10 Newburger JW, Takahashi M, Burns JC, Beiser AS, Chung KJ, Duffy CE, et al. The treatment of Kawasaki syndrome with intravenous gamma globulin. New England Journal of Medicine 1986;315:341–7.
11 Newburger JW, Takahashi M, Beiser AS, Burns JC, Bastian J, Chung KJ, et al. A single intravenous infusion of gamma globulin as compared with four infusions in the treatment of acute Kawasaki syndrome. New England Journal of Medicine 1991;324:1633–9.
12 Tacke CE, Kuipers IM, Groenink M, Spijkerboer AM, Kuijpers TW. Cardiac Magnetic Resonance Imaging for Noninvasive Assessment of Cardiovascular Disease During the Follow-Up of Patients With Kawasaki Disease. Circulation: Cardiovascular Imaging 2011;4:712–20.
13 Takahashi M, Mason W, Lewis AB. Regression of coronary aneurysms in patients with Kawasaki syndrome. Circulation 1987;75:387–94.
14 Tsuda E, Kamiya T, Ono Y, Kimura K, Echigo S. Dilated coronary arterial lesions in the late period after Kawasaki disease. Heart 2005;91:177–82.
15 Mavrogeni S, Papadopoulos G, Douskou M, Kaklis S, Seimenis I, Baras P, et al. Magnetic resonance angiography isequivalent to X-Ray coronary angiography for the evaluation of coronary arteries in kawasaki

Patient 4

9 3D SSFP, reformatted in a vertical long axis plane exposing post-aneurysmal stenosis (white arrowhead) of the left anterior descending artery. Note the aneurysm (asterisk) of the left main coronary artery (LCA).

10 Multiplanar reconstruction of a contrast-enhanced magnetic resonance angiogram portraying a large aneurysm (asterisk) of the left axillary artery and multifocal arterial wall irregularity.

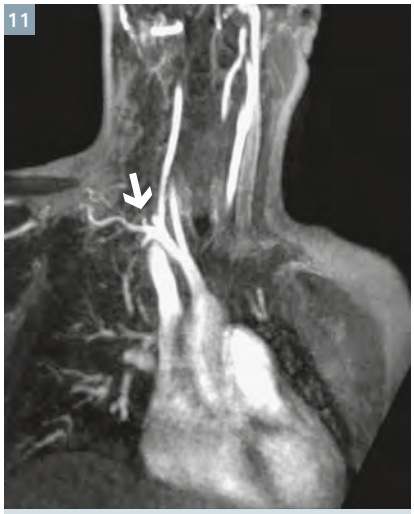

11 A differently angled reconstruction of the same angiographic dataset shows occlusion of the right subclavian artery (arrow) most likely due to thrombosis in the setting of Kawasaki's Disease. The small caliber vessel lateral to the occlusion is an arterial collateral.

disease. Journal of the American College of Cardiology 2004;43:649–52.

16 Raman SV, Aneja A, Jarjour WN. CMR in inflammatory vasculitis. Journal of Cardiovascular Magnetic Resonance 2012;14:1–1.

17 Lederlin M, Thambo J-B, Latrabe V, Corneloup O, Cochet H, Montaudon M, et al. Coronary imaging techniques with emphasis on CT and MRI. Pediatr Radiol 2011;41:1516–25.

18 Vitiello R, McCrindle BW, Nykanen D, Freedom RM, Benson LN. Complications associated with pediatric cardiac catheterization. Jac 1998;32:1433–40.

19 Schoenhagen P, Halliburton SS, Stillman AE, Kuzmiak SA, Nissen SE, Tuzcu EM, et al. Noninvasive Imaging of Coronary Arteries: Current and Future Role of Multi-Detector Row CT. Radiology 2004;232:7–17.

20 Suzuki A, Takemura A, Inaba R, Sonobe T, Tsuchiya K, Korenaga T. Magnetic resonance coronary angiography to evaluate coronary arterial lesions in patients with Kawasaki disease. Cty 2006;16:563.

21 Kim WY, Danias PG, Stuber M, Flamm SD, Plein S, Nagel E, et al. Coronary magnetic resonance angiography for the detection of coronary stenoses. New England Journal of Medicine 2001;345:1863–9.

22 Dirksen MS, Lamb HJ, Doornbos J, Bax JJ, Jukema JW, de Roos A. Coronary Magnetic Resonance Angiography: Technical Developments and Clinical Applications. Journal of Cardiovascular Magnetic Resonance 2003;5:365–86.

23 Prsa M, Hussain T, McCrindle BW, Grosse-Wortmann L. Comprehensive Evaluation of a Patient with Kawasaki Disease and Giant Coronary Aneurysms with Cardiac Magnetic Resonance. Congenit Heart Dis 2013:1–4.

24 Greil GF, Seeger A, Miller S, Claussen CD, Hofbeck M, Botnar RM, et al. Coronary magnetic resonance angiography and vessel wall imaging in children with Kawasaki disease. Pediatr Radiol 2007;37:666–73.

25 Hussain T, Fenton M, Peel SA, Wiethoff AJ, Taylor A, Muthurangu V, et al. Detection and Grading of Coronary Allograft Vasculopathy in Children With Contrast-Enhanced Magnetic Resonance Imaging of the Coronary Vessel Wall. Circulation: Cardiovascular Imaging 2013;6:91–8.

26 Puntmann VO, D'Cruz D, Taylor PC, Hussain T, Indermuhle A, Butzbach B, et al. Contrast Enhancement Imaging in Coronary Arteries in SLE. Jcmg 2012;5:962–4.

27 Nagel E, Lorenz C, Baer F, Hundley WG, Wilke N, Neubauer S, et al. Stress Cardiovascular Magnetic Resonance: Consensus Panel Report. Journal of Cardiovascular Magnetic Resonance 2001;3:267–81.

28 Lewis M, Yanny S, Malcolm PN. Advantages of blood pool contrast agents in MR angiography: A pictorial review. Journal of Medical Imaging and Radiation Oncology 2012;56:187–91.

Lars Grosse-Wortmann, M.D.

Gregory L. Compton, MBBS

Contact

Dr. L. Grosse-Wortmann
Cardiology, Labatt Family Heart Centre
Hospital for Sick Children
555 University Avenue
Toronto, ON M5G 1X8
Canada
Phone: +1 416-813-7654 (x203526)
Fax: +1 416-813-7547
lars.grosse-wortmann@sickkids.ca
www.sickkids.ca/Centres/heart-centre/index.html

Cardiac Imaging with MAGNETOM Prisma: Initial Experience

Saeed Al Sayari, MBBS; Jens Bremerich, M.D.

Division of Cardiothoracic Imaging, University of Basel Hospital, Switzerland

Introduction

Since its introduction at the RSNA 2012, the Siemens 3T MAGNETOM Prisma MRI scanner has been promising the highest quality of MR images.

Some of the features that make it unique to its competitors are its remarkable gradient performance with 80 mT/m @ 200 T/m/s gradients simultaneously on all three axes with fast switching capabilities, the 60 cm bore helping the high homogeneity of the magnetic field, the zero helium boil-off, the latest signal transmit and receive technologies by Siemens (TimTX TrueShape and Tim 4G) and the force-compensated design to reduce vibrations.

The above-mentioned features provide an unprecedented image quality with significantly higher resolution and fewer artifacts. Moreover, the new Tim 4G coil technology with 48, 64 or 128 independent channels provides faster imaging with higher signal-to-noise ratio (SNR). Another great feature that makes this scanner unique is its powerful shimming system with an excellent magnet homogeneity that could be achieved with its advanced higher order shim and/or optional SpectroShim [1].

With all these unparalleled promises, it should not be a surprise that MAGNETOM Prisma has succeeded to draw the attention of CMR specialists as a potential next big step in the field

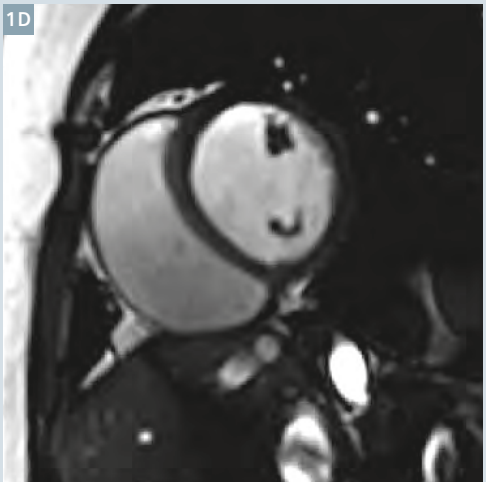

1

SSFP images of the left ventricle. **(1A)** 2-chamber, **(1B)** 3-chamber, **(1C)** 4-chamber, and **(1D)** short-axis mid-ventricular views. The images are of high quality without banding artifacts and show end-diastolic left ventricular dilatation.

of cardiac MRI. This article is intended to provide a brief report on our initial experience with this system, to illustrate examples of some of the cases we examined and to highlight the unique differences compared to other MRI scanners.

Our initial experience

Case 1

A 31-year-old female patient presented with a history of unclear chest pain for the last 2 to 3 months and ankle edema. Her family history was strongly positive for dilated cardiomyopathy. Echocardiography was suspicious for an early dilatation of the left ventricle and showed mildly reduced left ventricular function. Further evaluation with cardiac MRI was advised.

Her examination protocol was adapted to the 2013 updated standardized cardiovascular magnetic resonance (CMR) protocols published by the Society for Cardiovascular Magnetic Resonance (SCMR) [2]. This included the left ventricular structure and function module (SSFP cine images in long and short axes), myocardial edema module (TIRM), first pass perfusion at rest and late gadolinium-enhancement modules.

The SSFP cine images were visually suggestive of a left ventricular dilatation (Fig. 1). The left ventricular function was reduced with global hypokinesia, especially in the septum and inferoseptal. The End-Diastolic-Volume (EDV) was 189 ml (normal range in females 88–168 ml); whereas the indexed EDV (EDVi) was 93 ml/m^2 (normal range in females 57–92 ml/m^2). There was no late enhancement or myocardial edema, (Fig. 2). The findings were suggestive of an early dilated cardiomyopathy without fibrosis or scarring.

What is of importance in this example is that we did not have to perform any frequency scouts, which is the norm in other 3T MRI systems. The SSFP cine images were of excellent quality without any banding artifacts.

As it is known, the banding artifacts appear at frequencies that show a positive to negative phase transition of the signal and depend on susceptibility differences that cause variations in the main magnetic field. These differences are more prominent on higher magnetic fields; hence banding artifacts are more prevalent at 3T [3]. To get rid of these, it is customary to perform a frequency scout prior to SSFP sequences and select the most appropriate frequency with the least artifacts, rendering imaging at 3T more time consuming and sometimes difficult compared to 1.5T. In our experience, Prisma has shown excellent results without the need to perform frequency scouts in the vast majority of cases.

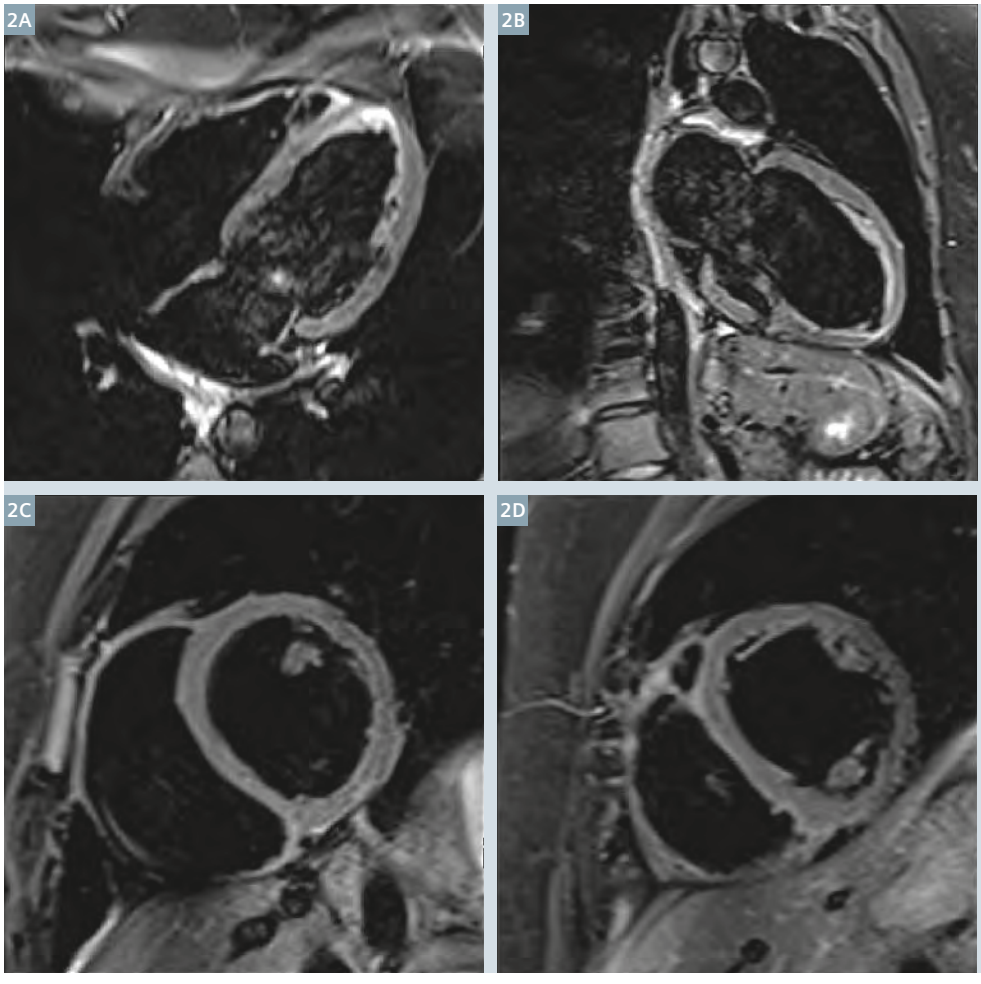

2

TIRM images (sensitive to myocardial edema) showing high quality and resolution. There is no evidence of myocardial edema.

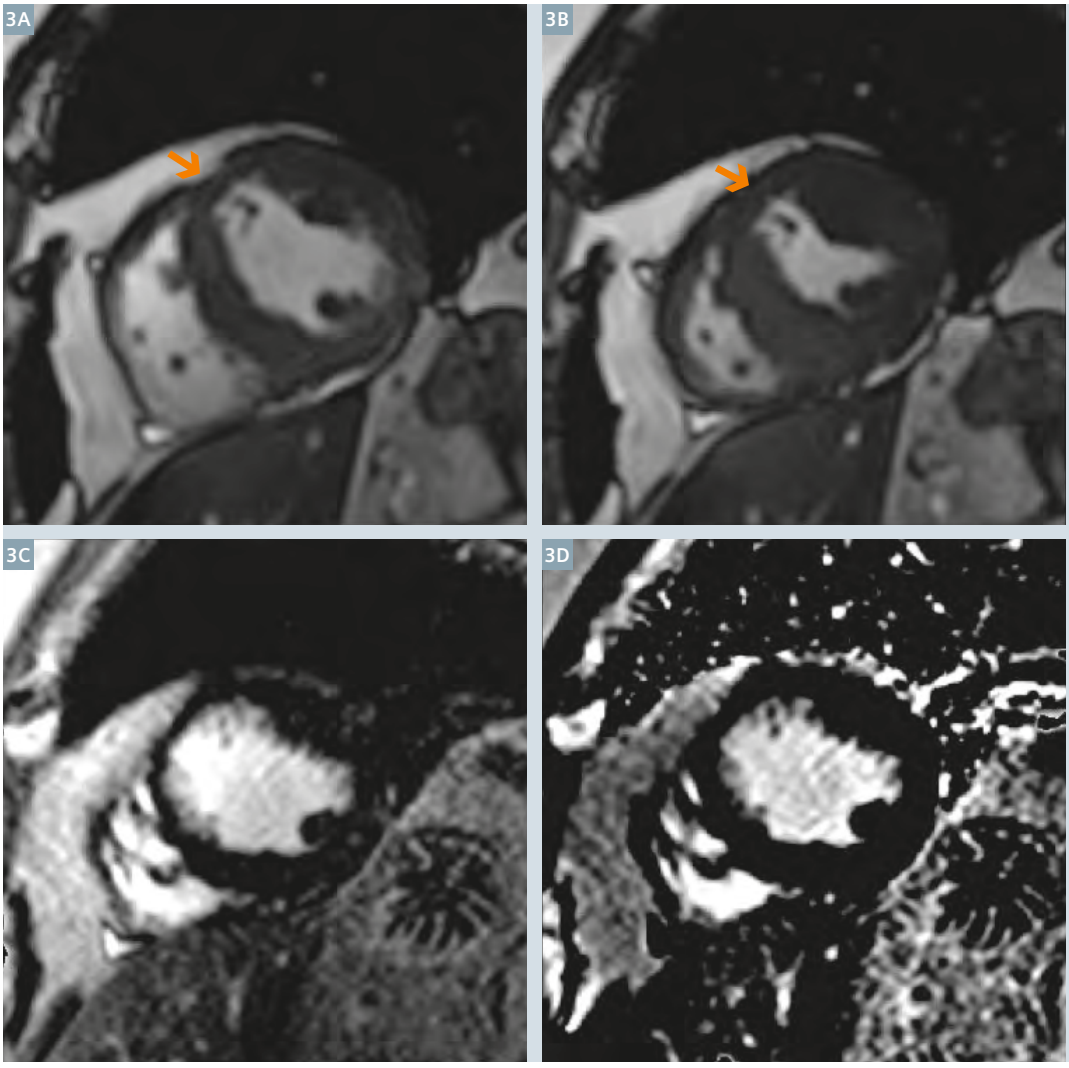

3

SSFP SAX showing thinning of the myocardium anteroseptal (**(3A)** ED, **(3B)** ES), with subendocardial late-enhancement in the corresponding region (**(3C)** magnitude image and **(3D)** PSIR image).

Case 2

A 57-year-old male patient with known triple coronary artery disease presented with progressive chest pain and dyspnoea on exertion. Echocardiography showed minimal reduction in left ventricular function with a left ventricular EF of 52% and anteroapical akinesia. Coronary angiography showed a 60% stenosis in left main, a subtotal proximal LAD obstruction, a 50% stenosis of the circumflex artery and a chronic obstruction of the RCA showing collateral blood supply. The question of myocardial viability was raised to justify a re-vascularisation procedure. The patient was sent for a CMR examination.

His examination protocol included the left ventricular structure and function module (SSFP cine images in long and short axes), myocardial edema module (TIRM) and late gadolinium-enhancement module.

SSFP images showed anteroseptal myocardial thinning with regional akinesia, in addition to inferoseptal and lateral wall hypokinesia in the basal region. Late-enhancement images showed scar formation in the anteroseptal region with potentially viable adjacent myocardium (Fig. 3).

The patient underwent a bypass operation (LIMA to LAD and a sequential vein bypass graft to ramus intermedius and circumflex) and showed a significant improvement postoperatively.

This example again helps to enforce the fact that we were able to obtain excellent SSFP images without the drawbacks of a 3T system. Moreover, late-enhancement images were of excellent quality.

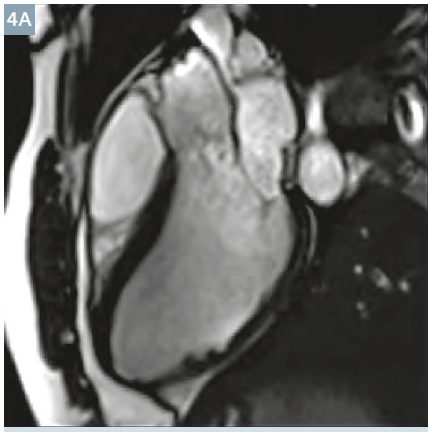

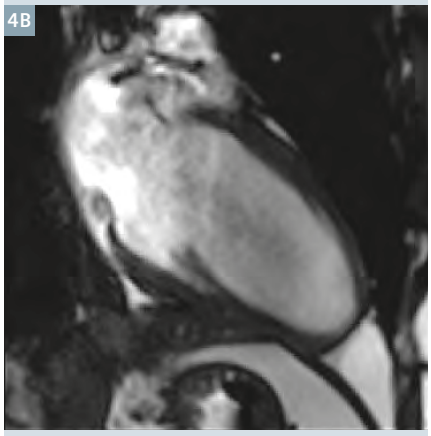

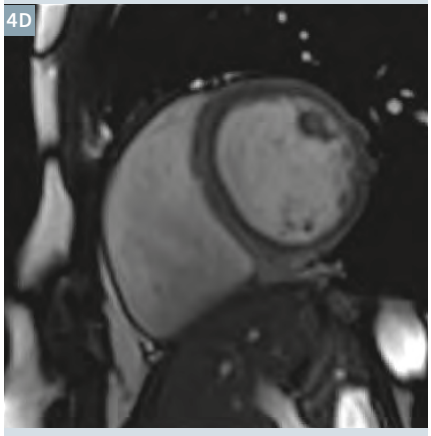

4 SSFP cine images showing mild dilatation of the left ventricle.

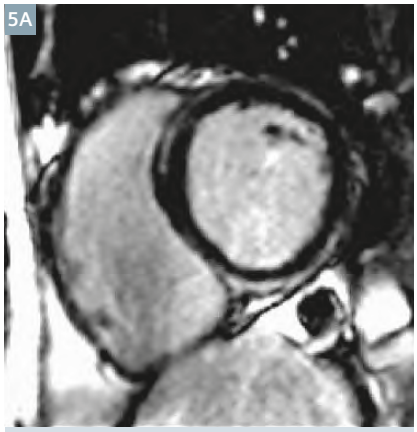

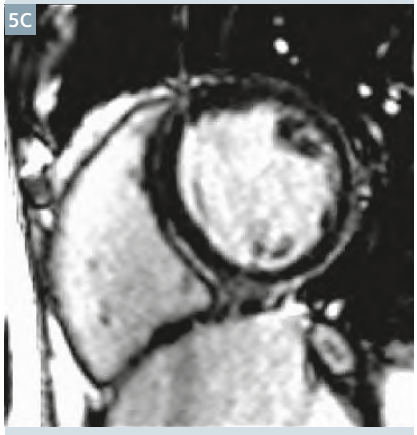

5 Late-enhancement images showing subepicardial and mid-myocardial late gadolinum-enhancement.

Case 3

A 34-year-old male patient presented to the cardiologist with history of extrasystoles and tachycardia for the last 4 months. Echocardiography showed mild reduction in LV function (LVEF 50%) without any regional wall motion abnormalities. The patient was referred to cardiac MRI with suspected myocarditis.

His examination protocol included the left ventricular structure and function module (SSFP cine images in long and short axes), myocardial edema module (TIRM) and late gadolinium-enhancement module.

SSFP images showed dilatation of the left ventricle with EDV of 198 ml and EDVi of 177 ml/m^2 (Fig. 4). There was also a left ventricular function reduction comparable to the echocardiography findings (49%).

The late enhancement findings were of remarkable quality showing patchy and mid-myocardial late-enhancement in the septum, in addition to a subepicardial late-enhancement specially in the lateral, inferoseptal and anterior wall, which is the most common pattern seen in cases of myocarditis [4].

Taking all findings into consideration, a diagnosis of an early dilated cardiomyopathy post myocarditis was made.

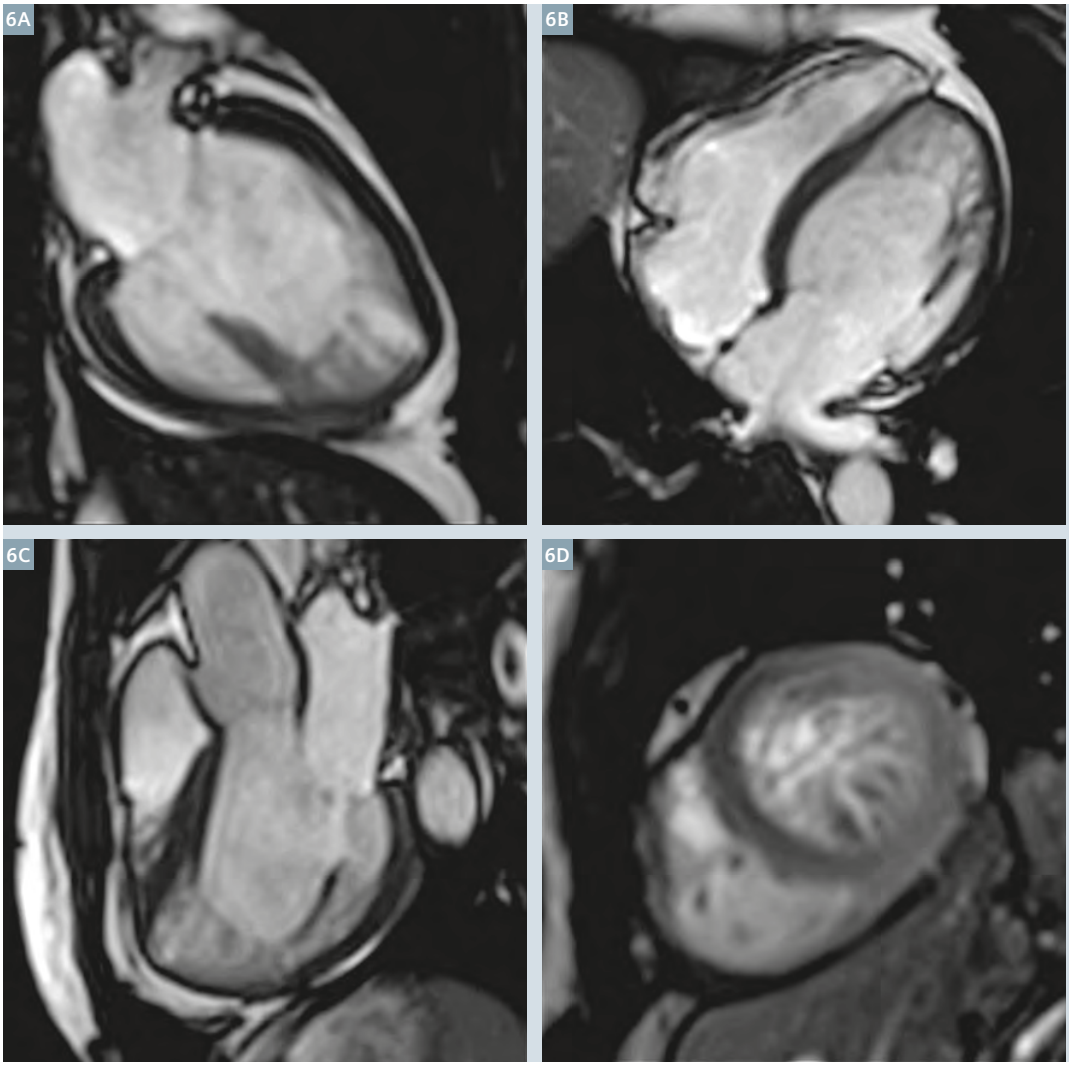

6
SSFP images showing non-compacted myocardium in the apical region.

Case 4

A 41-year-old female patient presented to the emergency department with sudden onset of weakness. She had abnormal EKG and cardiologists were consulted. Echocardiography showed suspected non-compaction of the myocardium. She was referred for a cardiac MRI.

The examination protocol comprised the left ventricular structure and function module (SSFP cine images in long and short axes), myocardial edema module (TIRM) and late gadolinium-enhancement module.

SSFP images showed non-compacted myocardium in the apical region with hypokinesia (Fig. 6). No late-enhancement was present (Fig. 7). The ratio of non-compacted to compacted myocardium was > 2.3, which has been shown to be 86% sensitive and 99% specific for the diagnosis of non-compaction cardiomyopathy [5]. Hence a diagnosis of a non-compaction cardiomyopathy was made.

Conclusion

With its high quality images, fast acquisition time and the ability to acquire cine images without the need for an external ECG monitor or for a frequency scout in most of the cases, MAGNETOM Prisma MRI system seems to be a remarkable evolution for cardiac imaging.

References
1 www.siemens.com/prisma
2 Kramer, C. M., Barkhausen, J., Flamm, S. D., Kim, R. J., & Nagel, E. (2013). Standardized cardiovascular magnetic resonance (CMR) protocols 2013 update. Journal of Cardiovascular Magnetic Resonance, 15(1), 91. doi:10.1186/1532-429X-15-91.
3 Oshinski, J. N., Delfino, J. G., Sharma, P., Gharib, A. M., & Pettigrew, R. I. (2010). Cardiovascular magnetic resonance at 3.0T: Current state of the art. Journal of Cardiovascular Magnetic Resonance, 12(1), 55. doi:10.1186/1532-429X-12-55.
4 Cummings, K. W., Bhalla, S., Javidan-Nejad, C., Bierhals, A. J., Gutierrez, F. R., & Woodard, P. K. (2009). A Pattern-based Approach to Assessment of Delayed Enhancement in Nonischemic Cardiomyopathy at MR Imaging1. Radiographics, 29(1), 89–103. doi:10.1148/rg.291085052.

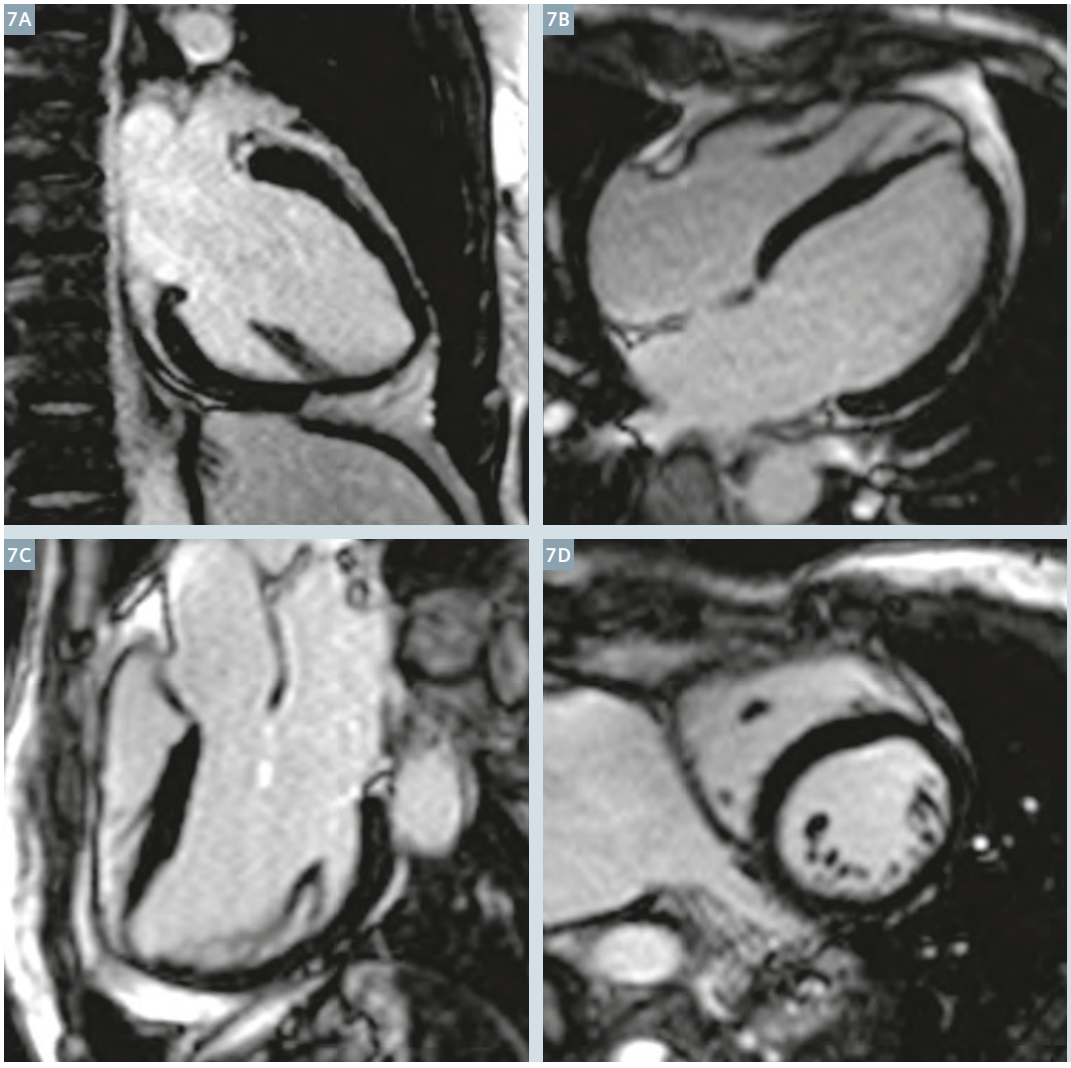

7 Late-enhancement images showing no scars.

5 Petersen, S. E., Selvanayagam, J. B., Wiesmann, F., Robson, M. D., Francis, J. M., Anderson, R. H., et al. (2005). Left ventricular non-compaction: insights from cardiovascular magnetic resonance imaging. Journal of the American College of Cardiology, 46(1), 101–105. doi:10.1016/j.jacc.2005.03.045.

MAGNETOM Prisma is not commercially available in all countries. Due to regulatory reasons their future availability cannot be guaranteed.

Contact

Saeed Al Sayari, MBBS
Non-Invasive Cardiac Imaging Fellow
Division of Cardiothoracic Imaging
Department of Radiology
University of Basel Hospital
Petersgraben 4
4031 Basel, Switzerland
Phone: +41 61 32 86911
Saeed.AlSayari@usb.ch

Saeed Al Sayari

Jens Bremerich

Cardiac Magnetic Resonance Elastography to Estimate Myocardial Stiffness: Initial Feasibility in a Heart Transplant Patient

Arunark Kolipaka, Ph.D.[1,2]; Richard D. White, M.D.[1,2]

[1] Department of Radiology, The Ohio State University Wexner Medical Center, Columbus, Ohio, USA
[2] Department of Internal Medicine, Division of Cardiovascular Medicine, The Ohio State University Wexner Medical Center, Columbus, Ohio, USA

Introduction

Heart failure (HF) is one of the leading causes of death in western world. HF affect over 5 million Americans [1], and comprise the leading cause of hospitalization among Medicare beneficiaries [1] and accounts for $39.2 billion in overall medical costs in the US per year [2]. HF has a poor five-year mortality ~50% [3–5] and has been called "a new epidemic" for the 21st century [6].

Heart transplantation (HT) is the most effective therapeutic option with median survival exceeding 10 years for patients with end-stage HF [7, 8]. However, it is known that early HF accounts up to 20% of perioperative deaths in HT recipients owing to ischemic injury during preservation, pulmonary hypertension and acute rejection [8, 9]. Acute cardiac allograft rejection (AR) reflects the greater risk during the first postoperative year of HT [8]. The highest risk of AR is in the first six months, though it can occur months to years later [10]. Because most patients are asymptomatic, it is important to diagnose and treat acute rejection as early as possible to reverse the process and increase the survival rate.

It is known that inflammation and cell death associated with acute cardiac AR initially leads to myocardial edema and hence increased myocardial stiffness leading to diastolic dysfunction and eventually systolic dysfunction [11, 12]. Currently, endomyocardial biopsy (EMB) is used as a gold standard for diagnosis of cardiac AR [10, 12–17]. EMB is an invasive procedure associated with potentially serious complications such as pneumothorax, tricuspid valve regurgitation as well as vascular or cardiac tissue rupture. Furthermore, it is expensive and has up to 20% of false negative patients [10]. Frequent biopsies should be obtained if an episode of cellular rejection is detected to monitor for reversal of rejection or if the patient has suggestive symptoms. Therefore, there is a need for a technique capable of non-invasively assessing myocardial stiffness, which can avoid the need for EMB.

Magnetic resonance elastography (MRE) is a novel non-invasive imaging technique to estimate stiffness of soft tissues [18–24]. In MRE, cyclic motion is applied to a tissue and a phase-contrast MR image is acquired in which motion-encoding gradients (MEG) are synchronized with the external motion. This produces MRI images of the waves propagating in the tissue. The wave displacements obtained from these images are mathematically converted to stiffness maps.

Previous studies [25-32] have demonstrated application of MRE to estimate *in-vivo* myocardial stiffness. However, to date MRE has not been applied to monitor changes in myocardial stiffness

1

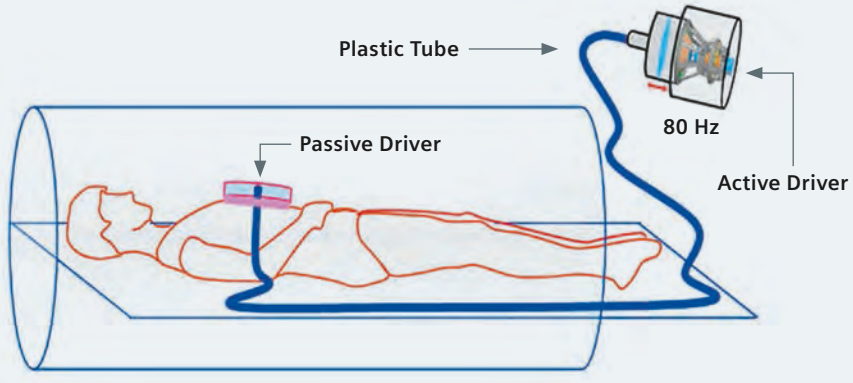

1 Shows the cardiac MRE experimental setup. A passive driver is placed on the chest wall connecting to an acoustic speaker sitting outside scan room using a plastic tube to send 80 Hz mechanical waves into the chest wall to the myocardium.

Table 1: Image acquisition parameters for all sequences performed.

Sequence	b-SSFP Cine	Cine GRE MRE	T2 Prep B-SSFP
Parallel acceleration	GRAPPA rate 2	GRAPPA rate 2	GRAPPA rate 2
Acquisition matrix	256 × 120	256 × 64	192 × 126
FOV (mm)	300 × 400	400 × 400	400
Slice thickness, mm	8	8	8
TR/TE, ms	2.8/1.21	12.5/9.0	3 × R-R/0,24,55
Band width, Hz/pixel	1149	501	930
Flip angle, °	56	25	70
MRE time Offsets	–	4	–
MEG/Excitation frequency, Hz	–	160/80	–
Number of segments	16	16 (+/–)	–
Temporal Resolution(ms)	44.8	200	–

b-SSFP indicates balanced steady state free precession; GRE: gradient echo; MRE: magnetic resonance elastography; MOLLI: Modified Look-Locker inversion recovery; GRAPPA: generalized auto calibrating partially parallel acquisitions; TR: repetition time; TE: echo time, MEG: motion encoding gradients. 16 (+/–) indicates 8 segments for positive MEG and 8 segments for negative MEG for reconstructing a phase contrast image.

*WIP, the product is currently under development and is not for sale in the US and other countries. Its future availability cannot be ensured.

in a HT patient. This study demonstrates the feasibility of applying MRE in a HT patient to monitor changes in myocardial stiffness during first 4 months of post-transplant and correlate to EMB.

Methods

This study was approved by institutional review board. Written informed consent was obtained and documented from the patient. Cardiac MRE was performed in a volunteer (31-year-old male) who underwent HT.

Image acquisition

All imaging was performed using a commercially available 1.5T MRI scanner (MAGNETOM Avanto, Siemens Healthcare, Erlangen, Germany) post 8, 9, 10 and 13 weeks of HT. The volunteer was laid in the supine position and placed head first in the scanner. External vibrations were induced into the heart using a pneumatic driver system (Resoundant, Mayo Foundation for Medical Education and Research, Mayo Clinic, Rochester, MN, USA) by placing the passive driver on the chest wall as shown in figure 1. The pneumatic driver system consists of two parts; an acoustic speaker also known as active driver, and a passive driver. The active driver is placed outside the scan room. The passive driver and active driver are connected through a plastic tube to send the 80 Hz vibrations into the heart muscle as shown in figure 1. A cine gradient-echo prospective gated MRE sequence was used to measure the external motion in the myocardium in a single short-axis slice. In the same short axis slice T2-prepared balanced-steady state free precession (b-SSFP) sequence was used to map the T2 values of the myocardium [33]. Similarly, b-SSFP cine imaging was performed covering the entire ventricle to obtain cardiac function parameters. A phased array receive-only coil was used for all acquisitions. All the imaging parameters are shown in Table 1.

Image analysis

Left Ventricular Function: Left ventricular function parameters such as end-diastolic (ED) volume, end-systolic (ES) volume, and ejection fraction (EF) were determined by Simpson's rule using cine b-SSFP images. It was calculated by computer assisted endocardial and epicardial border definition on an advanced Leonardo workstation (Siemens Healthcare, Erlangen, Germany).

Myocardial Stiffness: MRE wave images were masked with left ventricular (LV) epicardial and endocardial contours and analyzed with MRE Lab (Mayo Clinic, Rochester, MN, USA) using local frequency estimation (LFE) algorithm [34]. In LFE, the wave images were filtered using Butterworth band pass filter to remove the longitudinal component of motion and directionally filtered in 8 directions to remove the reflected waves [35]. Then the first harmonic component of the displacement field (x, y, z) was processed to obtain the weighted stiffness map. The mean effective stiffness of the LV myocardium during ES and ED were reported by drawing regions-of-interest (ROI) in the LV short-axis.

T2 Values: T2 values were recorded from quantitative T2 maps by manually drawing ROI in the LV short axis. Care was taken to avoid inclusion of blood pool.

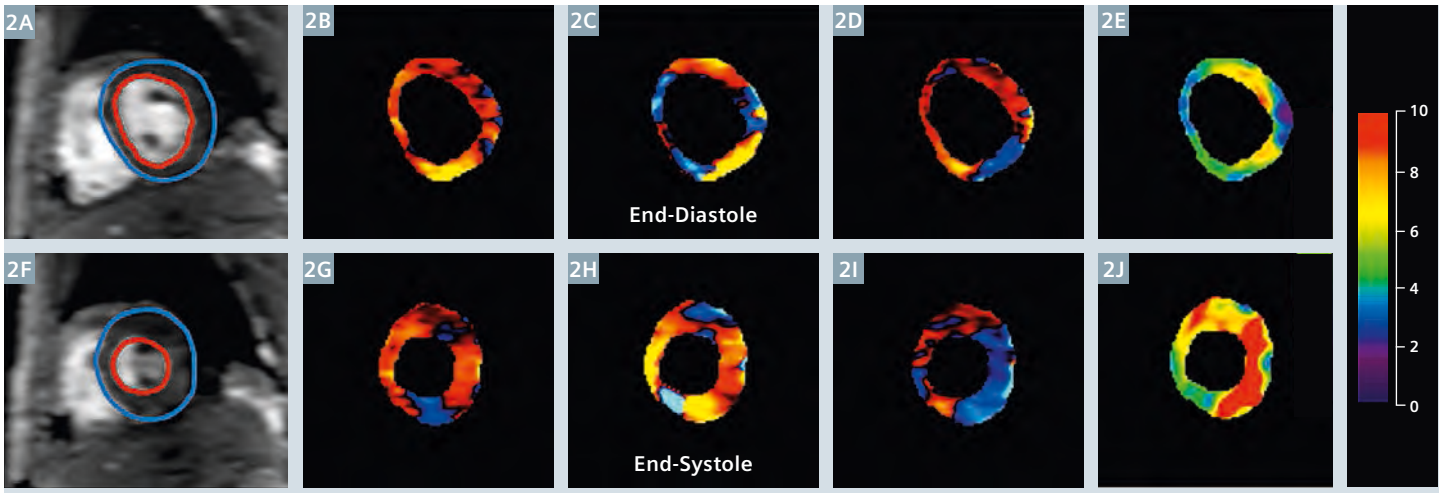

2 An example of cardiac MRE images post 8th week of HT. **(2A, F)** Shows magnitude image during end-diastole and end-systole with red and blue contours delineating LV myocardium. **(2B-D; 2G–H)** Snapshot of wave propagation in all the three directions (x, y, z) during end-diastole and end-systole, respectively. **(2E, J)** MRE-derived weighted effective stiffness map during end-diastole and end-systole. Color bar represents the stiffness values ranging from 0–10 kPa.

Endomyocardial biopsy (EMB): EMB was performed as part of the routine clinical care to determine the AR.

Results and discussion

Volunteer expressed no discomfort during MRI/MRE scans. Table 2 shows ED volume, ES volume, ejection fraction (EF), mean T2 values and mean effective stiffness values at ED and ES in the volunteer during 8, 9, 10, 13 weeks of post HT. All the reported function parameters and T2 values were in the normal range. And also cine b-SSFP images read by an experienced cardiac Radiologist (RDW) indicated normal function.

We have observed variation in mean effective stiffness values in ES and ED during 8, 9, 10 and 13 weeks of post HT. Figure 2 shows an example of snap shot of wave propagation (in all directions) and corresponding stiffness maps during ED and ES during 8th week of post HT. Figure 3 shows the stiffness maps (ED, ES), T2 maps and the corresponding EMB images in the volunteer demonstrating the International Society for Heart and Lung Transplant (ISHLT) scores during 8, 9, 13 weeks of post HT. During 8th week of post HT the EMB results indicated ISHLT score of Grade 1R (i.e. moderate focal acute rejection) and the ES and ED stiffness were 8.5 and 5 kPa, respectively. Similarly, during 9th the EMB results indicated ISHLT score of Grade 0 (i.e. no acute rejection) with relatively lower stiffness values at ES (6.8 kPa) and ED (3.9 kPa) when compared to week 8th. In the 10th week, the volunteer experienced serious episodes of tachycardia and was hospitalized and treated, however no EMB was performed. But his MRE-derived effective stiffness at ES was 10.8 kPa and ED was 7.2 kPa, which were relatively higher than the previous weeks. During 13th week, the EMB results indicated ISHLT score of Grade 1R (i.e. moderate focal acute rejection) and his ES and ED stiffness values were 8 kPa and 5.1 kPa, which were similar to week 8th with Grade 1R rejection. Therefore, MRE-derived effective stiffness closely matched/followed the pattern indicated by EMB results.

Previous studies have indicated that inflammation and cell death associated with acute cardiac AR initially leads to myocardial edema and hence increased myocardial stiffness [11, 12]. We have observed changes in the stiffness values but the T2 values (an indicator of myocardial edema) were in normal range (53–61 ms). This indicates that stiffness might provide superior information compared to T2

Table 2: Cardiac function parameters, T2 values and MRE-derived effective stiffness values.

MRI/MRE Imaging Post HT	Week 8	Week 9	Week 10	Week 13
ED Volume (ml)	168	159	161	146
ES Volume (ml)	70	48	67	64
EF (%)	58	70	58	56
T2 values (ms)	58	57	58	54
ES Stiffness (kPa)	8.5	6.8	10.8	8
ED Stiffness (kPa)	5	3.9	7.2	5.1

ED: end-diastole; ES: end-systole; EF: ejection fraction

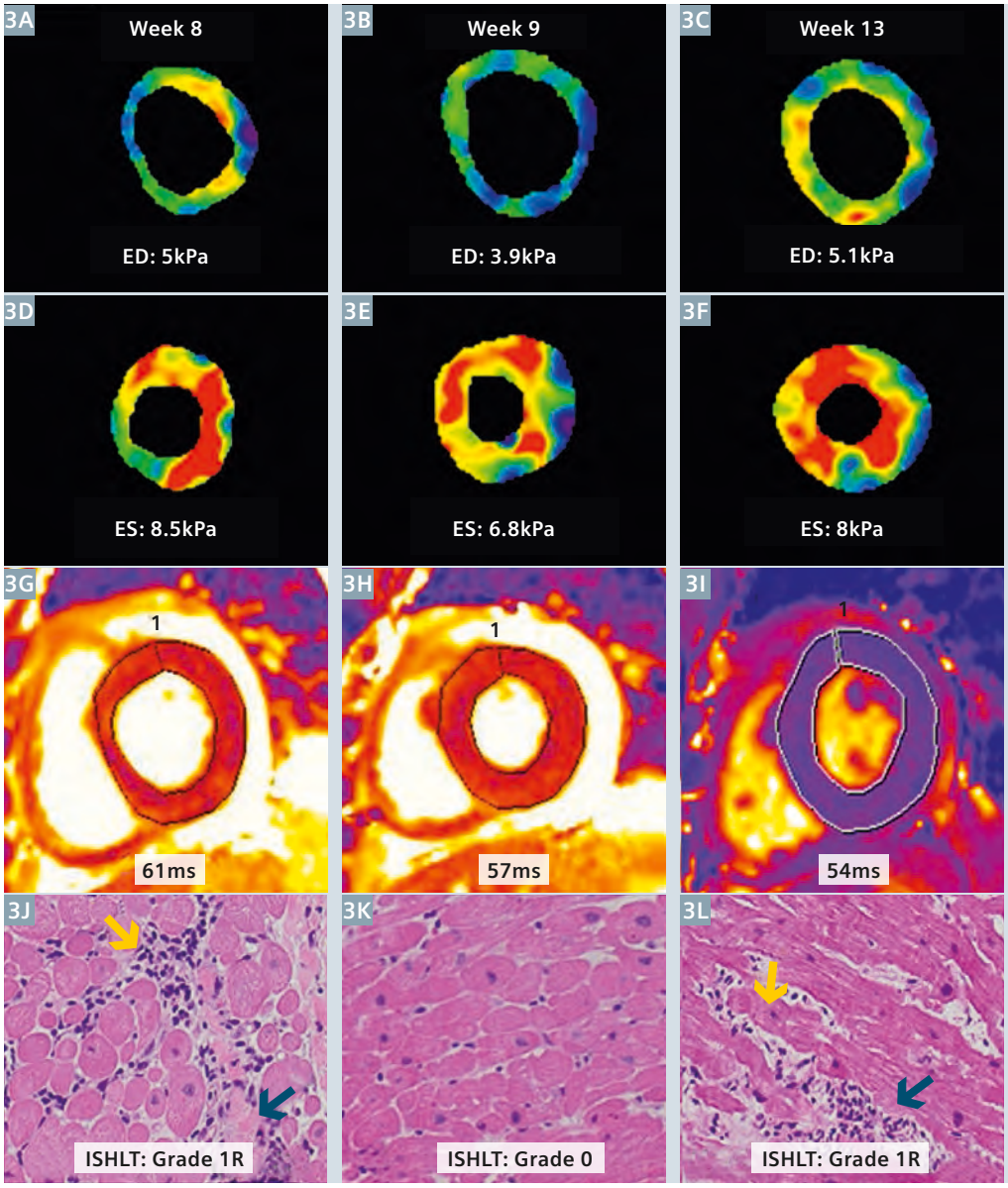

3

Shows the MRE-derived stiffness maps during end-diastole and end-systole in top two rows, T2 maps in the third row and EMB images indicating the cellular rejection (yellow and blue arrows) with ISHLT rejection scores in the last row for weeks 8, 9 and 13.

values in HT patients. However, these results are obtained in only one patient; more patient studies are needed to establish this hypothesis.

In conclusion, this study demonstrated feasibility of performing cardiac MRE in an HT patient. MRE-derived effective stiffness dynamically changed during each week of post HT. These MRE-derived stiffness values also matched to the gold standard EMB based ISHLT scores. However, this is a preliminary case report and more studies are warranted to establish correlation of cardiac MRE-derived stiffness to EMB based ISHLT scores.

References

1 Schocken DD, Benjamin EJ, Fonarow GC, Krumholz HM, Levy D, Mensah GA, Narula J, Shor ES, Young JB, Hong Y. Prevention of heart failure: a scientific statement from the American Heart Association Councils on Epidemiology and Prevention, Clinical Cardiology, Cardiovascular Nursing, and High Blood Pressure Research; Quality of Care and Outcomes Research Interdisciplinary Working Group; and Functional Genomics and Translational Biology Interdisciplinary Working Group. Circulation 2008;117(19):2544-2565.

2 Lloyd-Jones D, Adams RJ, Brown TM, Carnethon M, Dai S, De Simone G, Ferguson TB, Ford E, Furie K, Gillespie C, Go A, Greenlund K, Haase N, Hailpern S, Ho PM, Howard V, Kissela B, Kittner S, Lackland D, Lisabeth L, Marelli A, McDermott MM, Meigs J, Mozaffarian D, Mussolino M, Nichol G, Roger VL, Rosamond W, Sacco R, Sorlie P, Thom T, Wasserthiel-Smoller S, Wong ND, Wylie-Rosett J. Heart disease and stroke statistics--2010 update: a report from the American Heart Association. Circulation 2010;121(7):e46-e215.

3 Levy D, Kenchaiah S, Larson MG, Benjamin EJ, Kupka MJ, Ho KK, Murabito JM, Vasan RS. Long-term trends in the incidence of and survival with heart failure. N Engl J Med 2002;347(18):1397-1402.

4 Senni M, Redfield MM. Heart failure with preserved systolic function. A different natural history? J Am Coll Cardiol 2001;38(5):1277-1282.

5 Lam CS, Lyass A, Kraigher-Krainer E, Massaro JM, Lee DS, Ho JE, Levy D, Redfield MM, Pieske BM, Benjamin EJ, Vasan RS. Cardiac dysfunction and noncardiac dysfunction as precursors of heart failure with reduced and preserved ejection fraction in the community. Circulation 2011;124(1):24-30.

6 Braunwald E. Shattuck lecture–cardiovascular medicine at the turn of the millennium: triumphs, concerns, and opportunities. N Engl J Med 1997; 337(19):1360-1369.

7 Hunt SA. Taking heart--cardiac transplantation past, present, and future. N Engl J Med 2006;355(3):231-235.

8 Toyoda Y, Guy TS, Kashem A. Present status and future perspectives of heart transplantation. Circ J 2013;77(5): 1097-1110.

9 Kirklin JK, Naftel DC, Bourge RC, McGiffin DC, Hill JA, Rodeheffer RJ, Jaski BE, Hauptman PJ, Weston M, White-Williams C. Evolving trends in risk profiles and causes of death after heart transplantation: a ten-year multi-institutional study. J Thorac Cardiovasc Surg 2003; 125(4):881-890.

10 Patel JK, Kobashigawa JA. Should we be doing routine biopsy after heart transplantation in a new era of anti-rejection? Current opinion in cardiology 2006; 21(2):127-131.

11 Mena C, Wencker D, Krumholz HM, McNamara RL. Detection of heart transplant rejection in adults by echocardiographic diastolic indices: a systematic review of the literature. J Am Soc Echocardiogr 2006;19(10):1295-1300.

12 Puleo JA, Aranda JM, Weston MW, Cintron G, French M, Clark L, Fontanet HL. Noninvasive detection of allograft rejection in heart transplant recipients by use of Doppler tissue imaging. J Heart Lung Transplant 1998;17(2):176-184.

13 Caves PK, Stinson EB, Billingham M, Shumway NE. Percutaneous transvenous endomyocardial biopsy in human heart recipients. Experience with a new technique. Ann Thorac Surg 1973;16(4): 325-336.

14 Caves PK, Stinson EB, Billingham ME, Rider AK, Shumway NE. Diagnosis of human cardiac allograft rejection by serial cardiac biopsy. J Thorac Cardiovasc Surg 1973;66(3):461-466.

15 Caves PK, Stinson EB, Graham AF, Billingham ME, Grehl TM, Shumway NE. Percutaneous transvenous endomyocardial biopsy. JAMA 1973;225(3): 288-291.

16 Stinson EB, Caves PK, Griepp RB, Rider AK, Graham AF, Dong E, Jr., Shumway NE. The transplanted human heart in the early postoperative period. Surg Forum 1973;24:189-191.

17 Mehra MR, Uber PA, Uber WE, Park MH, Scott RL. Anything but a biopsy: noninvasive monitoring for cardiac allograft rejection. Current opinion in cardiology 2002;17(2):131-136.

18 Sack I, Beierbach B, Hamhaber U, Klatt D, Braun J. Non-invasive measurement of brain viscoelasticity using magnetic resonance elastography. NMR Biomed 2008;21(3):265-271.

19 Yin M, Talwalkar JA, Romano AJ, Grimm RC, Rossman PJ, Manduca A, Ehman RL. Increased Splenic Stiffness: A Potential Indicator of Portal Hypertension. 2007; Berlin, Germany. In: Proceedings of the 15th Annual Meeting of ISMRM. p 217.

20 Muthupillai R, Lomas DJ, Rossman PJ, Greenleaf JF, Manduca A, Ehman RL. Magnetic resonance elastography by direct visualization of propagating acoustic strain waves. Science (New York, NY 1995;269(5232):1854-1857.

21 Ringleb SI, Bensamoun SF, Chen Q, Manduca A, An KN, Ehman RL. Applications of magnetic resonance elastography to healthy and pathologic skeletal muscle. J Magn Reson Imaging 2007; 25(2): 301-309.

22 Sinkus R, Tanter M, Xydeas T, Catheline S, Bercoff J, Fink M. Viscoelastic shear properties of in vivo breast lesions measured by MR elastography. Magnetic Resonance Imaging 2005;23:159-165.

23 Bensamoun SF, Ringleb SI, Chen Q, Ehman RL, An KN, Brennan M. Thigh muscle stiffness assessed with magnetic resonance elastography in hyperthyroid patients before and after medical treatment. J Magn Reson Imaging 2007;26(3):708-713.

24 Dresner MA, Rose GH, Rossman PJ, Muthupillai R, Manduca A, Ehman RL. Magnetic resonance elastography of skeletal muscle. J Magn Reson Imaging 2001; 13(2): 269-276.

25 Elgeti T, Beling M, Hamm B, Braun J, Sack I. Elasticity-based determination of isovolumetric phases in the human heart. J Cardiovasc Magn Reson 2010; 12(1): 60-68.

26 Elgeti T, Beling M, Hamm B, Braun J, Sack I. Cardiac Magnetic Resonance Elastography: Toward the Diagnosis of Abnormal Myocardial Relaxation. Invest Radiol 2010;45(12):782-787.

27 Elgeti T, Laule M, Kaufels N, Schnorr J, Hamhaber U, Klatt D, Papazoglou S, Warmuth C, Hamm B, Juergen B, Sack I. Assessment of heart function by cardiac MR elastography: Comparison to left ventricular pressure measurements. 2009; Honolulu, Hawaii. In: Proceedings of the 17th Annual Meeting of ISMRM. p 1791.

28 Kolipaka A, Aggarwal SR, McGee KP, Anavekar N, Manduca A, Ehman RL, Araoz PA. Magnetic resonance elastography as a method to estimate myocardial contractility. J Magn Reson Imaging 2012; 36(1):120-127.

29 Kolipaka A, Araoz PA, McGee KP, Manduca A, Ehman RL. Magnetic resonance elastography as a method for the assessment of effective myocardial stiffness throughout the cardiac cycle. Magn Reson Med 2010; 64:862-870.

30 Kolipaka A, Araoz PA, McGee KP, Manduca A, Ehman RL. *In Vivo* Cardiac MR Elastography in a Single Breath Hold. 2010; Stockholm, Sweden. p 591.

31 Kolipaka A, McGee KP, Aggarwal SR, Chen Q, Anavekar NS, Manduca A, Ehman RL, Araoz PA. MR Elastography as a Method to Compare Stiffness Estimates in Hypertrophic Cardiomyopathy and in Normal Volunteers. 2011; Montreal, Canada. p 274.

32 Kolipaka A, McGee KP, Manduca A, Anavekar N, Ehman RL, Araoz PA. In vivo assessment of MR elastography-derived effective end-diastolic myocardial stiffness under different loading conditions. J Magn Reson Imaging 2011;33(5):1224-1228.

33 Giri S, Chung YC, Merchant A, Mihai G, Rajagopalan S, Raman SV, Simonetti OP. T2 quantification for improved detection of myocardial edema. J Cardiovasc Magn Reson 2009;11:56.

34 Manduca A, Oliphant TE, Dresner MA, Mahowald JL, Kruse SA, Amromin E, Felmlee JP, Greenleaf JF, Ehman RL. Magnetic resonance elastography: non-invasive mapping of tissue elasticity. Med Image Anal 2001;5(4):237-254.

35 Manduca A, Lake DS, Kruse SA, Ehman RL. Spatio-temporal directional filtering for improved inversion of MR elastography images. Med Image Anal 2003; 7(4): 465-473.

*WIP, the product is currently under development and is not for sale in the US and other countries. Its future availability cannot be ensured.

Contact

Arunark Kolipaka, Ph.D.
395 West 12th Ave, 4th Floor
Department of Radiology,
Columbus, Ohio – 43210, USA
Phone: +1 614-366-0268
arunark.kolipaka@osumc.edu

The entire editorial staff at University Hospital Basel (USB) and at Siemens Healthcare extends their appreciation to all the radiologists, technologists, physicists, experts and scholars who donate their time and energy – without payment – in order to share their expertise with the readers of MAGNETOM Flash.

MAGNETOM Flash – Imprint

Publisher:
Siemens AG
Medical Solutions
Business Unit Magnetic Resonance,
Karl-Schall-Straße 6, D-91052 Erlangen,
Germany

Guest Editor:
Professor Elmar Merkle, M.D.
Professor of Radiology,
Chairman Department of Radiology
University Hospital Basel, Switzerland

Editor-in-chief: Antje Hellwich
(antje.hellwich@siemens.com)

Editorial Board: Wellesley Were;
Ralph Strecker; Sven Zühlsdorff, Ph.D.;
Gary R. McNeal, MS (BME);
Peter Kreisler, Ph.D.

Production: Norbert Moser, Siemens AG,
Medical Solutions

Layout: independent Medien-Design
Widenmayerstrasse 16, D-80538 Munich,
Germany

Printer: G. Peschke Druckerei GmbH,
Schatzbogen 35, D-81829 Munich,
Germany

We welcome your questions and comments about the editorial content of MAGNETOM Flash. Please contact us at magnetomworld.med@siemens.com.

Manuscripts as well as suggestions, proposals and information are always welcome; they are carefully examined and submitted to the editorial board for attention. MAGNETOM Flash is not responsible for loss, damage, or any other injury to unsolicited manuscripts or other materials. We reserve the right to edit for clarity, accuracy, and space. Include your name, address, and phone number and send to the editors, address above.

MAGNETOM Flash is also available on the internet:

www.siemens.com/magnetom-world

SIEMENS

MAGNETOM Flash

The Magazine of MRI

Issue Number 3/2014 | ISMRM Edition

58

Assessment of Renal Allograft Function with DTI and Tractography, Page 28

Amide Proton Transfer MRI in Patients with High- and Low-Grade Gliomas, Page 39

CMR Elastography to Estimate Myocardial Stiffness, Page 76

Please enter your business address

Institution

Department

Function

Title

Name

Street

Postal Code

City

State

Country

MR system used

Please include me in your mailing list for the following Siemens Healthcare customer magazine(s):

☐ Medical Solutions

☐ MAGNETOM Flash

☐ SOMATOM Sessions

☐ AXIOM Innovations

Stay up to date with the latest information

Register for:

E-mail

☐ Yes, I consent to the above information being used for future contact regarding product updates and other important news from Siemens.

☐ unsubscribe from info service

Please print clearly!

→Visit www.siemens.com/magnetom-world for case reports, clinical methods, application tips, talks and much more clinical information.

SUBSCRIBE NOW!

– and get your free copy of future MAGNETOM Flash! Relevant information from the world of magnetic resonance – gratis to your desk. Send us this postcard, or subscribe online at www.siemens.com/MAGNETOM-World

Siemens AG
Healthcare Sector
Magnetic Resonance
Antje Hellwich – Marketing
P.O. Box 32 60
D-91050 Erlangen
Germany

MAGNETOM Flash

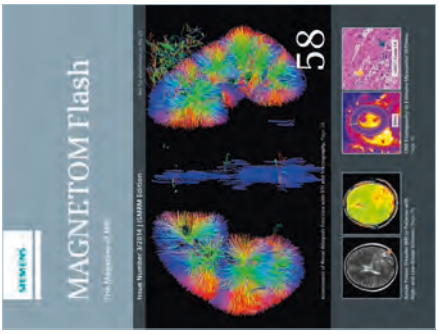

Global Business Unit

Siemens AG
Medical Solutions
Magnetic Resonance
Henkestraße 127
DE-91052 Erlangen
Germany
Phone: +49 9131 84-0
www.siemens.com/healthcare

Local Contact Information

Asia/Pacific:
Siemens Medical Solutions
Asia Pacific Headquarters
The Siemens Center
60 MacPherson Road
Singapore 348615
Phone: +65 6490 6000

Canada:
Siemens Canada Limited
Healthcare Sector
1550 Appleby Lane
Burlington, ON L7L 6X7, Canada
Phone +1 905 315-6868

Europe/Africa/Middle East:
Siemens AG, Healthcare Sector
Henkestr. 127
91052 Erlangen, Germany
Phone: +49 9131 84-0

Latin America:
Siemens S.A., Medical Solutions
Avenida de Pte. Julio A. Roca No 516, Piso
C1067 ABN Buenos Aires, Argentina
Phone: +54 11 4340-8400

USA:
Siemens Medical Solutions USA, Inc.
51 Valley Stream Parkway
Malvern, PA 19355-1406, USA
Phone: +1 888 826-9702

Global Siemens Headquarters

Siemens AG
Wittelsbacherplatz 2
80333 Muenchen
Germany

Global Siemens Healthcare Headquarters

Siemens AG
Healthcare Sector
Henkestraße 127
91052 Erlangen
Germany
Phone: +49 9131 84-0
www.siemens.com/healthcare

Order No. A91MR-1000-108C-7600 | Printed in Germany | CC MR 2114 041410. | © 04.14, Siemens AG

www.siemens.com/magnetom-world